TRANSPORT IN PERIODIC POROUS MEDIA: BEYOND HOMOGENISATION

By

Yahya Farah

A thesis submitted to
the University of Birmingham
for the degree of
DOCTOR OF PHILOSOPHY

School of Mathematics
College of Engineering and Physical Sciences
University of Birmingham
April 2022

ABSTRACT

The dispersion of scalars (or heat) inside a fluid flowing through a porous medium is often examined using the theory of homogenisation. Homogenisation theory provides a coarse-grained description of the scalar at large times and predicts that it diffuses with a certain effective diffusivity, so the concentration of the scalar is approximately Gaussian. This thesis improves on this by developing a large-deviation approximation which also captures the non-Gaussian tails of the scalar concentration through a rate function obtained by solving a family of eigenvalue problems. We demonstrate this on two distinct examples of idealised porous media. The first example is a medium composed of a periodic array of impermeable cylindrical obstacles. We focus on the classical problem of diffusion and examine the dilute and dense limits, when the obstacles occupy a small and large area fraction, respectively. We derive asymptotic approximations for the rate function that explain the validity of the Gaussian behaviour in the dilute limit and capture the non-Gaussian behaviour in the dense limit. We use finite-element implementations to solve the eigenvalue problems yielding the rate function for arbitrary obstacle area fractions and an elliptic boundary-value problem arising in the asymptotics calculation in the dense limit. Comparison between numerical results and asymptotic predictions confirm the validity of the latter. The second example is a periodic network composed of one-dimensional edges along which fluid flows with uniform velocity. We focus on networks generated from Bravais (triangular and square) and non-Bravais (hexagonal) lattices. We derive a set of transcendental equations from where the rate function can be extracted, yielding the effective diffusivity tensor that governs the Gaussian approximation as a byproduct. The dependence of dispersion on the underlying geometry and topology is determined by examining a set of asymptotic approximations for the effective diffusivity tensor and the rate function in a variety of physical regimes.

DEDICATION

Dedicated to hooyaday macaan Saida.

ACKNOWLEDGMENTS

I would like to express my gratitude to those whose help has contributed to the completion of this research. Foremost to my supervisor Dr. Alexandra Tzella, for the patience, diligence, and astute insight and knowledge that has steered me through this research. The meeting and conversations were vital in inspiring me to think creatively to produce a comprehensive thesis. I would like to thank those at the School of Mathematics for their support before and during the pandemic, in particular Prof. Chris Parker.

On a personal note, thank you to my family who have been so generous and given me the upmost support. To my beloved mother Saida and father Mohamed. My special thanks go to my sister Safia and brother Zakaria without their enduring support, I could have never undertaken this research.

I am also thankful to my fellow office mates in 318 Tejas, Gimmy and Soodeh who gave me great help in both study and life. My friends, especially to Awo, and all those who have shown me support during this time; from an encouraging smile to extensive collaborations and all those in-between.

Contents

Abstract **i**

Acknowledgments **iv**

Page

1 Introduction **1**

1.1 First principles: transport and flow 3

1.2 Periodic media 5

1.2.1 Symmetries and Bravais lattices 6

1.2.2 Perforated media 8

1.2.3 Network model 10

1.3 Effective descriptions 11

1.3.1 Diffusive approximation 11

1.3.2 Homogenisation 13

1.3.3 Effective diffusivity results 18

1.4 Aim of the Thesis 21

1.4.1 Large-deviation approximation 21

1.5 Outline 24

2 Diffusion in Arrays of Obstacles **26**

2.1 Introduction 26

2.2 Large-deviation approximation 28

2.3 Relation between the effective diffusive approximation and the large-deviation approximation 32

2.4 Circular obstacles in square lattices 35

2.4.1 Numerical method 35

2.4.2 Numerical results 43

2.5 Asymptotic analysis 47

2.6 Dilute limit 48

2.7 Dense limit 53

2.7.1 Discrete-network approximation 53

2.7.2 Asymptotics 57

2.8 Concluding remarks 67

3 Dispersion in Networks **69**

3.1 Introduction 69

3.2 Large deviations 73

3.2.1 Triangular and square networks 75

3.2.2 Hexagonal networks 76

3.3 Effective diffusivity 78

3.3.1 Effective diffusivity via perturbative expansion 82

3.3.2 Asymptotic regimes 87

3.4 Rate function 93

3.4.1 Tail regime 95

3.4.2 The large-Péclet regime 99

3.5 Concluding remarks 100

4 Conclusion **103**

References **107**

Bibliography **107**

Chapter One

Introduction

The transport and mixing of scalars (passive tracers [*]) e.g. nutrients, heat, etc., is a problem that appears in many geophysical and industrial applications from ground water hydrology [9] to filtration. In all of these examples scalars are confined between solid (usually impenetrable) obstacles that separate spaces (pores). A principal challenge is to predict the distribution of scalars as a result of the interplay between advection, diffusion and geometry of the porous media. This is particularly the case at long times ($t \gg 1$) when the range of scales involved is large.

At this point upscaling methods (which exploit the natural separation of scales) are usually employed to find the effective form of the scalar distribution for large times. These methods (e.g., volume averaging, homogenisation [68], and method of moments [80]) provide an effective description of the pore scale problem valid at the observational scale. In the case of passive scalar transport they approximate the pore scale description given by an advection-diffusion equation by a diffusion equation, in which an effective

---

[*] A passive tracer is a species that does not modify the flow by which it is advected.

diffusivity replaces the molecular diffusivity. The effective diffusivity characterises the phenomenon of scalar dispersion describing the spread of scalar distribution. Thus its value is crucial and has been obtained for various physical problems. Original work on this can be traced back to Maxwell and Rayleigh [59, 72] who obtained the effective (conductivity) diffusivity of dilute suspension of spheres, in the absence of advection. However the first theoretical work considering flow were conducted by Taylor and Aris [83, 10]. They calculated the effective diffusivity for shear flows inside a long thin channel. This was later extended to describe scalar dispersion inside porous media [22].

The diffusive description and the characterisation of dispersion for $t \gg 1$ by an effective diffusivity describe the bulk behaviour of the scalar distribution. It holds for distances of $O(t^{1/2})$ from the centre of mass. However the tails of the scalar distribution are not adequately represented by the diffusive approximation. The precise form of the scalar distribution was recently obtained by Haynes and Vanneste [40, 41]. They developed a large-deviation approximation that is valid at distances of $O(t)$ rather than $O(t^{1/2})$ that captures the tails of the scalar distribution. This was presented in the context of scalar dispersion due to shear and cellular flows; and later extended to describe scalar dispersion in a square network in Tzella and Vanneste [87]. As a result of this method new dispersion phenomenons related to tails of scalar distribution where obtained. These include anisotropic dispersion and finite propagation speeds for small molecular diffusivity.

A natural step is to employ large-deviation approximation to describe scalar dispersion in porous media. In this thesis we use this approximation to describe scalar dispersion in periodic porous media. Periodic systems constitute a well characterised idealisation of heterogeneous media. Unlike in disordered media, they allow for a rigorous calculations to be made without the necessity of ad hoc assumptions. After-all some important mechanisms of dispersion depend only upon the geometry of the porous media. Additionally the study of periodic systems allows us to identify which transport properties are a consequence of periodic constraints. Motivated by this we focus on two distinct classes/models of periodic porous media. The first is characterised by circular obstacles arranged on a lattice. The second are regular networks composed of edges and vertices.

In the remainder of this introductory chapter, we present the fundamental equations of scalar transport in Stokes flows (§1.1). In the following §1.2 we present a classification of the most common periodic structures, and we introduce the two periodic media that are going to be studied in this thesis. In the final §1.3 we focus on scalar dispersion. We report the diffusive approximation by classical homogenisation theory and we recount classical results. We then introduce the large-deviation approximation that is to be used throughout this thesis.

1.1 First principles: transport and flow

In a porous medium, the spatial and temporal evolution of a passive scalar is governed by an advection-diffusion equation, describing advection by a flow and mixing by molecular diffusion. For a flow of constant density ρ, the velocity field $\boldsymbol{u}(\boldsymbol{x}, t)$ $[LT^{-1}]$ is incompressible i.e, $\nabla \cdot \boldsymbol{u} = 0$, where $\nabla = (\partial/\partial x_1, \ldots, \partial/\partial x_n)$ is the n-dimension vector differential operator. In this case, the typical form of this equation is

$$\partial_t \theta + \boldsymbol{u} \cdot \nabla \theta = \kappa \nabla^2 \theta, \quad \boldsymbol{x} \in \Omega, \tag{1.1.1a}$$

where $\theta(\boldsymbol{x}, t)$ $[molL^{-3}]$ is the scalar (molar) concentration with initial condition

$$\theta(\boldsymbol{x}, 0) = \theta_0 \delta(\boldsymbol{x}_0), \tag{1.1.1b}$$

representing a sudden localised release, where $\boldsymbol{x}_0$ is a general point within the pore space Ω. Here, we have assumed that the diffusivity κ $[L^2 T^{-1}]$ is constant (i.e., diffusion is isotropic). Equation (1.1.1a) needs to be supplemented by boundary conditions at the interface between the pores and solid obstacles. There are a number of models describing scalar exchanges between the pores and solid boundary. The most basic model corresponds to an impenetrable boundary for which no-flux (Neumann) boundary conditions apply i.e.,

$$\boldsymbol{n} \cdot \nabla \theta = 0, \quad \text{on } \mathcal{B} \tag{1.1.1c}$$

where $\boldsymbol{n}$ denotes the outward unit normal to the boundary of Ω.

In the absence of advection, Equation (1.1.1) reduces to a classic diffusion equation whose solution is nonetheless highly complex due to the geometry of the void phase of the porous medium. The complexity is further compounded by advection by flow. The associated flows have typically very small velocities [53, 70], and are characterised by low Reynolds number $Re = U\ell/\nu \ll 1$, where U and ℓ are respectively a characteristic flow speed and length scale. Under these conditions, the flow may be described by the steady

Stokes equations,

$$\nu \nabla^2 \boldsymbol{u} - \frac{1}{\rho} \nabla p = 0, \tag{1.1.2a}$$

where $p(\boldsymbol{x})$ is the fluid pressure. Since the flow is divergent free then Stokes equation can be reduced to $\nabla^2 p = 0$. Impenetrability of the solid obstacles together with no slip boundary conditions lead to (Dirichlet) condition at $\mathcal{B}$ i.e.,

$$\boldsymbol{u} = \boldsymbol{0} \quad \text{on } \mathcal{B}. \tag{1.1.2b}$$

The resulting flow is based on a considerable simplification which neglects inertial and transient effects. Nevertheless, the resulting flow can be complex due to the geometrical constraints imposed by the impenetrable solid obstacles [43].

1.2 Periodic media

Naturally occurring porous media usually do not possess long-range order and are difficult to treat in relative completeness. A major simplification can be achieved by assuming that the porous medium is spatially periodic. Periodic systems are simpler to model mathematically, since in such systems their exists a periodic element (elementary cell), whose properties are representative of the entire system. Their study was initiated in the 19th century by Maxwell [59] and Rayleigh [72] to describe various transport properties of periodic arrays of spheres and cylinders with the results applied to describe electrical conduction, a problem directly relevant to the scalar diffusion investigated here.

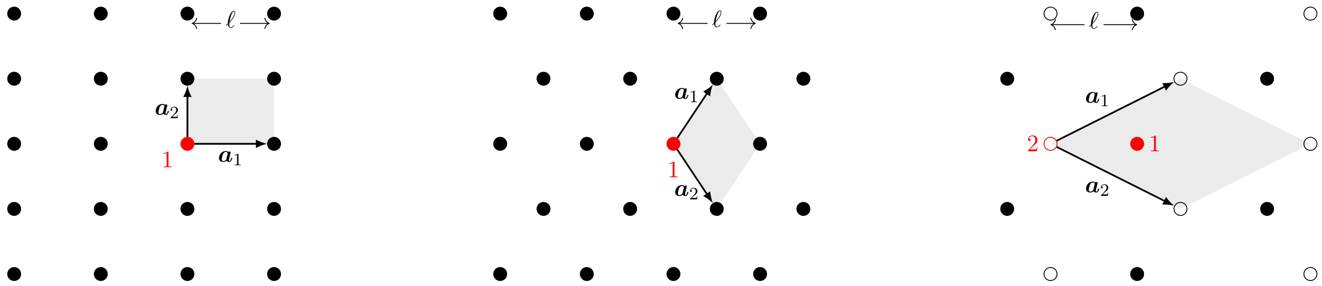

Figure 1.1: A section of the (left) square, (centre) triangular and (right) honeycomb structures. In all cases the elementary cell (shaded grey area) is spanned by the vectors $\boldsymbol{a}_1$ and $\boldsymbol{a}_2$.

1.2.1 Symmetries and Bravais lattices

Periodic media are based on Bravais lattices. A typical Bravais lattice may be described by a translation vector, given by

$$\boldsymbol{r}_\ell^{(\boldsymbol{m})} = \ell \sum_{i=1}^{d} m_i \boldsymbol{a}_i, \quad \boldsymbol{m} = (m_1, \dots, m_d), \tag{1.2.1}$$

where $\boldsymbol{a}_i$ are primitive lattice vectors spanning an elementary cell (whose choice is not unique), ℓ is a scaling factor (or the period of array), and m_i are integers used to index the position of lattice points and d denotes the dimension of space. A key feature of Bravais lattices is that they are translationally invariant.

In two dimension, there exist five fundamental lattices [81]. These can be defined in terms of the following set of primitive vectors

$$\boldsymbol{a}_1 = \gamma \boldsymbol{e}_1, \tag{1.2.2a}$$

$$\boldsymbol{a}_2 = \left(\cos\alpha \; \boldsymbol{e}_1 + \sin\alpha \; \boldsymbol{e}_2\right), \tag{1.2.2b}$$

Topology	General function	Restriction
Square	$\varphi(1, \pi/2)$	–
Rectangle	$\varphi(\gamma, \pi/2)$	$\gamma \neq 1$
Triangular	$\varphi(1, 2\pi/3)$	–
Rhombic	$\varphi(\gamma, \arccos \gamma/2)$	$\gamma \neq 1$
Oblique	$\varphi(\gamma, \alpha)$	$\gamma \neq 1$, $\alpha \neq \pi/2$

Table 1.1: General definition of the five fundamental Bravais Lattices are expressed by the function $\varphi(\gamma, \alpha)$, since any two-dimensional lattice be uniquely defined by the asymmetry ratio γ and angular component α [57]

.

where $\boldsymbol{e}_1, \boldsymbol{e}_2$ are the Cartesian basis vectors and γ, α are the asymmetry ratio and the orientation of cell edges, respectively. The latter are used to parametrise a general function $\varphi(\gamma, \alpha)$ which can be used to describe all five lattices with restrictions given in Table 1.1 [57]. Of these, we focus here on the two uniform Bravais lattices (in which the asymmetry ratio $\gamma = 1$) corresponding to the square and triangular lattices (see Figure 1.1). They can be generated by the primitive vectors where $\boldsymbol{a}_1 = \boldsymbol{e}_1$ and $\boldsymbol{a}_2 = \boldsymbol{e}_2$ for the square lattice (for which $\alpha = \pi/2$), and (upon rotation by $\pi/3$) $\boldsymbol{a}_1 = (1/2\ \boldsymbol{e}_1 + \sqrt{3}/2\ \boldsymbol{e}_2)$ and $\boldsymbol{a}_2 = (1/2\ \boldsymbol{e}_1 - \sqrt{3}/2\ \boldsymbol{e}_2)$ for the triangular lattice (for which $\alpha = 2\pi/3$). In three dimensions the number of fundamental lattices is fourteen [81].

1.2.2 Perforated media

Any periodic media can be constructed by a lattice of repeating cells. To this end, it is convenient to introduce a reference point which can be used to describe the elementary cell of the periodic media. In the simple case of a periodic medium with arrangement of points forming a Bravais lattice, it is sufficient to describe the position of the elementary cell by the position of a reference point (labelled 1 in Figure 1.1 for the square and triangular lattices) given by the lattice vector $\boldsymbol{r}_\ell^{(\boldsymbol{m})}$ in (1.2.1). However, in cases where the arrangement of points forming the periodic medium is not a lattice (e.g., the honeycomb structure in Figure 1.1), the reference point is used as a basis to obtain the position of all other points inside the elementary cell. For example, the honeycomb structure shown in Figure 3.1, has the reference point (labelled 1) which forms a (triangular) lattice whose primitive vectors are

$$\boldsymbol{a}_1 = (\frac{3}{2}\,\boldsymbol{e}_1 + \frac{\sqrt{3}}{2}\,\boldsymbol{e}_2), \tag{1.2.3a}$$

$$\boldsymbol{a}_2 = (\frac{3}{2}\,\boldsymbol{e}_1 - \frac{\sqrt{3}}{2}\,\boldsymbol{e}_2). \tag{1.2.3b}$$

The position of this reference point is given by $\boldsymbol{r}_\ell^{(\boldsymbol{m})}$. The second point (labelled 2) inside the elementary cell has position given by the vector

$$\boldsymbol{r}_2^{(\boldsymbol{m})} = \boldsymbol{r}_\ell^{(\boldsymbol{m})} - \ell\boldsymbol{e}_1. \tag{1.2.4}$$

The simplest and most commonly studied periodic media are based on the uniform square, triangular and honeycomb structures [84]. They can be used to build two distinct classes of simplified periodic porous media. The first class is generated by replacing points with identical impenetrable circular obstacles $\mathcal{B}_{\ell a}(\boldsymbol{r}_\ell^{(\boldsymbol{m})})$ of radius ℓa centred at

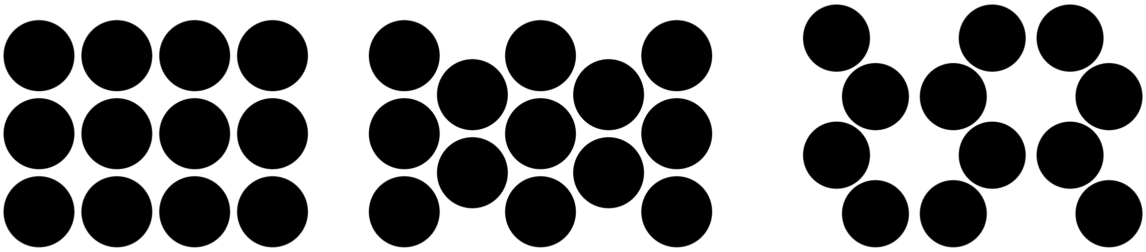

Figure 1.2: A section of the (left) square, (centre) triangular and (right) honeycomb perforated porous media in the dense limit.

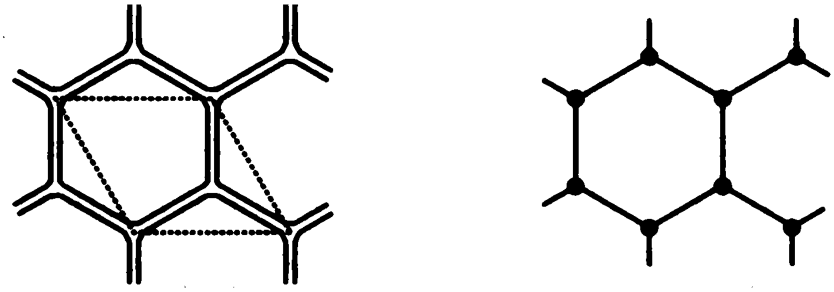

Figure 1.3: Hexagonal network formed from the honeycomb structure (see Figure 1.1). Retrieved from [38].

these points. The size of the circles determine the solid area fraction σ whose value is limited by when the circles touch. Figure 1.2 shows perforated media built from the three configurations shown in Figure 1.1 in the dense limit when the circles are close to touching. It can be shown that the largest solid area fraction is achieved for the triangular packing arrangement whilst the smallest solid area fraction is achieved for the honeycomb packing arrangement.

1.2.3 Network model

The second class of simplified porous media corresponds to networks. These arise as an approximation for highly dense porous media for which the solid area fraction approaches the upper-bound (see for examples [78, 84, 70]). It is shown that the network model becomes increasingly accurate in the limit the gaps between the obstacles vanish. In this case, the perforated media described above are characterised by pores whose widths are much smaller than their lengths (see Figure 1.2). The pores may then be replaced by channels of length ℓ and width $w \ll \ell$ with channels merging at each intersection. For the square, triangular and honeycomb structures there are respectively 4, 6 and 3 channels merging at each intersection (see e.g., Figure 1.3 for the case of honeycomb structure). We associate a network with edges representing channels and vertices representing the intersection of channels. Figure 3.1 shows the square, triangular and hexagonal networks arising from the three cases shown in Figure 1.1. These networks can be visualised as large impenetrable square or hexagonal obstacles in the triangular square and hexagonal lattices. Our analysis in Chapter 3 assumes a simple perfect mixing [2, 28, 51] rule at the vertices. This is the most common of mixing rules which simply assumes no bias in which channel the scalar enters upon exiting an intersection. A detailed review of the various mixing rules in network models is provided in [30].

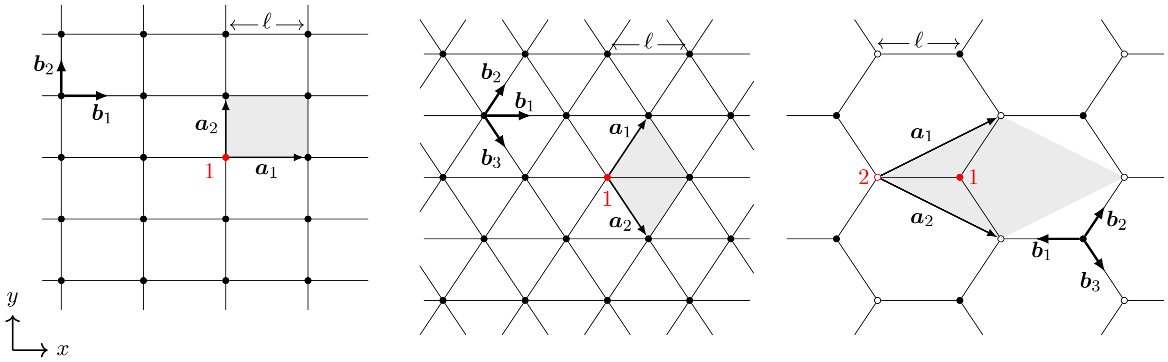

Figure 1.4: A section of the (left) square, (centre) triangular and (right) hexagonal networks. In all cases the elementary cell (shaded grey area) is spanned by the vectors $\boldsymbol{a}_1$ and $\boldsymbol{a}_2$. The unit vectors $\{\boldsymbol{b}_i\}_{i=1}^3$ describe the direction of the network edges connecting the vertices.

1.3 Effective descriptions

1.3.1 Diffusive approximation

The study of scalar dispersion can be traced back to the pioneering work of G.I. Taylor [83] who examined the influence of a shear flow $\boldsymbol{u} = (u(y), 0)$ on the evolution of a passive scalar inside an infinite channel domain $\mathbb{R} \times [0, \ell]$. Using heuristic arguments, Taylor obtained an upscaled version of (1.1.1) that captures the effective scalar behaviour at the macroscale $x \gg \ell$ and is given by the one-dimensional advection-diffusion equation,

$$\partial_t \theta + \langle \boldsymbol{u} \rangle \partial_x \theta = \kappa_{\text{eff}} \partial^2_{xx} \theta, \tag{1.3.1}$$

where $\langle \boldsymbol{u} \rangle$ and κ_{eff} are both constant. This result indicates that at leading order, the variations of the concentration in the direction perpendicular to the channel are subdominant and therefore the channel geometry maybe replaced by the real line. This is made possible by the natural separation of length scales occurring between the channel width and observation scale. Equation (1.3.1) involves the effective coefficients $\langle \boldsymbol{u} \rangle$ and κ_{eff}. The former corresponds to the average fluid velocity across the channel, i.e., $\langle \boldsymbol{u} \rangle = \int_0^\ell \ell^{-1} u(y) dy$. The latter corresponds to the effective diffusive coefficient. Its value is crucial since it controls the spread of the scalar concentration. Taylor found that as $\kappa \to 0$, the effective diffusive coefficient obeys an inverse law, $\kappa_{\text{eff}} \to a\kappa^{-1}$, where a is a positive constant dependent on the exact geometry and flow structure. Thus, counterintuitively, when κ is small the value of the effective diffusion is enhanced by some orders of magnitude in comparison to its molecular value, κ. This phenomenon is generally referred to as "Taylor dispersion" and was later derived by more rigorous means by Aris [10] using the method of moments.

Thereafter Taylor-Aris dispersion theory received considerable attention. It was used to tackle a variety of flows, including periodic and random flows, and domains, and periodic porous media [22]. However, initial applications of Taylor-Aris theory to the study of dispersion in porous media were either specific to certain problems or consisted of various ad hoc assumption. These studies assumed for instance that in general the geometry of the pore space can be modelled by network of capillaries and that the local fluid flow $\boldsymbol{u}$ is every where parallel to the average fluid velocity $\langle \boldsymbol{u} \rangle$ [75, 76]. As discussed in [22] these assumptions overlook the generally complex geometrical characteristics of the pore space and the fact that the fluid motion are not always locally unidirectional (as is the case for shear flows in a channel). Concurrently rigorous theories emerged considering dispersion in porous media starting from pore scale phenomena in the form of advection-diffusion and then upscaling through averaging over the entire porous media. A unifying principle underlying these theories is the decoupling of the average system behaviour from the pore-scale dynamics. At first, the theories were based on the method of moments [22] and volume averaging techniques [91, 90]. However these methods are limited to specific problems and are not pertinent to dealing with problems involving large scales (e.g. velocity fields with a wide range of excited length and time scales). A more substantial theory that is applicable to a variety of settings is discussed next.

1.3.2 Homogenisation

A crucial advancement was achieved in the 70's when a standardised rigorous approach termed “Homogenisation theory" was systematically developed and applied to a variety of periodic problems [16, 47, 15, 12, 13, 14, 79]. This multiscale asymptotic analysis (reviewed in [68]) formed a unified approach in upscaling a diverse range of physical problems in which a large separation of scales naturally occurs. The outcome is a macroscale description in the form of an effective ‘homogenised’ equation parameterised by constant coefficients. The microscale details are incorporated into the effective equation through the coefficients. These coefficients represent intrinsic properties of the medium and are determined via a solution of a periodic closure problem defined on a representative cell, characterising the underlying structure of the medium.

Homogenisation framework

To introduce the concept of homogenisation consider a medium whose properties vary rapidly compared to the macroscale. Let L denote the macroscopic length scale and let l denote the characteristic length scale of the heterogeneities of the medium. Assume now a scale of separation is present so that $\epsilon = l/L \ll 1$ is a small parameter. The system of equations describing a physical quantity θ^ϵ (e.g. concentration field) of the system can generally be expressed in terms of a partial differential operator $\mathcal{L}^\epsilon$ of the form

$$\mathcal{L}^\epsilon \theta^\epsilon = f, \tag{1.3.2}$$

where f represents a source term. Under appropriate assumption of periodicity and in the physical limit corresponding to when the heterogeneities vanish, i.e. $\epsilon \to 0$ it can be shown that θ^ϵ converges, in an appropriate sense, to θ, which solves the homogenised equation:

$$\bar{\mathcal{L}} \theta = f, \tag{1.3.3}$$

where $\bar{\mathcal{L}}$ is the homogenised operator. The homogenised equations (1.3.3) and its coefficients can be derived by taking a formal perturbative expansion of the solution to (1.3.2), in the form of

$$\theta^\epsilon(\boldsymbol{x}, t) = \theta_0(\boldsymbol{x}, \frac{\boldsymbol{x}}{\epsilon}, t) + \epsilon\theta_1(\boldsymbol{x}, \frac{\boldsymbol{x}}{\epsilon}, t) + \epsilon^2\theta_2(\boldsymbol{x}, \frac{\boldsymbol{x}}{\epsilon}, t) + \dots, \tag{1.3.4}$$

where $\theta_i(\boldsymbol{x}, \boldsymbol{y}, t)$, $i = 0, 1, \dots$, are periodic in $\boldsymbol{y} = \boldsymbol{x}/\epsilon$. A unifying theme of homogenisation is to assume all terms in the expansion depend explicitly in both the slow (macroscale) variable $\boldsymbol{x}$ and fast (microscale) $\boldsymbol{y}$ variables. In exploiting the scale of separation a leading-order approximation $\theta_0 = \theta(\boldsymbol{x}, t)$ is sought which is independent of $\boldsymbol{y}$, in the limit $\epsilon \to 0$.

Therefore the homogenised solution $\theta(\boldsymbol{x}, t)$ describes the leading-order behaviour of θ^ϵ. The calculation of the homogenised solution which is parametrised by constant coefficients requires the solution to a periodic cell problem (related to the first-order correction term θ_1) which then allows for the construction of the effective coefficients. The homogenised problem (1.3.3) unlike (1.3.2) is independent of the small parameter ϵ and thus rapidly oscillating coefficients. It is therefore responsive to direct rigorous analysis, numerical solutions or exact solutions in certain cases.

In addition, homogenisation theory (which is viewed as a manifestation of central limit theorem) can be made rigorous by proving the solution θ^ϵ of (1.3.2) converges to the homogenised solution θ of (1.3.3) in the limit $\epsilon \to 0$. Rigorous convergence proofs including error estimates justifying the homogenisation results for varying partial differential equations can be obtained in multiscale expansion[16], two scale convergence [3, 4, 67], oscillating test function [82] and perturbed test functions [32]. An additional benefit of this theory is that in practice higher-order corrections to the effective coefficients are attainable through solving higher-order cell problems (for shear flows see [64, 25, 24, 92]).

Homogenisation applied to scalar dispersion

In the context of scalar dispersion, applying homogenisation theory by use of perturbation expansion (1.3.4) to the advection-diffusion equation (1.1.1a) results in an effective diffusive description for the scalar concentration of the form

$$\partial_t \theta + \langle \boldsymbol{u} \rangle \cdot \nabla \theta = \nabla \cdot (\kappa_{\text{eff}} \cdot \nabla \theta). \tag{1.3.5}$$

As before the mean flow $\langle \boldsymbol{u} \rangle$ is the periodic velocity field averaged over a representative cell and where this time the effective diffusivity κ_{eff} is a tensor determined from an appropriate cell problem. For a localised initial condition (1.1.1b), the solution to (1.3.5) is described by a Gaussian, given by

$$\theta \sim \exp\left(-(\boldsymbol{x} - \langle \boldsymbol{u} \rangle t)^T \cdot \frac{\kappa_{\text{eff}}^{-1}}{4t} \cdot (\boldsymbol{x} - \langle \boldsymbol{u} \rangle t) \right). \tag{1.3.6}$$

The derivation of the diffusive approximation (1.3.5) using homogenisation can be found in [61, 33, 34]. These results notably confirm Brenner prediction which were obtained without any appeal to homogenisation in the case of steady flows. Assuming here for convenience a diffusive time scale which is suitable to problems where the advective effects associated to $\boldsymbol{u}$ average out, i.e. $\langle \boldsymbol{u} \rangle = 0$, usually a result of the symmetries of the problem. The effective diffusivity tensor expressed as a multiple of the identity tensor is

$$(\kappa_{\text{eff}})_{ij} = \kappa\, \delta_{ij} + \kappa \langle \nabla \boldsymbol{\chi}_i \cdot \nabla \boldsymbol{\chi}_j \rangle. \tag{1.3.7}$$

The vector field $\boldsymbol{\chi}$ related to the first order correction $\theta_1(\boldsymbol{x}, \boldsymbol{y}, t) = -\boldsymbol{\chi}(\boldsymbol{y}) \cdot \nabla_{\boldsymbol{x}} \theta(\boldsymbol{x}, t)$ solves the periodic cell problem

$$\kappa \nabla^2 \boldsymbol{\chi} - \boldsymbol{u} \cdot \nabla \boldsymbol{\chi} = \boldsymbol{u}. \tag{1.3.8}$$

The symmetric properties of κ_{eff} is known to depend on the symmetric properties of the flow field $\boldsymbol{u}$ [48]. In this diffusive time scale the effective behaviour is purely diffusive and the effective diffusivity in enhanced over molecular diffusion. If the mean flow does not vanish the problem is then scaled differently to see effective advective behaviour. In essence there are two time scales to the problem a diffusive time scale and an advective time scale. The ratio between these two times is the dimensionless Péclet number, $Pe =$

$U\ell/\kappa$, measuring the relative strength of advection to diffusion. The form of the effective description for varying Péclet limits were deduced for a variety of periodic and random flows [56] and porous media [11, 43]. In [73] it was established that homogenisation theory reduces to Taylor-Aris theory in the special case of a porous media composed of straight parallel tubes.

We have so far focused on the diffusive description (1.3.5) with $\boldsymbol{u}$ a prescribed periodic field. Such periodic flows can be generated by the Stokes equations (1.1.2), provided that the host medium is itself periodic. The effective description of (1.1.2) was first discovered empirically by Darcy [27] who found that the macroscale flow $\langle \boldsymbol{u} \rangle$ inside a porous media is proportional to the applied pressure gradient, and at leading order satisfies Darcy's law

$$\langle \boldsymbol{u} \rangle = -\frac{K}{\mu} \cdot \nabla \langle p \rangle, \tag{1.3.9a}$$

$$\nabla \cdot \langle \boldsymbol{u} \rangle = 0. \tag{1.3.9b}$$

Here $\langle p \rangle$ is the macroscale pressure that is independent of the microstructure of the medium. The coefficient K is the effective permeability tensor that is dependent only on the geometry of a representative cell of the medium and is obtained from solving an appropriate cell problem. Hence, given the pressure gradient $\nabla \langle p \rangle$ at the macroscale, (1.3.9) provides the effective flow inside the periodic medium. Darcy's law is cruicial to various practical fields including in groundwater hydrology and petroleum engineering. Equation (1.3.9) as essential as it is lacked rigorous justification until in the late 60's when S. Whitaker obtained Darcy's law through volume averaging techniques. Darcy's law was later justified through homogenisation [11] by starting from Stokes equations (1.1.2) at the pore scale. The same theory can be used to show the leading order structure of the flow is periodic and therefore readily used to upscale.

1.3.3 Effective diffusivity results

In general, the cell problem determining κ_{eff} can rarely be solved analytically, except if the order of the problem can be reduced to a one-dimensional problem (for example in special cases of shear flows [56], network models [2] and in layered materials [66]). In most cases however the cell problem and thus κ_{eff} can be approximated in asymptotic limits or otherwise bounds on the magnitude of the effective diffusivity can be obtained. Such approximations are essential as they provide an insight into the physical mechanisms responsible for scalar dispersion. We now review for porous media both exact and asymptotic approximations of κ_{eff} in terms of the non-dimensional Péclet number . In particular we present results as it applies to the two classes of periodic porous media introduced in §1.2. A review of effective diffusivity results due to flows is provided in [56]; it transpires that the effective diffusivity is dependent on the topology of the fluid velocity field $\boldsymbol{u}$.

For the pure diffusion problem ($Pe = 0$) applied to the first class of porous media, corresponding to the problem of impermeable obstacles arranged in a periodic lattice. This problem has a long history, dating back to Maxwell [59] and Rayleigh [72], and has relevance to a broad range of applications that include constituent dispersion, heat conduction (with θ the temperature) and (with suitable re-interpretation) electric conduction and electrostatics, in porous media and in composite materials (see e.g. Ch. 2

of [18] for a survey). It was shown in [59, 72] that κ_{eff} accounts for the effect of the obstacles. This effect results from two competing mechanisms: obstacles reduce the area available to the scalar, which enhances dispersion, but they also reduce the scalar flux, which inhibits dispersion. The second mechanism is dominant so that $\kappa_{\text{eff}} \leqslant 1$ (see e.g. Ch. 1 of [44]). Explicit asymptotic results, valid when the obstacles occupy a small or large area fraction σ, are particularly valuable. For small area fraction – the dilute limit – Maxwell and Rayleigh's results [59, 72] yield

$$\frac{\kappa_{\text{eff}}}{\kappa} \sim 1 - \sigma \quad \text{as} \quad \sigma \to 0. \tag{1.3.10}$$

Higher order corrections to (1.3.10) were obtained by Perrins et al. [69] for circular obstacles using multipole methods. More general asymptotic expressions have since been obtained for different lattices [62, 60]. For near-maximal area fractions – the dense limit – and for circular obstacles in the configuration of a square lattice was first studied by Keller [46] who noticed that Maxwell's approximation (1.3.10) is not valid approximately for σ greater than $\sigma_c/3$ [18]. For large values of σ, the concentration flux between neighbouring obstacles is localised in the small gap between the obstacles; Keller [46] obtained that the total concentration flux within the gap is conserved. By approximating the circular boundary with a parabola, Keller [46] obtained the total flux, from where he deduced that

$$\frac{\kappa_{\text{eff}}}{\kappa} \sim \frac{2(\pi/4 - \sigma)^{1/2}}{\pi^{3/2}(1 - \pi/4)} \quad \text{as} \quad \sigma \to \pi/4. \tag{1.3.11}$$

The result was extended to spheres on cubic lattices [46]. Between the dilute and dense limits, the value of κ_{eff} can be computed numerically [69]. For the second class of periodic porous media described by a network model (see Figure 3.1) the cell problem defining κ_{eff} is amenable to analysis. This is because the transport equations (1.1.1) degenerate into linear systems which are comparatively easier to solve. The problem was considered by Torquato et al., [85] (in the context of conductivity of cellular solids) who showed that

$$\frac{\kappa_{\text{eff}}}{\kappa} = \frac{1}{2}, \tag{1.3.12}$$

for all three networks. However (1.3.12) is not a unique to regular networks - it was shown that various networks achieve the same effective diffusion [85, 39].

In the presence of advection ($Pe > 0$), the asymptotic behaviour of κ_{eff} was calculated by Koch et al., [50] for the first class periodic porous media. They identified two mechanisms of dispersion for high Péclet numbers: Taylor dispersion where the effective diffusion scales like Pe^2 or enhanced molecular diffusion where it scales like κ. Interestingly these regimes become active depending on the orientation of the average flow. It was further shown by Koch and Brady [49] that additional mechanisms are present in disordered media. For the second class of porous media described by a network model explicit calculations of κ_{eff} were obtained by Adler and Brenner who assumed perfect mixing at the intersection of channels [2] and advection dominant transport in the channels. Using a combination of graph theory and method of moments they identified similar mechanisms of dispersion present in transport in networks. Similar results were obtained in [38] for purely advective transport whilst assuming time dependent pressure gradient on the network. Dorfman and Brenner [30] built on earlier work by relaxing the rule of perfect mixing at the intersections of channels whilst also incorporating molecular diffusion within the channels.

1.4 Aim of the Thesis

The thesis is motivated by the recognition that, for the initial-value problem (1.1.1), the diffusion approximation (1.3.5) predicted by homogenisation and the corresponding Gaussian distribution of the scalar concentration have a limitation, specifically they apply only to the core of the scalar distribution, $|\boldsymbol{x} - \boldsymbol{x}_0| = O(\sqrt{t})$, and fail in the tails, $|\boldsymbol{x} - \boldsymbol{x}_0| \gg \sqrt{t}$; where the concentration has a non-Gaussian behaviour that depends on the specific flow and geometry configurations. This mirrors a corresponding limitation of the central-limit theorem, which underpins homogenisation (see e.g.[44, 68]) and similarly does not apply to the tail probabilities. This limitation is particularly significant for applications in which low concentrations are critical, such as the migration of radioactive elements from underground nuclear water repositories which has been examined using homogenisation [5, 8]. Our aim, therefore, is to develop a coarse graining of (1.1.1) that goes beyond homogenisation and captures the tails of the scalar distribution.

1.4.1 Large-deviation approximation

A significant advancement was made quite recently in this direction by Haynes and Vanneste [40]. They applied the theory of large deviations [37, 36] (see also [86]) to transport in periodic fluid flow to capture the behaviour of the concentration $\theta(\boldsymbol{x}, t)$

$$\theta(\boldsymbol{x}, t) = \phi(\boldsymbol{x}, \boldsymbol{\xi}, t)\, \mathrm{e}^{-tg(\boldsymbol{\xi})}, \quad \text{where} \ \ \boldsymbol{\xi} = \frac{\boldsymbol{x} - \boldsymbol{x}_0}{t} \in \mathbb{R}^2 \tag{1.4.1}$$

that is valid for $|\boldsymbol{x} - \boldsymbol{x}_0| = O(t)$, thus improving on homogenisation. Here $g \in \mathbb{R}$ corresponds to the rate (or Cramér) function. It provides a continuous approximation for the most rapid changes in θ. It is well known that g is positive, convex, and has a single minimum and zero located at say, $\boldsymbol{\xi} = \boldsymbol{\xi}_*$. Subdominant corrections involve ϕ which possess the same periodic dependence in $\boldsymbol{x}$ as the lattice i.e.,

$$\phi(\boldsymbol{x} + \boldsymbol{r}_\ell^{(\boldsymbol{m})}, \boldsymbol{\xi}, t) = \phi(\boldsymbol{x}, \boldsymbol{\xi}, t), \tag{1.4.2}$$

Expression (1.4.1) introduces variable $\boldsymbol{\xi}$ that capture the behaviour at the macroscale. On the other hand $\boldsymbol{x}$ describes variations on the microscale. The rate function is readily determined via a solution of a family of eigenvalue problems which can be regarded as a generalisation of the cell problem that appears when homogenisation is used to compute κ_{eff} (e.g.[68]).

Homogenisation and the corresponding diffusive approximation (1.3.5) can be recovered from the more general large-deviation approximation (1.4.1) by taking an expansion of g for small $\boldsymbol{\xi}$. Taking a Taylor expansion of g around $\boldsymbol{\xi}_*$ we obtain

$$g(\boldsymbol{\xi}) \sim g(\boldsymbol{\xi}_*) + \frac{1}{2}(\boldsymbol{\xi} - \boldsymbol{\xi}_*)^T \cdot H_g^{-1} \cdot (\boldsymbol{\xi} - \boldsymbol{\xi}_*) + \ldots, \tag{1.4.3}$$

where $H_g = \nabla_{\boldsymbol{\xi}} \nabla_{\boldsymbol{\xi}} g(\boldsymbol{\xi}_*)$ is the Hessian of g evaluated at $\boldsymbol{\xi}_*$. Introducing (1.4.3) inside (1.4.1) and comparing with the diffusive (Gaussian) approximation (1.3.6) yields,

$$\langle \boldsymbol{u} \rangle = \boldsymbol{\xi}_* \quad \text{and} \quad \kappa_{\text{eff}} = \frac{H_g^{-1}}{2}. \tag{1.4.4}$$

Haynes and Vanneste [40] made clear the relationship between the large-deviation approach and homogenisation can be made completely explicit by noting that a perturbative solution of the family of eigenvalue problems (obtained from the large-deviation approximation (1.4.1)) in the limit $|\boldsymbol{\xi}| \to 0$ recovers, at leading order, the cell problem of homogenisation (1.3.8) that determines κ_{eff}. Pursuing the expansion to higher orders in $|\boldsymbol{\xi}|$ yields corrections to $g(\boldsymbol{\xi})$ that correspond to improvements to homogenisation involving diffusion-like operators of degrees higher than 2 [64]. See §2.3 of [40] for details of this expansion in the context of advection–diffusion.

Explicit expressions for the rate function were obtained for both shear and cellular flows [40]. The approach was then developed for a square network in [87] and quite recently for the classical problem of diffusion in circular obstacles on a square lattice [35]. In all these problems it was shown that the rate function generalises classical results on effective diffusivity. These include new phenomena relevant at the tails of the scalar concentration such as anisotropic dispersion, for small molecular diffusivity finite propagation speeds and a regime where the scalar concentration is controlled by single shortest-distance paths. The effectiveness of the large-deviation results for moderately large t were demonstrated through Monte Carlo simulations. Owing to its recent development, the large-deviation approximation is yet to be applied to scalar dispersion in porous media. This is achieved in this thesis for periodic porous media and demonstrated on the two distinct classes of periodic media introduced in §1.2.

The large deviation ideas used in this thesis can be readily generalised to consider more complex systems. For instance, owing to the close connection between large deviations and chemical-front propagation in the Fisher–Kolmogorov–Petrovsky–Piskunov (FKPP) model (e.g.[36]), the family of eigenvalue problems obtained from the large deviation approximation (1.4.1) also determines the speed of these fronts [17] (see for example [58, 6] for linear chemical reactions in periodic geometry). Another context in which large-deviation ideas are potentially applicable are to non-diffusive models of dispersion such as continuous-time random walks which have been proposed for complex, non-periodic media (e.g.[29]).

1.5 Outline

The focus of this thesis is to employ the large-deviation approximation to study scalar dispersion on two models of periodic media introduced in §1.2. The thesis itself consists of two research chapters: Chapter 2 concerns the first model corresponding to periodically perforated media. We specifically study the classical square lattice model. We obtain a cell eigenvalue problem whose solution determine the rate function. We focus on the dense limit and derive asymptotic approximation for the rate function in this limit, valid uniformly over a wide range of distances. We use finite elements to calculate the rate function for arbitrary obstacle area fractions and an elliptic boundary-value problem arising in the asymptotics calculation. These reveal an interesting transition of g as the solid area fraction increases. The results contained in this chapter are in collaboration with Daniel Loghin and Jacques Vanneste. Published in Proceedings of The Royal Society A [35].

Next, Chapter 3 focuses on the second model which consists of the three regular networks (see Figure 3.1). We obtain a cell eigenvalue problem. Their solution is provided in terms of a transcendental equation. The rate function is thereafter determined and contrasted amongst the three networks. We examine the varying asymptotic limits of the rate function g for all networks and compare this against g obtained numerically from the transcendental equations. We obtain a diffusive description of the scalar dispersion and deduce explicit expressions for the effective diffusivity tensor K. We study the asymptotic behaviour of K for all three networks with respect to both the strength and orientation of flow. Finally we study the behaviour of the rate function outside the region of validity of the diffusive description. In particular we study both the strong flow asymptotic behaviour of the rate function and the tail behaviour of g.

In chapter 4, we draw together some concluding remarks, and then discuss several directions in which our results could be extended using the framework developed in this thesis.

Chapter Two

Diffusion in Arrays of Obstacles

2.1 Introduction

In this chapter, we consider the diffusion of a passive scalar inside a two-dimensional homogeneous medium interrupted by an infinite number of impermeable obstacles $\mathcal{B}(\boldsymbol{r}^{(\boldsymbol{m})})$ (e.g., perforations) arranged in a periodic lattice $\boldsymbol{r}^{(\boldsymbol{m})}$ (see Equation (1.2.1)), as illustrated in Figure 2.1 for the case of circular obstacles. The scalar concentration $\theta(\boldsymbol{x}, t)$ satisfies the diffusion equation (1.1.1) with $\boldsymbol{u} = \boldsymbol{0}$. Taking ℓ as reference length, ℓ^2/κ as reference time and θ_0 as the reference concentration, the non-dimensional scalar concentration evolves according to

$$\frac{\partial \theta}{\partial t} = \nabla^2 \theta, \quad \boldsymbol{x} \in \Omega, \tag{2.1.1a}$$

with no-flux (Neumann) conditions on the boundaries $\mathcal{B}$ of the obstacles

$$\boldsymbol{n} \cdot \nabla \theta = 0 \quad \text{on} \;\; \mathcal{B}, \tag{2.1.1b}$$

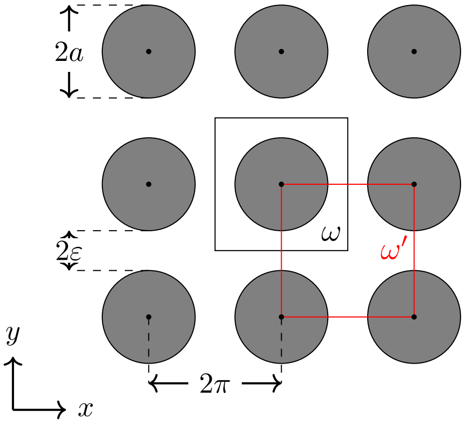

Figure 2.1: Square lattice of circular obstacles indicating the problem's geometric parameters and the two alternative elementary cells ω and ω' used in the analysis. The obstacles have radius a and are separated by gaps of width 2ε, hence $a = \pi - \epsilon$.

Here the pore space is defined as

$$\Omega = \mathbb{R}^2 \backslash \bigcup_{\boldsymbol{m}} \bar{\mathcal{B}}(\boldsymbol{r}^{(\boldsymbol{m})}). \tag{2.1.1c}$$

We are interested in the initial-value problem corresponding to the instantaneous release of the scalar at some location $\boldsymbol{x}_0$ outside the obstacles, and assume that the solution decays at infinity. Our aim is to provide a coarse-grained description of $\theta(\boldsymbol{x}, t)$, that goes beyond homogenisation and captures the tails of the scalar distribution. This can be achieved by applying ideas of large-deviation theory (e.g. [86]), adapting the approach developed by [40] for transport in periodic fluid flow to the diffusion with obstacles (2.1.1). We first introduce the approach in §2.2. This yields a family of eigenvalue problems whose solution provides an approximation to the concentration $\theta(\boldsymbol{x}, t)$ that is valid for $|\boldsymbol{x} - \boldsymbol{x}_0| = O(t)$, thus improving on homogenisation. We next study the eigenvalue problems numerically using the finite element method in §2.4.1.

In §§2.4–2.7, we focus on circular obstacles in the geometry of Figure 2.1 and obtain explicit results demonstrating the value of the large-deviation approach. We first solve the family of eigenvalue problems numerically for different obstacle area fractions σ (§2.4.2). The results show that diffusion with κ_{eff} provides a satisfactory approximation of the concentration tails only in the dilute limit $\sigma \to 0$; for general σ and, most markedly in the dense limit $\sigma \to \pi/4$, the tails are much fatter than predicted by the diffusive approximation and display some anisotropy, unlike the Gaussian core of the distribution. To explore this further, we examine the dense limit in detail in §2.7, where we develop an asymptotic theory which extends Keller's result (1.3.11) to the large-deviation regime. This theory, based on a matched-asymptotics treatment of the large-deviation eigenvalue problems, recovers and subsumes a more straightforward extension, which replaces the continuous geometry by that of a network [18] and captures part of the concentration tails. We assess the ranges of validity of the various approximations and test them against numerical solutions of the eigenvalue problems. We conclude the chapter in §2.8.

2.2 Large-deviation approximation

Our goal here is to obtain an approximation for the concentration $\theta(\boldsymbol{x}, t)$ for long times $t \gg 1$. This can be achieved by the theory of large deviations [37, 36, 86] applied to periodic environments which indicates that it takes the two-scale form (1.4.1) [40, 87] repeated here for convenience

$$\theta(\boldsymbol{x}, t) = \phi(\boldsymbol{x}, \boldsymbol{\xi}, t)\, \mathrm{e}^{-tg(\boldsymbol{\xi})}, \quad \text{where} \quad \boldsymbol{\xi} = \frac{\boldsymbol{x} - \boldsymbol{x}_0}{t} \in \mathbb{R}^2 \tag{2.2.1}$$

and $\boldsymbol{x}_0$ is the location of the initial scalar release, such that $\theta(\boldsymbol{x},0)=\delta(\boldsymbol{x}-\boldsymbol{x}_0)$. Here g is a rate (or Cramér) function which provides a continuous approximation for the most rapid changes in θ. It is non-negative, convex, and has a single minimum and zero located at $\boldsymbol{\xi}=\mathbf{0}$ that yields the maximum of θ in the limit of $t\to\infty$. The (positive) correction term ϕ (with $\ln\phi=o(t)$ as $t\to\infty$) has the same periodicity as the lattice,

$$\phi(\boldsymbol{x}+\boldsymbol{r}^{(\boldsymbol{m})},\boldsymbol{\xi},t)=\phi(\boldsymbol{x},\boldsymbol{\xi},t), \tag{2.2.2}$$

where $\boldsymbol{r}^{(\boldsymbol{m})}$ (see equation (1.2.1)) denotes the positions of the centroids of the obstacles.

Equation (2.2.1) introduces the vector $\boldsymbol{\xi}=(\xi,\eta)^{\mathrm{T}}$ defined on the whole of $\mathbb{R}^2$ which captures variations on scales large compared with the size of the lattice cells. The vector $\boldsymbol{x}$, in contrast, is defined on the multiply-connected domain obtained by excising the obstacles from $\mathbb{R}^2$ and captures variations on the scale of single lattice cells. The large separation between the two scales allows $\boldsymbol{x}$ and $\boldsymbol{\xi}$ to be treated as independent. We now employ (2.2.1) inside (2.1.1) using the chain rule to replace the time derivative and spatial gradient by

$$\frac{\partial}{\partial t}\to\frac{\partial}{\partial t}-\frac{1}{t}\boldsymbol{\xi}\cdot\nabla_{\boldsymbol{\xi}} \qquad \text{and} \qquad \nabla\to\nabla_{\boldsymbol{x}}+\frac{1}{t}\nabla_{\boldsymbol{\xi}}. \tag{2.2.3}$$

Equation (2.1.1a) is now

$$\begin{aligned}&\left(\nabla_{\boldsymbol{x}}^2-2\nabla_{\boldsymbol{\xi}}g\cdot\nabla_{\boldsymbol{x}}+|\nabla_{\boldsymbol{\xi}}g|^2-\boldsymbol{\xi}\cdot\nabla_{\boldsymbol{\xi}}g+g-\partial_t\right)\phi\\ &\qquad +t^{-1}\left((\boldsymbol{\xi}+2\nabla_{\boldsymbol{x}}-2\nabla_{\boldsymbol{\xi}}g)\cdot\nabla_{\boldsymbol{\xi}}-\nabla_{\boldsymbol{\xi}}^2g\right)\phi+t^{-2}\nabla_{\boldsymbol{\xi}}^2\phi=0\end{aligned} \tag{2.2.4a}$$

while the boundary conditions (2.1.1b) become

$$\boldsymbol{n}\cdot(\nabla_{\boldsymbol{x}}-\nabla_{\boldsymbol{\xi}}g+t^{-1}\nabla_{\boldsymbol{\xi}})\phi=0 \quad \text{on} \;\; \mathcal{B}. \tag{2.2.4b}$$

Substituting the expansion

$$\phi(\boldsymbol{x}, \boldsymbol{\xi}, t) = t^{-1}\left(\phi_0(\boldsymbol{x}, \boldsymbol{\xi}) + t^{-1}\phi_1(\boldsymbol{x}, \boldsymbol{\xi}) + t^{-2}\phi_2(\boldsymbol{x}, \boldsymbol{\xi}) + \ldots\right), \tag{2.2.5}$$

with the prefactor t^{-1} motivated by mass conservation [40], into (2.2.4) gives

$$\nabla_{\boldsymbol{x}}^2\phi_0 - 2\boldsymbol{p}\cdot\nabla_{\boldsymbol{x}}\phi_0 + |\boldsymbol{p}|^2\phi_0 = f(\boldsymbol{p})\phi_0, \quad \boldsymbol{x} \in \omega, \tag{2.2.6a}$$

at leading order, where we have defined

$$\boldsymbol{p} = (p, q) = \nabla_{\boldsymbol{\xi}} g(\boldsymbol{\xi}) \quad \text{and} \quad f(\boldsymbol{p}) = \boldsymbol{\xi}\cdot\nabla_{\boldsymbol{\xi}} g(\boldsymbol{\xi}) - g(\boldsymbol{\xi}). \tag{2.2.6b}$$

Here ω corresponds to the pore space inside the elementary cell. The associated boundary conditions are deduced from (2.2.4b) as follows:

$$\boldsymbol{n}\cdot(\nabla_{\boldsymbol{x}}\phi_0 - \boldsymbol{p}\phi_0) = 0 \quad \text{on} \;\; \mathcal{B}. \tag{2.2.6c}$$

Using (2.2.6d),

$$\phi_0(\boldsymbol{x} + \boldsymbol{r}^{(\boldsymbol{m})}, \boldsymbol{\xi}, t) = \phi_0(\boldsymbol{x}, \boldsymbol{\xi}, t). \tag{2.2.6d}$$

Equation (2.2.6) defines a family of eigenvalue problems parameterised by $\boldsymbol{p} = (p, q)$, which determine a discrete spectrum of eigenvalues $f(\boldsymbol{p})$. The eigenfunctions can be thought of as functions $\phi_0(\boldsymbol{x}, \boldsymbol{p})$, using the one-to-one correspondence between $\boldsymbol{\xi}$ and $\boldsymbol{p}$. The eigenvalue problems can alternatively be rewritten in terms of

$$\psi = e^{-\boldsymbol{p}\cdot\boldsymbol{x}}\phi_0. \tag{2.2.7}$$

Substituting (2.2.7) inside the eigenvalue equation (2.2.6a) we obtain

$$\begin{aligned}(f(\boldsymbol{p}) - |\boldsymbol{p}|^2)e^{\boldsymbol{p}\cdot\boldsymbol{x}}\psi &= \nabla_{\boldsymbol{x}}\cdot(e^{\boldsymbol{p}\cdot\boldsymbol{x}}(\boldsymbol{p} + \nabla_{\boldsymbol{x}})\psi) - 2e^{\boldsymbol{p}\cdot\boldsymbol{x}}\boldsymbol{p}\cdot(\boldsymbol{p} + \nabla_{\boldsymbol{x}})\psi \\ &= e^{\boldsymbol{p}\cdot\boldsymbol{x}}(|\boldsymbol{p}|^2 + 2\boldsymbol{p}\cdot\nabla_{\boldsymbol{x}} + \nabla_{\boldsymbol{x}}^2)\psi - 2e^{\boldsymbol{p}\cdot\boldsymbol{x}}(|\boldsymbol{p}|^2 + \boldsymbol{p}\cdot\nabla_{\boldsymbol{x}})\psi, \end{aligned} \tag{2.2.8a}$$

At the same time,

$$\boldsymbol{n} \cdot (e^{\boldsymbol{p}\cdot\boldsymbol{x}}(\boldsymbol{p} + \nabla_{\boldsymbol{x}})\psi - \boldsymbol{p}e^{\boldsymbol{p}\cdot\boldsymbol{x}}\psi) = 0. \tag{2.2.8b}$$

Upon simplification, (2.2.8a) and (2.2.8b) combine to become the modified Helmholtz problems

$$\nabla^2_{\boldsymbol{x}}\psi = f(\boldsymbol{p})\psi, \quad \boldsymbol{x} \in \omega, \tag{2.2.9a}$$

$$\boldsymbol{n} \cdot \nabla_{\boldsymbol{x}}\psi = 0 \quad \text{on } \mathcal{B}, \tag{2.2.9b}$$

involving Neumann conditions on the obstacles boundaries. It is important to note that unlike the function ϕ, ψ is not periodic in $\boldsymbol{x}$ but instead is a 'tilted' periodic function of $\boldsymbol{x}$. That is

$$\psi(\boldsymbol{x} + \boldsymbol{r}^{(\boldsymbol{m})}, \boldsymbol{p}) = e^{-\boldsymbol{p}\cdot\boldsymbol{r}^{(\boldsymbol{m})}}\psi(\boldsymbol{x}, \boldsymbol{p}). \tag{2.2.10}$$

We focus on the principal eigenvalue $f(\boldsymbol{p})$ of (2.2.6) or (2.2.9) , that is, the eigenvalue with maximum real part, with associated eigenfunction $\phi_0(\boldsymbol{x}, \boldsymbol{p})$ (unique up to multiplication). The Krein–Rutman theorem [52] implies that this eigenvalue is unique, simple and real. Moreover, $f \geqslant 0$ and convex. The rate function g is then deduced from f by Legendre transform since (2.2.6b) together with convexity implies that $f(\boldsymbol{p})$ and $g(\boldsymbol{\xi})$ are Legendre duals. Thus solving the family of eigenvalues problems (2.2.6) or (2.2.9) provide all the elements of the large-deviation approximation (2.2.1) of the scalar concentration.

The eigenvalue problem (2.2.6) or (2.2.9) cannot be solved analytically, even for simple obstacle shapes. A useful lower bound on g can however be obtained by multiplying

(2.2.6a) by ϕ_0, integrating by parts over an elementary cell ω

$$f(\boldsymbol{p}) \int_\omega \phi_0^2 \, d\boldsymbol{x} = \int_{\partial\omega} \phi_0 \boldsymbol{n} \cdot \nabla_{\boldsymbol{x}} \phi_0 \, dl - \int_\omega |\nabla_{\boldsymbol{x}} \phi_0|^2 \, d\boldsymbol{x} - 2 \int_\omega \phi_0 \boldsymbol{p} \cdot \nabla_{\boldsymbol{x}} \phi_0 \, d\boldsymbol{x} + |\boldsymbol{p}|^2 \int_\omega \phi_0^2 \, d\boldsymbol{x}. \tag{2.2.11}$$

Using the boundary (2.2.6c) and periodicity (2.2.6d) conditions gives

$$f(\boldsymbol{p}) \int_\omega \phi_0^2 \, d\boldsymbol{x} = - \int_\omega |\nabla_{\boldsymbol{x}} \phi_0|^2 \, d\boldsymbol{x} + |\boldsymbol{p}|^2 \int_\omega \phi_0^2 \, d\boldsymbol{x}. \tag{2.2.12}$$

Thus, we may deduce that

$$f(\boldsymbol{p}) \leqslant |\boldsymbol{p}|^2. \tag{2.2.13}$$

Taking the Legendre transform of (2.2.13) we obtain that

$$g(\boldsymbol{\xi}) \geqslant \frac{1}{4} |\boldsymbol{\xi}|^2. \tag{2.2.14}$$

Recall that $g(\boldsymbol{\xi}) = 1/4|\boldsymbol{\xi}|^2$ corresponds to the case of a uniform environment (i.e. in the absence of obstacles). Thus the presence of obstacles hinders dispersion [17, Th. 1.3] (note that f and therefore g may not vary monotonically with respect to the size of the obstacles [17, Th. 1.4]).

2.3 Relation between the effective diffusive approximation and the large-deviation approximation

The relationship between the large-deviation approach and homogenisation can be made completely explicit by noting that a perturbative solution of the eigenvalue problem (2.2.6) obtained by expanding for small $\boldsymbol{p}$, recovers at leading order, the cell problem of homogenisation that determines κ_{eff}. Assuming that the eigenvalue problem is sufficiently symmetric (the case for the four-fold symmetry of the lattice assumed here) we take a regular series expansion in powers of $|\boldsymbol{p}|$ for the eigenvalue $f(\boldsymbol{p})$, given by

$$f(\boldsymbol{p}) = \alpha^{(0)} + \alpha^{(1)}(\hat{\boldsymbol{p}})\,|\boldsymbol{p}| + \alpha^{(2)}(\hat{\boldsymbol{p}})\,|\boldsymbol{p}|^2 + O(|\boldsymbol{p}|^3), \quad \text{as } |\boldsymbol{p}| \to 0, \tag{2.3.1a}$$

and eigenfunction ϕ_0, given by

$$\phi_0(\boldsymbol{x},\boldsymbol{p}) = \phi_{0,0}(\boldsymbol{x}) + \phi_{0,1}(\boldsymbol{x},\hat{\boldsymbol{p}})\,|\boldsymbol{p}| + \phi_{0,2}(\boldsymbol{x},\hat{\boldsymbol{p}})\,|\boldsymbol{p}|^2 + O(|\boldsymbol{p}|^3), \quad \text{as } |\boldsymbol{p}| \to 0. \tag{2.3.1b}$$

Introducing (2.3.1) into the eigenvalue problems (2.2.6) yields a series of problems in increasing powers of $|\boldsymbol{p}|$. At leading order we obtain

$$\nabla^2_{\boldsymbol{x}}\phi_{0,0} = \alpha^{(0)}\phi_{0,0}, \quad \boldsymbol{x} \in \omega, \tag{2.3.2a}$$

$$\boldsymbol{n}\cdot\nabla_{\boldsymbol{x}}\phi_{0,0} = 0 \quad \text{on } \mathcal{B}, \tag{2.3.2b}$$

$$\phi_{0,0}(\boldsymbol{x} + \boldsymbol{r}^{(\boldsymbol{m})}) = \phi_{0,0}(\boldsymbol{x}). \tag{2.3.2c}$$

At $O(|\boldsymbol{p}|)$ we obtain

$$\nabla^2_{\boldsymbol{x}}\phi_{0,1} - 2\hat{\boldsymbol{p}}\cdot\nabla_{\boldsymbol{x}}\phi_{0,0} = \alpha^{(0)}\phi_{0,1} + \alpha^{(1)}\phi_{0,0}, \quad \boldsymbol{x} \in \omega, \tag{2.3.3a}$$

$$\boldsymbol{n}\cdot(\nabla_{\boldsymbol{x}}\phi_{0,1} - \hat{\boldsymbol{p}}\phi_{0,0}) = 0 \quad \text{on } \mathcal{B}, \tag{2.3.3b}$$

$$\phi_{0,1}(\boldsymbol{x} + \boldsymbol{r}^{(\boldsymbol{m})}) = \phi_{0,1}(\boldsymbol{x}), \tag{2.3.3c}$$

where $\hat{\boldsymbol{p}} = \boldsymbol{p}/|\boldsymbol{p}|$. At $O(|\boldsymbol{p}|^2)$ we obtain

$$\nabla^2_{\boldsymbol{x}}\phi_{0,2} - 2\hat{\boldsymbol{p}}\cdot\nabla_{\boldsymbol{x}}\phi_{0,1} + \phi_{0,0} = \alpha^{(0)}\phi_{0,2} + \alpha^{(1)}\phi_{0,1} + +\alpha^{(2)}\phi_{0,0}, \quad \boldsymbol{x} \in \omega, \tag{2.3.4a}$$

$$\boldsymbol{n}\cdot(\nabla_{\boldsymbol{x}}\phi_{0,2} - \hat{\boldsymbol{p}}\phi_{0,1}) = 0 \quad \text{on } \mathcal{B}, \tag{2.3.4b}$$

$$\phi_{0,2}(\boldsymbol{x} + \boldsymbol{r}^{(\boldsymbol{m})}) = \phi_{0,2}(\boldsymbol{x}). \tag{2.3.4c}$$

Integrating (2.3.2a) over an elementary cell ω gives

$$\int_\omega \nabla^2_{\boldsymbol{x}} \phi_{0,0}\, d\boldsymbol{x} = \int_{\mathcal{B}} \boldsymbol{n} \cdot \nabla_{\boldsymbol{x}} \phi_{0,0}\, dl = \alpha^{(0)} \int_\omega \phi_{0,0}\, d\boldsymbol{x}, \tag{2.3.5}$$

where the first equality is obtained by using the divergence theorem together with (2.3.2c). The Neumann boundary conditions (2.3.2b) imply that $\alpha^{(0)} = 0$. This means the problem at leading order is a Laplacian problem and by the maximum principle it has a solution that is constant in $\boldsymbol{x}$. Without loss of generality we normalise $\phi_{0,0}$ by taking $\phi_{0,0} = 1$. Equation (2.3.3a) now reduces to

$$\nabla^2_{\boldsymbol{x}} \phi_{0,1} = \alpha^{(1)}. \tag{2.3.6}$$

Integrating (2.3.6) over the elementary cell we obtain

$$\int_\omega \nabla^2_{\boldsymbol{x}} \phi_{0,1}\, d\boldsymbol{x} = \int_{\mathcal{B}} \boldsymbol{n} \cdot \nabla_{\boldsymbol{x}} \phi_{0,1}\, dl - \hat{\boldsymbol{p}} \cdot \int_{\mathcal{B}} \boldsymbol{n}\, dl = 0 = \int_\omega \alpha^{(1)}\, d\boldsymbol{x} = \alpha^{(1)}\sigma. \tag{2.3.7}$$

We once more use divergence theorem and periodicity (2.3.3c) to obtain the first equality. We then use (2.3.3b) to obtain the second equality. The last equality holds for all simply connected obstacles. This yields $\alpha^{(1)} = 0$. We may express $\phi_{0,1}$ as

$$\phi_{0,1} = -\hat{\boldsymbol{p}} \cdot \boldsymbol{\chi}, \tag{2.3.8}$$

where $\boldsymbol{\chi}$ is periodic in $\boldsymbol{x}$. Then the problem at $O(|\boldsymbol{p}|)$ becomes

$$\nabla^2_{\boldsymbol{x}} \boldsymbol{\chi} = \boldsymbol{0}, \quad \boldsymbol{x} \in \omega, \tag{2.3.9a}$$

$$\boldsymbol{n} \cdot \nabla_{\boldsymbol{x}} \boldsymbol{\chi} + \boldsymbol{n} = \boldsymbol{0} \quad \text{on } \mathcal{B}, \tag{2.3.9b}$$

which we recognise as the cell problem in homogenisation (or equation (1.3.8) when $\boldsymbol{u} = \boldsymbol{0}$, see e.g. [68], for derivation). Integrating equation (2.3.4a) we obtain

$$\nabla^2_{\boldsymbol{x}} \phi_{0,2} - 2\hat{\boldsymbol{p}} \cdot \nabla_{\boldsymbol{x}} \phi_{0,1} + 1 = \alpha^{(2)}, \tag{2.3.10}$$

and using (2.3.4c),(2.3.4b) together with (2.3.9) we obtain after simplification

$$\alpha^{(2)} = 1 + \hat{\boldsymbol{p}}^T \langle \nabla_{\boldsymbol{x}} \boldsymbol{\chi} \rangle \hat{\boldsymbol{p}}, \tag{2.3.11}$$

where $\langle \nabla \boldsymbol{\chi} \rangle$ is the spatial average of $\nabla \boldsymbol{\chi}$ of the elementary cell. Thus

$$(\kappa_{\text{eff}})_{ij} = \delta_{ij} + \langle \nabla_{\boldsymbol{x}} \boldsymbol{\chi}_{ij} \rangle, \tag{2.3.12}$$

reproducing the standard homogenisation result. Explicit expressions for κ_{eff} only exist for limiting cases (see §1.3).

2.4 Circular obstacles in square lattices

We now focus on the solution to the eigenvalue problems for the particular case of a square lattice configuration. We first focus on the numerical method that we use to approximate the eigenvalue problems. We then present numerical results followed by results obtained using asymptotic analysis.

2.4.1 Numerical method

We here obtain a numerical solution to the eigenvalue problem (2.2.6). We focus on the simple geometry of Figure 2.1, with circular obstacles of radius a arranged in square lattices with sides 2π, so that

$$\boldsymbol{r}^{(\boldsymbol{m})} = 2\pi(m_1 \boldsymbol{e}_1 + m_2 \boldsymbol{e}_2), \tag{2.4.1}$$

where m_1, m_2 are integers denoting the positions of the centroids of the obstacles. Then the solid area fraction σ, satisfies

$$\sigma = \frac{a^2}{4\pi} \leqslant \sigma_c = \frac{\pi}{4}, \tag{2.4.2}$$

where σ_c is the critical value obtained for $a = \pi$, corresponding to when the obstacles touch. Observe $\partial\omega$ is composed of two boundaries: the boundary of the circle $\mathcal{B}$ and the square boundary.

The finite element method [54, 45, 19] is widely employed in boundary value problems involving complex geometries for which closed form solutions are inaccessible. It allows for efficient and accurate approximations. The essence of the method requires to use a weak formulation of the eigenvalue problem (2.2.6). An approximation to the latter is then sought in the space of continuous piecewise linear polynomials defined on a quasi-uniform triangular subdivision of the domain obtained using Matlab's PDE Toolbox. This results in a large, sparse generalised matrix eigenvalue problem which is solved using the Shift-and-Invert method [74].

Weak form of the eigenvalue problem

A weak form of the eigenvalue problem (2.2.6) is readily obtained by considering φ to be a general test function (square-integrable, including its derivatives) satisfying the same periodicity condition (2.2.6d) as ϕ_0. Multiplying (2.2.6a) by φ and integrating over ω we get

$$(f(\boldsymbol{p}) - |\boldsymbol{p}|^2) \int_\omega \phi_0 \varphi \, d\boldsymbol{x} = \int_\omega (\nabla_{\boldsymbol{x}}^2 \phi_0 - 2\boldsymbol{p} \cdot \nabla_{\boldsymbol{x}} \phi_0) \varphi \, d\boldsymbol{x}. \tag{2.4.3}$$

Integrating by parts and using Green's identity gives

$$\begin{aligned}(f(\boldsymbol{p})-|\boldsymbol{p}|^2)\int_\omega \phi_0\varphi\,d\boldsymbol{x} &= \int_{\partial\omega}\boldsymbol{n}\cdot\nabla_{\boldsymbol{x}}\phi_0\varphi\,dl - \int_\omega \nabla_{\boldsymbol{x}}\phi_0\cdot\nabla_{\boldsymbol{x}}\varphi\,d\boldsymbol{x}\\ &-\int_\omega \boldsymbol{p}\cdot\nabla_{\boldsymbol{x}}\phi_0\varphi\,d\boldsymbol{x} - \int_{\partial\omega}\boldsymbol{p}\cdot\boldsymbol{n}\phi_0\varphi\,dl + \int_\omega \boldsymbol{p}\cdot\nabla_{\boldsymbol{x}}\varphi\phi_0\,d\boldsymbol{x}. \qquad (2.4.4)\end{aligned}$$

We now use the periodicity of both ϕ_0 and φ to deduce that

$$\int_{\partial\omega}\boldsymbol{n}\cdot\nabla_{\boldsymbol{x}}\phi_0\varphi\,dl = \int_{\mathcal{B}}\boldsymbol{n}\cdot\nabla_{\boldsymbol{x}}\phi_0\varphi\,dl, \qquad (2.4.5)$$

since contributions along opposing edges of the square boundary cancel. Similarly

$$\int_{\partial\omega}\boldsymbol{p}\cdot\boldsymbol{n}\phi_0\varphi\,dl = \int_{\mathcal{B}}\boldsymbol{p}\cdot\boldsymbol{n}\phi_0\varphi\,dl. \qquad (2.4.6)$$

Inserting (2.4.5) and (2.4.6) into (2.4.4) we get

$$(f(\boldsymbol{p})-|\boldsymbol{p}|^2)\int_\omega \phi_0\varphi\,d\boldsymbol{x} = \int_{\mathcal{B}}(\boldsymbol{n}\cdot\nabla_{\boldsymbol{x}}\phi_0 - \boldsymbol{p}\cdot\boldsymbol{n}\phi_0)\varphi\,dl - \int_\omega \nabla_{\boldsymbol{x}}\phi_0\cdot\nabla_{\boldsymbol{x}}\varphi\,d\boldsymbol{x} \qquad (2.4.7)$$

$$+\int_\omega \boldsymbol{p}\cdot\nabla_{\boldsymbol{x}}\varphi\phi_0\,d\boldsymbol{x} - \int_\omega \boldsymbol{p}\cdot\nabla_{\boldsymbol{x}}\phi_0\varphi\,d\boldsymbol{x}. \qquad (2.4.8)$$

Upon application of the boundary (2.2.6c) condition on $\mathcal{B}$, we obtain that

$$(f(\boldsymbol{p})-|\boldsymbol{p}|^2)\int_\omega \phi_0\varphi\,d\boldsymbol{x} = -\int_\omega \nabla_{\boldsymbol{x}}\phi_0\cdot\nabla_{\boldsymbol{x}}\varphi\,d\boldsymbol{x} + \int_\omega \boldsymbol{p}\cdot\nabla_{\boldsymbol{x}}\varphi\phi_0\,d\boldsymbol{x} - \int_\omega \boldsymbol{p}\cdot\nabla_{\boldsymbol{x}}\phi_0\varphi\,d\boldsymbol{x}. \qquad (2.4.9)$$

It is convenient to define $a(\phi_0,\varphi)$ and $m(\phi_0,\varphi)$ where

$$a(\phi_0,\varphi) = -\int_\omega \nabla_{\boldsymbol{x}}\phi_0\cdot\nabla_{\boldsymbol{x}}\varphi\,d\boldsymbol{x} + \int_\omega \boldsymbol{p}\cdot\nabla_{\boldsymbol{x}}\varphi\phi_0\,d\boldsymbol{x} - \int_\omega \boldsymbol{p}\cdot\nabla_{\boldsymbol{x}}\phi_0\varphi\,d\boldsymbol{x}, \qquad (2.4.10a)$$

and

$$m(\phi_0,\varphi) = \int_\omega \phi_0\varphi\,d\boldsymbol{x}. \qquad (2.4.10b)$$

Then the variational formulation of the eigenvalue problem reads:

$$a(\phi_0,\varphi) = \mu m(\phi_0,\varphi), \qquad (2.4.11)$$

where $\mu = f(\boldsymbol{p}) - |\boldsymbol{p}|^2$.

Finite element approximation

Our next task is to construct a discrete approximation to the solution of the variational problem (2.4.11). To that end we introduce a mesh on the domain ω. Let $\mathcal{T}_h$ denote a quasi-uniform subdivision of ω into simplices K_j, where $j = 1, \ldots, n$. We choose these to be non-overlapping triangles K_j such that no vertex of one triangle touches the edge of another. To define the mesh parameter h (measuring how fine the mesh is) we introduce the notion of the local mesh size h_{K_j}, defined as the area of the triangle K_j. Then $h = \max_{\{K_j \in \mathcal{T}_h\}} h_{K_j}$. The vertices of the triangles coincide at points or nodes $N_i = (x^{(i)}, y^{(i)})$, where $i = 1, \ldots, M$ of the mesh. Here M is the total number of nodes of the mesh. We assume that parallel sides of the square domain are equally subdivided. This allows periodicity to be incorporated in a straightforward manner. A quasi-uniform triangular subdivision is in practise achieved using Matlab's PDE Toolbox.

We here use the Ritz–Galerkin method [54, 45] to convert the weak formulation of the eigenvalue problem (2.2.6) into a discrete matrix formulation. We approximate $\phi_0(\boldsymbol{x})$ and $\varphi(\boldsymbol{x})$ by continuous piecewise linear functions $\phi_{0,h}(\boldsymbol{x})$ and $\varphi_h(\boldsymbol{x})$, both of which share the same periodicity as $\phi_0(\boldsymbol{x})$. Thus, (2.4.11) takes the discretised form

$$a(\phi_{0,h}, \varphi_h) = \mu m(\phi_{0,h}, \varphi_h). \tag{2.4.12}$$

The finite element approximation $\phi_{0,h}$ is computed by expressing it as a linear combination of the basis functions $\{\phi_j\}_{j=1}^{M}$ such that

$$\phi_{0,h} = \sum_{j=1}^{M} u_j \phi_j, \tag{2.4.13}$$

for which there are M unknown constants u_j to be determined. Here ϕ_j are the nodal basis functions, defined by

$$\phi_j(N_i) = \begin{cases} 1 & i = j \\ 0 & i \neq j \end{cases} \qquad i, j = 1, 2, \ldots, M. \tag{2.4.14}$$

As a result the basis functions has local support on the set of triangles sharing the node N_j. Similarly the test function φ_h can be written in terms of the same set of basis functions. Inserting (2.4.13) into (2.4.12), we find that the function $a(\phi_{0,h}, \phi_i)$ becomes

$$\begin{aligned} a(\phi_{0,h}, \phi_i) &= -\int_\omega \nabla_{\boldsymbol{x}}\phi_{0,h} \cdot \nabla_{\boldsymbol{x}}\phi_i \, d\boldsymbol{x} + \boldsymbol{p} \cdot \int_\omega \left(\nabla_{\boldsymbol{x}}\phi_i \phi_{0,h} - \nabla_{\boldsymbol{x}}\phi_{0,h}\phi_i\right) \, d\boldsymbol{x} \\ &= -\int_\omega \nabla_{\boldsymbol{x}} \left(\sum_{j=1}^M u_j\phi_j\right) \cdot \nabla_{\boldsymbol{x}}\phi_i + \boldsymbol{p} \cdot \left(\nabla_{\boldsymbol{x}}\phi_i \left(\sum_{j=1}^M u_j\phi_j\right) - \nabla_{\boldsymbol{x}} \left(\sum_{j=1}^M u_j\phi_j\right)\phi_i\right) d\boldsymbol{x} \\ &= \sum_{j=1}^M u_j \left(-\int_\omega \nabla_{\boldsymbol{x}}\phi_j \cdot \nabla_{\boldsymbol{x}}\phi_i \, d\boldsymbol{x} + \boldsymbol{p} \cdot \int_\omega \left(\nabla_{\boldsymbol{x}}\phi_i\phi_j - \nabla_{\boldsymbol{x}}\phi_j\phi_i\right) \, d\boldsymbol{x}\right), \quad i = 1, \ldots, M, \end{aligned} \tag{2.4.15}$$

and $m(\phi_{0,h}, \phi_i)$ becomes

$$m(\phi_{0,h}, \phi_i) = \int_\omega \phi_{0,h}\phi_i \, d\boldsymbol{x} = \int_\omega \left(\sum_{j=1}^M u_j\phi_j\right)\phi_i \, d\boldsymbol{x} = \sum_{j=1}^M u_j \left(\int_\omega \phi_j\phi_i\right) \, d\boldsymbol{x}, \quad i = 1, \ldots, M. \tag{2.4.16}$$

Now using the notation

$$A_{ij} = -\int_\omega \nabla_{\boldsymbol{x}}\phi_j \cdot \nabla_{\boldsymbol{x}}\phi_i \, d\boldsymbol{x} + \boldsymbol{p} \cdot \int_\omega \left(\nabla_{\boldsymbol{x}}\phi_i\phi_j - \nabla_{\boldsymbol{x}}\phi_j\phi_i\right) \, d\boldsymbol{x}, \quad i, j = 1, \ldots, M \tag{2.4.17}$$

$$M_{ij} = \int_\omega \phi_j\phi_i \, d\boldsymbol{x}, \quad i, j = 1, \ldots, M, \tag{2.4.18}$$

we find that (2.4.12) becomes a generalised algebraic eigenvalue problem of the form

$$A\boldsymbol{u} = \mu M\boldsymbol{u}. \tag{2.4.19}$$

with $A, M \in \mathbb{R}^{M\times M}$ entries defined by (2.4.17) and (2.4.18), respectively. As is convention A is called the *stiffness matrix* and M is called the *mass matrix* and $\boldsymbol{u} \in \mathbb{R}^M$ is a vector holding the nodal values of $\phi_{0,h}$. In practise they are constructed by the assembly of the *elemental matrices* A^{K_l} and M^{K_l} which determine contributions from each triangle K_l for $l = 1, \ldots, n$. For the stiffness matrix this process is represented as

$$A = \sum_{l=1}^{n} - \int_{K_l} \nabla_{\boldsymbol{x}} \phi_j \cdot \nabla_{\boldsymbol{x}} \phi_i \, d\boldsymbol{x} + \boldsymbol{p} \cdot \int_{K_l} (\nabla_{\boldsymbol{x}} \phi_i \phi_j - \nabla_{\boldsymbol{x}} \phi_j \phi_i) \, d\boldsymbol{x} = \sum_{l=1}^{n} A^{K_l}, \tag{2.4.20}$$

and for the mass matrix

$$M = \sum_{l=1}^{n} \int_{K_l} \phi_j \phi_i \, d\boldsymbol{x} = \sum_{l=1}^{n} M^{K_l}. \tag{2.4.21}$$

Notably the entries of $A_{ij}, M_{ij} \neq 0$ if and only if the nodes N_j and N_i are vertices of triangle K_l i.e. the local support of ϕ_j and ϕ_i overlap in K_l. There are three non-zero basis functions on each triangle. Therefore for each elemental matrices A^{K_l} and M^{K_l} only a small 3×3 local element matrix are formed for storing their non-zero entries.

The computation of A^{K_l} and M^{K_l} is aided by mapping the triangles K_l to the canonical triangle $\bar{K}$ with nodes at $(0,0), (1,0), (0,1)$. Consider a single triangle K_l with nodes with position N_i for $i = 1, \ldots, 3$. A coordinate transformation implies that the elemental mass matrix may be expressed as

$$M^{K_l} = \int_{K_l} \phi_j \phi_i \, dx dy = \int_{\bar{K}} \varphi_j \varphi_i |J| \, d\bar{x}\bar{y}, \tag{2.4.22}$$

where $\varphi_i(\bar{x}, \bar{y}) = \phi_i(x(\bar{x}, \bar{y}), y(\bar{x}, \bar{y}))$ are the canonical basis functions (or shape functions) defined for linears as

$$\varphi_1(\bar{x}, \bar{y}) = 1 - \bar{x} - \bar{y}, \quad \varphi_2(\bar{x}, \bar{y}) = \bar{x}, \quad \varphi_3(\bar{x}, \bar{y}) = \bar{y}. \tag{2.4.23}$$

Then the Jacobian of the transformation $J = \partial(x, y)/\partial(\bar{x}, \bar{y})$ has a determinant which can be shown to be $|J| = 2|K_l|$ where $|K_l|$ is the area of triangle K_l. Similar construction applies to the elemental stiffness matrix A^K. Finally the integrals of the local element matrices A^{K_l} and M^{K_l} are computed using the Gauss rule [71]. They are then added to the appropriate entries of the global matrices A and M.

We finally enforce periodic boundary conditions on the system (2.4.19) by coupling nodes on opposing edges of the square boundary through constraint equations. We demonstrate periodicity on the eastern and western edges of the square boundary. Now consider the eigenvalue problem (2.4.19) and rewrite as

$$\begin{bmatrix} A_{ww} & A_{wi} & A_{we} \\ A_{iw} & A_{ii} & A_{ie} \\ A_{ew} & A_{ei} & A_{ee} \end{bmatrix} \begin{bmatrix} u_w \\ u_i \\ u_e \end{bmatrix} = \mu \begin{bmatrix} M_{ww} & M_{wi} & M_{we} \\ M_{iw} & M_{ii} & M_{ie} \\ M_{ew} & M_{ei} & M_{ee} \end{bmatrix} \begin{bmatrix} u_w \\ u_i \\ u_e \end{bmatrix}, \tag{2.4.24}$$

where u_w, u_e are the nodal values of $\phi_{0,h}$ on the western and eastern edges of the square boundary and u_i are the remaining nodal values on ω. Adding the first row to the last and applying periodicity (i.e. $u_e - u_w = 0$) we obtain

$$\begin{bmatrix} A_{ww} & A_{wi} & A_{we} \\ A_{iw} & A_{ii} & A_{ie} \\ A_{ew} - A_{ww} & A_{ei} - A_{wi} & A_{ee} - A_{we} \end{bmatrix} \begin{bmatrix} u_w \\ u_i \\ 0 \end{bmatrix} = \mu \begin{bmatrix} M_{ww} & M_{wi} & M_{we} \\ M_{iw} & M_{ii} & M_{ie} \\ M_{ew} - M_{ww} & M_{ei} - M_{wi} & M_{ee} - M_{we} \end{bmatrix} \begin{bmatrix} u_w \\ u_i \\ 0 \end{bmatrix}. \tag{2.4.25}$$

Now we can eliminate the final column of the matrices to obtain a reduced system given by

$$\begin{bmatrix} A_{ww} & A_{wi} \\ A_{iw} & A_{ii} \end{bmatrix} \begin{bmatrix} u_w \\ u_i \end{bmatrix} = \mu \begin{bmatrix} M_{ww} & M_{wi} \\ M_{iw} & M_{ii} \end{bmatrix} \begin{bmatrix} u_w \\ u_i \end{bmatrix}. \tag{2.4.26}$$

In a similar fashion we apply periodicity constraints to the corner nodes and to the south and north edges of the square boundary. The periodicity constraints imply that all four corner nodes are identical. The periodicity constraints reduce the overall size of the mass and stiffness matrices to $(M - s/2) \times (M - s/2)$ and the vector $\boldsymbol{u}$ to $(M - s/2)$ where s denotes the number of nodes on the square boundary of ω.

We now determine the principal eigenfunction of (2.4.19). The problem is simulated using MATLAB and its PDE Toolbox (see [55] for the numerical code). The large sparse matrices involved call for a single vector iteration scheme, i.e. involving a single sequence of vectors [74]. These standard methods include the power method which is the simplest single vector technique which converges to the principal eigenfunction. There is also the shift-and-power method which generalises the previous method to include a shift parameter. The shift parameter is suitably selected so that it maximises the asymptotic convergence rate. Therefore this method can converge more efficiently than the power method. We use the shift-and-invert method which is an adaptation of the previous two methods. This method uses the inverse of the system matrix to perform iterations. It is best suited to our generalised eigenvalue problem (2.4.19) since it has a high convergence rate [74]. The computation relies on a good initial guess for the principal eigenvalue. We first focus on small values of $|\boldsymbol{p}|$ e.g. $\boldsymbol{p} = (0, 0.001)$ and use $f(\mathbf{0}) = 0$ as an initial guess for e.g. $f(0, 0.001)$. We then iterate over a range of values of $\boldsymbol{p}$ using the previously determined solution as an initial guess to find the next solution. We anticipate a linear dependence of f on $\boldsymbol{p}$ for large $|\boldsymbol{p}|$ and a quadratic dependence of f on $\boldsymbol{p}$ for small $|\boldsymbol{p}|$ (both behaviours are obtained asymptotically, see sections 2.6 and 2.7). For this reason, we carry out the computation on a non-uniform grid $\boldsymbol{p}$ with step size 0.001 for $|\boldsymbol{p}| < 0.01$, step size 0.01 for $0.01 \leqslant |\boldsymbol{p}| < 1$ and step size 0.1 otherwise. We then determine g as a function of $\boldsymbol{\xi}$ by using finite differences to approximate the Legendre transform.

2.4.2 Numerical results

We now present our numerical findings and compare against the effective diffusivity approximations. We consider the three obstacle radii $a = 0.01$, $\pi/2$ and $\pi - 0.01$. The value $a = 0.01$ is representative of the dilute limit $a \ll 1$, the value $a = \pi - 0.01$ of the dense limit $\pi - a \ll 1$, with the area fraction close to the maximum $\sigma = \pi/4$ allowed by the lattice arrangement. For these configurations we construct meshes generated via triangulation of ω which is utilised for the finite element procedure. We control the mesh refinement parameter h by choosing the maximum area of the triangular elements in ω. For the three obstacle radii considered and in order of increasing radius we take $h = 0.06, 0.01$ and 3.4×10^{-4}, respectively. Note that for the dense case we need to use a very fine mesh to capture the large gradients for ϕ_0 localised in the thin gaps between neighbouring obstacles. We justify the choice of mesh refinement by noting that further reducing h only introduces small relative errors in f. For example in the dense case reducing the value of h by a 1/4 results in a relative error of 0.09%.

Figure 2.2 shows the eigenfunction ϕ_0 for the three obstacle radii and $\boldsymbol{\xi} = |\boldsymbol{\xi}|(1,1)/\sqrt{2}$ for $|\boldsymbol{\xi}| = 0.01, 1$ and 2. As expected, for all three cases ϕ_0 remains approximately uniform for small $|\boldsymbol{\xi}|$ (see left column in Figure 2.2). In the dilute case (Figure 2.2a), ϕ_0 departs from uniformity in the small region surrounding the obstacle. It behaves as a dipole centred at the obstacle centre. This behaviour is consistent with results obtained using homogenisation theory [69]. In the dense case (Figure 2.2g), ϕ_0's departure from non-uniformity takes place inside the small gaps of neighbouring obstacles wherein the gradients are uni-directional and transversely uniform. This behaviour is consistent

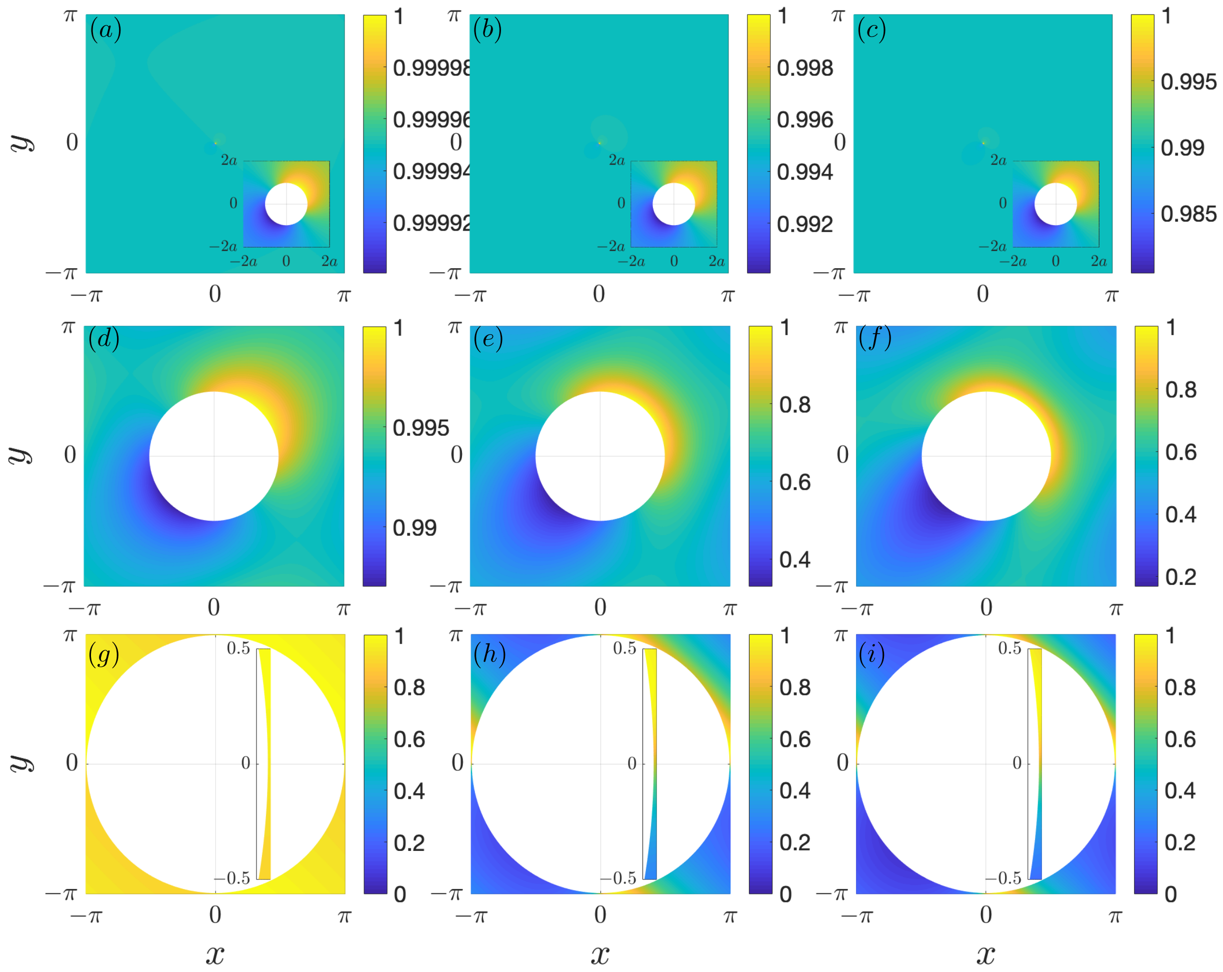

Figure 2.2: Normalised eigenfunctions ϕ_0 obtained numerically on the domain ω for square lattices of circular obstacles with radius (bottom) $a = 0.01$, (middle) $\pi/2$ and (top) $\pi - 0.01$ (gap half width $\epsilon = 0.01$) are shown along the direction $(1, 1)$ for $|\boldsymbol{\xi}| = 0.01$ (left), 1 (centre) and 2 (right). The magnified insets focus on the boundary layer behaviour.

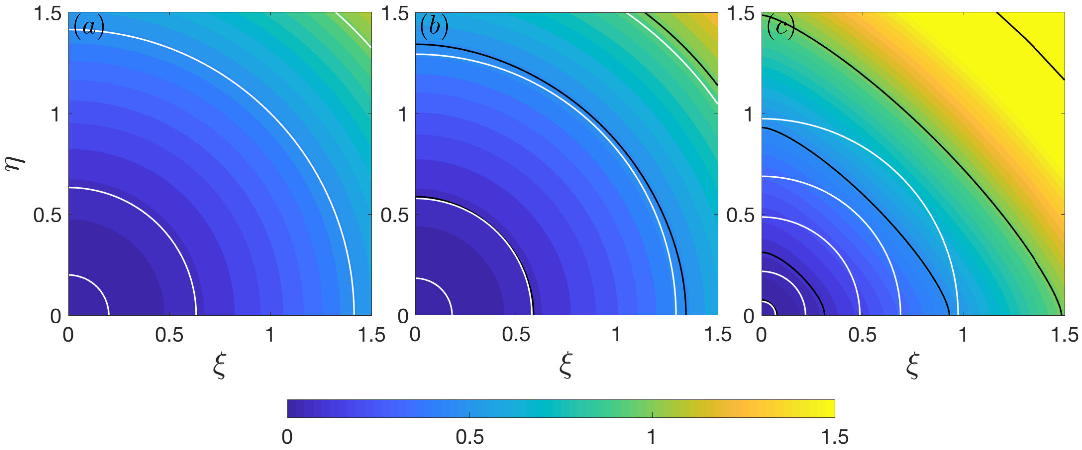

Figure 2.3: Rate function g plotted as a function of $\boldsymbol{\xi}$ for square lattices of circular obstacles with radius (left) $a = 0.01$, (middle) $\pi/2$ and (right) $\pi - 0.01$ (gap half width $\varepsilon = 0.01$). Selected contours (with values 0.01, 0.1, 0.5, 1 and 2) compare g (black) with its quadratic (Gaussian) approximation (white) with the effective diffusivity κ_{eff} given by the Maxwell formula (1.3.10) (left), a best-fit estimate (middle) and the Keller formula (1.3.11) (right).

with Keller's prediction developed by essentially using homogenisation theory [46]. In the dilute case, the eigenfunction remains approximately uniform beyond the small-$|\boldsymbol{\xi}|$ regime (top row in Figure 2.2). This is no longer the case for the intermediate and dense cases. This is particularly true for the dense case. Figure 2.2i shows that large uni-directional and transversely uniform gradients continue to take place inside the small gaps of neighbouring obstacles. Away from these gaps, the behaviour becomes increasingly non-uniform with $\boldsymbol{\xi}$. This behaviour is distinctly different to expected behaviour obtained using homogenisation theory.

Figure 2.3 shows the rate function obtained for the same three obstacle radii for $\boldsymbol{\xi}$ in the first quadrant (the other three quadrants are obtained from symmetry). The figure illustrates interesting features, such as anisotropy, which is absent for small obstacles (Figure 2.3a) but very marked for the largest obstacles (Figure 2.3c). As expected, the quadratic approximation (1.4.3) of $g(\boldsymbol{\xi})$ with effective diffusivity given by the Maxwell formula (1.3.10) in the dilute limit (Figure 2.3a) or the Keller formula (1.3.11) in the dense limit (Figure 2.3b) is accurate near $\boldsymbol{\xi} = \mathbf{0}$. In the intermediate case, the quadratic behaviour also holds near $\boldsymbol{\xi} = \mathbf{0}$ with an effective diffusivity that can be inferred from our results by contour fitting as an alternative to solving the cell problem of discretisation theory [69]. Remarkably, in the dilute case, the quadratic approximation is excellent beyond the small-$\boldsymbol{\xi}$ neighbourhood and applies to the entire range of $\boldsymbol{\xi}$ shown. In general and most strikingly in the dense case, g is a more complicated function of $\boldsymbol{\xi}$ for $|\boldsymbol{\xi}| = O(1)$.

The physical implications of the above results are that homogenisation and the corresponding quadratic approximation (1.4.3) underestimate passive scalar transport. The phenomenon is most dramatic in the dense limit but negligible in the dilute limit. This is illustrated in Figure 2.4 which focusses on two dense-limit cases: $a = \pi - 0.01$ and $\pi - 0.001$. It shows the (normalised) concentration $\theta(\boldsymbol{x}, t)$ in logarithmic scale along the diagonal $\boldsymbol{x} = |\boldsymbol{x}|(1,1)/\sqrt{2}$ obtained at five consecutive times multiple of $4\pi^2/\kappa_{\text{eff}}$. This choice ensures that the time is sufficiently long for the large-deviation approximation (2.2.1) to apply. The figure compares the concentration obtained from the large-deviation approximation with its Gaussian, diffusive approximation (1.4.3) obtained with effective diffusivity given by the Keller formula (1.3.11). Clearly the discrepancy between the large-deviation approximation and its Gaussian, diffusive approximation is largest at early times, in the tails of $\theta(\boldsymbol{x}, t)$ and for the largest of the two radii. As time increases, the Gaussian, diffusive approximation describes the bulk of the scalar concentration increasingly better.

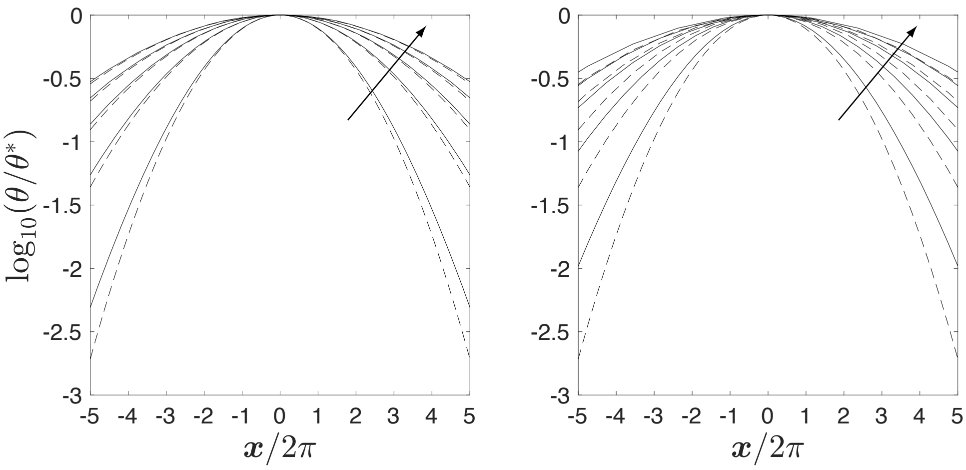

Figure 2.4: Normalised concentration $\theta(\boldsymbol{x},t)/\theta^*$ (in logarithmic scale) where $\theta^* = \max_{\boldsymbol{x}}\theta(\boldsymbol{x},t)$ plotted against $\boldsymbol{x}/(2\pi)$ for $\boldsymbol{x}$ in the direction $(1,1)$ at dimensionless times $\kappa_{\text{eff}}t/(4\pi^2) = 1$, 2, 3, 4 and 5, with the arrow pointing in the direction of increasing t, for obstacles of radius $a = \pi - 0.01$ (left) and $\pi - 0.001$ (right) (corresponding to gap half width $\varepsilon = 0.01$ and 0.001). Numerical results (solid lines) obtained by solving (2.2.6) are compared with the Gaussian approximation obtained from (1.3.6) with effective diffusivity κ_{eff} given by the Keller formula (1.3.11) (dashed lines).

2.5 Asymptotic analysis

In the remainder of the chapter we provide asymptotic approximations in of both the dilute and dense limits. For the dilute case we explain the validity of the quadratic approximation (1.4.3) with effective diffusivity κ_{eff} given by the Maxwell formula (1.3.10) throughout the range of $\boldsymbol{\xi}$. We achieve this by taking a as a small parameter in (2.2.9).

In the dense limit where the limitations of the diffusive approximation, non-Gaussianity and anisotropic behaviour are most prominent, we use the gap half width $\varepsilon = \pi - a \ll 1$ as small parameter.

2.6 Dilute limit

We now use matched asymptotics to obtain an approximation to the eigenvalue problem when $a \ll 1$ and $|\boldsymbol{p}| = O(1)$. The regular expansion of the eigenvalue $f(\boldsymbol{p})$,

$$f = f_0 + o(a) \tag{2.6.1}$$

is sought in parallel to the asymptotic expansion of the eigenvector $\psi(\boldsymbol{x})$ in the singularly perturbed domain ω. We construct two asymptotic expansions of $\psi(\boldsymbol{x})$ valid in different regions in ω. The first is written in terms of the unscaled variable $r = |\boldsymbol{x}| = O(1)$ and is called the outer (far-field) expansion it is subject to the boundary condition applied to the outer boundary of the elementary cell ω,

$$\nabla^2 \psi = f\psi, \qquad \boldsymbol{x} \in [-\pi, \pi)^2 \tag{2.6.2a}$$

$$\psi(\boldsymbol{x} + 2\pi \boldsymbol{e}_j) = e^{-2\pi \boldsymbol{p}\cdot\boldsymbol{e}_j}\psi(\boldsymbol{x}), \qquad \text{where} \quad j = 1, 2. \tag{2.6.2b}$$

The second is the inner (near-field) expansion subjected to the Neumann boundary condition and is written with the scaling $R = |\boldsymbol{X}| = r/a$,

$$\nabla_X^2 \Psi = a^2 f \Psi \tag{2.6.3a}$$

$$\boldsymbol{n} \cdot \nabla \Psi = \partial_R \Psi = 0, \qquad R = 1. \tag{2.6.3b}$$

The outer expansion approximates ψ in a domain excluding a small neighbourhood of the obstacle and thus captures the periodicity of the cell ω. Meanwhile, the inner expansion can be used to approximate ψ in a small neighbourhood of the circular obstacle, capturing the boundary layer phenomenon.

Leading-order solution

We begin by constructing an expansion of the **outer** problem valid outside the boundary layer. We assume a series expansion of the form,

$$\psi(\boldsymbol{x}) = \psi_0 + o(a) \tag{2.6.4}$$

The leading-order outer problem or the unperturbed problem, is

$$\nabla^2 \psi_0 = f_0 \psi_0, \qquad \boldsymbol{x} \in [-\pi, \pi)^2 \tag{2.6.5a}$$

$$\psi_0(\boldsymbol{x} + 2\pi \boldsymbol{e}_j) = e^{-2\pi \boldsymbol{p}\cdot\boldsymbol{e}_j} \psi_0(\boldsymbol{x}), \qquad \text{where} \quad j = 1, 2 \tag{2.6.5b}$$

which we obtain by inserting the ansatz (2.6.1) and (2.6.4) into problem (2.6.2). To solve the Helmholtz equation (2.6.5a) we assume a general solution of the form,

$$\psi_0 = a_0 e^{-\boldsymbol{p}\cdot\boldsymbol{x}} + b_0 e^{\boldsymbol{p}\cdot\boldsymbol{x}}, \tag{2.6.6}$$

were a_0 and b_0 are constants of integration. Applying the periodic boundary condition (2.6.5b) yields

$$\psi_0 = e^{-\boldsymbol{p}\cdot\boldsymbol{x}} \qquad \text{and} \quad f_0 = |\boldsymbol{p}|^2, \tag{2.6.7}$$

where without loss of generality we normalise ψ_0 by taking $a_0 = 1$.

The **inner** problem concerns the boundary region surrounding the circular obstacles. As a result we conveniently express variables in polar coordinates (r, φ). We suppose the thickness of region is $r = O(a)$ (which can be verified using the principal of dominant balance), and introduce the stretched coordinate $R = r/a = O(1)$. In order to understand the form of the series expansion in $\Psi(R, \varphi)$ we first match the inner and outer expansions using Van Dyke's matching rule [26, 31]. Writing the vectors $\boldsymbol{x} = r(\cos\varphi, \sin\varphi)$ and $\boldsymbol{p} = |\boldsymbol{p}|(\cos\alpha, \sin\alpha)$ in polar coordinates, through matching we obtain

$$\Psi(R, \varphi) = 1 - a|\boldsymbol{p}|R\cos(\varphi - \alpha) \quad \text{as } R \to \infty. \tag{2.6.8}$$

Guided by this we assume a series expansion,

$$\Psi(R, \varphi) = \Psi_0 + a\Psi_1 + o(a). \tag{2.6.9}$$

Substituting this into problem (2.6.3), yields the leading order inner problem

$$\nabla^2\Psi_0 = 0 \tag{2.6.10a}$$

$$\boldsymbol{n} \cdot \nabla\Psi_0 = \partial_R\Psi_0 = 0, \qquad R = 1. \tag{2.6.10b}$$

The general solution to the harmonic function Ψ_0 is written in polar coordinates as,

$$\Psi_0(R, \varphi) = a_{00} + c_0 \ln R + \sum_{n=1}^{\infty} a_{0n}R^n\cos(n\varphi) + b_{0n}R^n\sin(n\varphi) + c_{0n}R^{-n}\cos(n\varphi) + d_{0n}R^{-n}\sin(n\varphi) \tag{2.6.11}$$

and imposing Neumann condition (2.6.10b) applied at the interface $R = 1$ we obtain

$$\partial_R\Psi_0\big|_{R=1} = c_0 + \sum_{n=1}^{\infty} n(a_{0n} - c_{0n})\cos(n\varphi) + n(b_{0n} - d_{0n})\sin(n\varphi) = 0. \tag{2.6.12}$$

For non-trivial solutions we set: $c_0 = 0$, $a_{0n} = c_{0n}$ and $b_{0n} = d_{0n}$. Then the harmonic solution to the inner problem is uniquely determined as,

$$\Psi_0 = a_{00} + \sum_{n=1}^{\infty} a_{0n}(R^n + \frac{1}{R^n})\cos(n\varphi) + b_{0n}(R^n + \frac{1}{R^n})\sin(n\varphi). \tag{2.6.13}$$

Matching with the outer problem we obtain that: $a_{0n} = b_{0n} = 0 \, \forall \, n \geqslant 1$ and $a_{00} = 1$. The solution to the leading order inner problem simplifies to

$$\Psi_0 = 1. \tag{2.6.14}$$

The inner problem at $O(a)$ is,

$$\nabla^2 \Psi_1 = 0 \tag{2.6.15a}$$

$$\boldsymbol{n} \cdot \nabla \Psi_1 = \partial_R \Psi_0 = 0, \qquad R = 1, \tag{2.6.15b}$$

which we note is of the same form as the inner problem at $O(1)$. The solution to (2.6.15) is, given by

$$\Psi_1 = a_{10} + \sum_{n=1}^{\infty} a_{1n}(R^n + \frac{1}{R^n}) \cos{(n\varphi)} + b_{1n}(R^n + \frac{1}{R^n}) \sin{(n\varphi)}. \tag{2.6.16}$$

Matching with the outer problem we obtain that $a_{10} = 0$, $a_{1n} = b_{1n} = 0 \, \forall \, n \geqslant 2$, $b_{11} = -|\boldsymbol{p}| \sin \alpha$, $a_{11} = -|\boldsymbol{p}| \cos \alpha$. Thus,

$$\Psi_1 = -|\boldsymbol{p}|(R + \frac{1}{R}) \cos{(\varphi - \alpha)}. \tag{2.6.17}$$

The term in R^{-1} is crucial: through matching it carries the effect of the obstacle into the outer region, at $O(a^2)$.

The leading-order inner and outer solutions may be used to obtain a higher-order correction to the eigenvalue $f(\boldsymbol{p})$. We multiply (2.2.9) by $e^{\boldsymbol{p} \cdot \boldsymbol{x}}$ and integrate over the elementary cell ω: consisting of a square $[-\pi, \pi)^2$ minus the obstacle with radius $a \ll 1$ centred at the origin

$$\int_{\omega} e^{\boldsymbol{p} \cdot \boldsymbol{x}} \nabla^2 \psi \, d\boldsymbol{x} = \int_{\omega} f e^{\boldsymbol{p} \cdot \boldsymbol{x}} \psi \, d\boldsymbol{x}, \tag{2.6.18}$$

Then integrating by parts twice (2.6.18) becomes

$$\int_{\partial\omega} e^{\boldsymbol{p}\cdot\boldsymbol{x}}\boldsymbol{n}\cdot\nabla\psi\, dl - \int_{\partial\omega} e^{\boldsymbol{p}\cdot\boldsymbol{x}}\boldsymbol{n}\cdot\boldsymbol{p}\psi\, dl = (f-|\boldsymbol{p}|^2)\int_{\omega} e^{\boldsymbol{p}\cdot\boldsymbol{x}}\psi\, d\boldsymbol{x}. \tag{2.6.19}$$

We use the 'tilted' periodicity condition (2.2.10) to deduce that $\exp(\boldsymbol{p}\cdot\boldsymbol{x})\psi$ and $\exp(\boldsymbol{p}\cdot\boldsymbol{x})\nabla\psi$ are periodic and therefore contributions along opposing edges of the square boundary cancel. We demonstrate this by focusing on the contributions obtained on opposing edges $x=-\pi$ and $x=\pi$. On these edges the second integral becomes

$$\int_{-\pi}^{\pi} e^{-\pi q_1}e^{yq_2}q_1\psi\big|_{x=-\pi}\, dy - \int_{-\pi}^{\pi} e^{\pi q_1}e^{yq_2}q_1\psi\big|_{x=\pi}\, dy = 0, \tag{2.6.20}$$

since $\psi_1\big|_{x=-\pi} = e^{-2\pi q_1}\psi_1\big|_{x=\pi}$. Similarly the first integral gives contributions of the form,

$$\int_{-\pi}^{\pi} e^{-\pi q_1}e^{yq_2}\partial_x\psi\big|_{x=-\pi}\, dy - \int_{-\pi}^{\pi} e^{\pi q_1}e^{yq_2}\partial_x\psi\big|_{x=\pi}\, dy = 0, \tag{2.6.21}$$

since $\partial_x\psi_1\big|_{x=\pi} = e^{-2\pi}q_1\partial_x\psi_1\big|_{x=-\pi}$. After applying the boundary condition (2.2.9b), Equation (2.6.19) becomes

$$(f-|\boldsymbol{p}|^2)\int_{\omega} e^{\boldsymbol{p}\cdot\boldsymbol{x}}\psi\, d\boldsymbol{x} = -\int_{\mathcal{B}} e^{\boldsymbol{p}\cdot\boldsymbol{x}}\boldsymbol{n}\cdot\boldsymbol{p}\psi\, dl. \tag{2.6.22}$$

We use $\psi \sim \psi_0 = \mathrm{e}^{-\boldsymbol{p}\cdot\boldsymbol{x}}$ to approximate the left-hand side of (2.6.22) and

$$\psi|_{r=a} = \Psi|_{R=1} \sim \Psi_0(1,\varphi;a) + a\Psi_1(1,\varphi;a) = 1 - 2a|\boldsymbol{p}|\cos(\varphi-\alpha) + o(a), \tag{2.6.23}$$

and

$$\mathrm{e}^{\boldsymbol{p}\cdot\boldsymbol{x}} = 1 + a|\boldsymbol{p}|\cos(\varphi-\alpha) + o(a) \tag{2.6.24}$$

to approximate the right-hand side of (2.6.22). Carrying out the integrations gives

$$4\pi^2(f-|\boldsymbol{p}|^2) = a\int_0^{2\pi}(1-a|\boldsymbol{p}|\cos(\varphi-\alpha))|\boldsymbol{p}|\cos(\varphi-\alpha)\, d\varphi = -a^2\pi|\boldsymbol{p}|^2. \tag{2.6.25}$$

We finally obtain an approximation for $f(\boldsymbol{p})$ given by

$$f(\boldsymbol{p}) \sim \left(1 - \frac{a^2}{4\pi}\right)|\boldsymbol{p}|^2 \quad \text{as } a \to 0. \tag{2.6.26}$$

Alternatively, in terms of the solid area fraction the approximation is given by

$$f(\boldsymbol{p}) \sim (1-\sigma)|\boldsymbol{p}|^2 \quad \text{as } \sigma \to 0. \tag{2.6.27}$$

Taking the Legendre transform (2.6.27) we obtain that the rate function $g(\boldsymbol{\xi})$ is approximated by

$$g(\boldsymbol{\xi}) \sim \frac{|\boldsymbol{\xi}|^2}{4\,(1-\sigma)} \quad \text{as } \sigma \to 0. \tag{2.6.28}$$

Thus, to leading order, the large-deviation approximation reproduces the results of classical homogenisation. In other words, the tails as well as the core of the distribution are Gaussian.

We finally note that the quadratic approximations (2.6.27) and (2.6.28) hold in the dilute limit for obstacles of arbitrary shapes, because on the far-field, dipolar form of the inner solution matters at leading order.

2.7 Dense limit

2.7.1 Discrete-network approximation

An intuitive way to understand the dense limit is to consider a discrete network model as a simplified analogue to the continuum model (2.1.1). The building block of this model is Keller's asymptotic solution leading to (1.3.11) [46]. This relies on the observation that

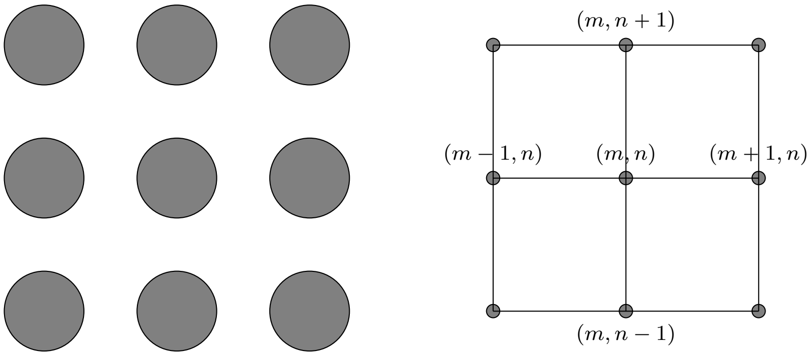

Figure 2.5: Models of diffusion in square lattice of circular obstacles: (left) continuum model and (right) discrete network model.

the scalar concentration $\theta(\boldsymbol{x}, t)$ is nearly constant away from the small gaps separating neighbouring obstacles and changes rapidly along the gaps. The scalar flux is then localised in the gaps, unidirectional and approximately uniform in the direction transverse to the gaps. For a gap in the x-direction, for example, the total scalar flux is given by

$$F = 2h_\varepsilon(x)\frac{\partial \theta}{\partial x}, \tag{2.7.1}$$

where $h_\varepsilon(x)$ denotes the gap half width. For ε small, $h_\varepsilon(x)$ can be approximated as a parabola centred in the middle of the gap: $h_\varepsilon(x) \approx x^2/(2\pi) + \varepsilon$. Dividing across by $2h_\varepsilon(x)$ and integrating in the region enclosed by the gap gives

$$\Delta\theta = F\int_{-(\pi-\varepsilon)}^{\pi-\varepsilon} \frac{\pi}{x^2 + 2\pi\varepsilon}\, dx = F\sqrt{\frac{\pi}{2\varepsilon}}\tan^{-1}(x/\sqrt{2\pi\varepsilon})\Big|_{-(\pi-\varepsilon)}^{\pi-\varepsilon}, \tag{2.7.2}$$

where Δ is not to be confused with the Laplacian. The integral converges so we can extend the integration range to $x \in (-\infty, \infty)$ [46]. Taking a Taylor expansion of the $\tan^{-1}$ term as $|x| \to \infty$ in (2.7.2) we obtain at leading order

$$\Delta\theta = F\sqrt{\frac{\pi}{2\varepsilon}}\tan^{-1}(x/\sqrt{2\pi\varepsilon})\Big|_{-\infty}^{\infty} \sim F\sqrt{\frac{\pi}{2\varepsilon}}\pi. \tag{2.7.3}$$

Rearranging (2.7.3) we obtain the relationship

$$F = \alpha \Delta\theta, \quad \text{where} \ \ \alpha = \sqrt{2\varepsilon/\pi^3}, \tag{2.7.4}$$

between the total scalar flux and the difference $\Delta\theta$ in concentration between the two sides of the gap. This makes it possible to approximate (2.1.1) by a discrete network in which regions away from the gaps are represented as vertices and the gaps between them as edges (see the right panel of Figure 2.5). The (near-uniform) concentration $\theta^{(m,n)}$ inside the region centred at $\pi(2m+1, 2n-1)$ then evolves in response to the sum of the fluxes in (the four) adjacent gaps, leading to

$$\mathscr{A}\frac{d\theta^{(m,n)}}{dt} = \alpha(\theta^{(m+1,n)} + \theta^{(m,n+1)} + \theta^{(m-1,n)} + \theta^{(m,n-1)} - 4\theta^{(m,n)}), \tag{2.7.5}$$

where $\mathscr{A} = \pi^2(4-\pi)$ is the approximate area of the region. A rigorous justification of model (2.7.5) can be obtained using the techniques in [18].

It is easy to determine the long-time behaviour of (2.7.5). The diffusion approximation is recovered by taking the continuum limit of (2.7.5), approximating the right-hand side by $4\pi^2\alpha\nabla^2\theta$ to obtain the effective diffusivity

$$\kappa_{\text{eff}} = 4\pi^2\alpha/\mathscr{A} = \alpha/(1-\pi/4) \tag{2.7.6}$$

which is readily shown to match Keller's expression (1.3.11) using that $\sigma = \pi/4 - \varepsilon/2 + O(\varepsilon^2)$. However, the diffusive approximation is limited. Further information can be obtained from the rate function which appears in the large-deviation approximation $\theta^{(m,n)} \sim t^{-1}\exp\Big(-tg_{\text{d}}(\boldsymbol{r}^{(m,n)}/t)\Big)$ of solutions of the network model (2.7.5). Substituting into (2.7.5) gives

$$\mathscr{A} f_{\text{d}}(\boldsymbol{p}) = \alpha(e^{-2\pi p} + e^{-2\pi q} + e^{2\pi p} + e^{-2\pi q} - 4) \tag{2.7.7}$$

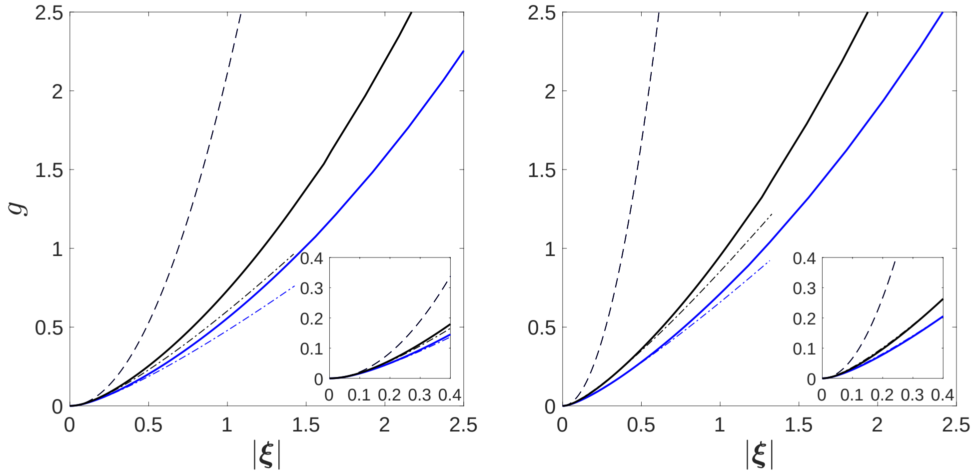

Figure 2.6: Rate function g plotted against $|\boldsymbol{\xi}|$ for obstacles of radius (left) $a = \pi - 0.01$ and (right) $\pi - 0.001$ (corresponding to gap half width $\varepsilon = 0.01$ and 0.001) in the directions $(1,1)$ (black) and $(1,0)$ (blue). Numerical results (thick solid lines) obtained by solving (2.2.6) are compared with the quadratic (Gaussian) approximation (1.4.3) (dashed lines) with effective diffusivity κ_{eff} given by the Keller formula (1.3.11) and the discrete-network approximation (2.7.9) (dashed-dotted). The insets focus on small values of $|\boldsymbol{\xi}|$.

and simplifying this we obtain an explicit relation for the Legendre transform $f_{\mathrm{d}}(\boldsymbol{p})$ of $g_{\mathrm{d}}(\boldsymbol{\xi})$, namely

$$f_{\mathrm{d}}(\boldsymbol{p}) = \frac{4\alpha}{\mathscr{A}} \left(\sinh^2(\pi p) + \sinh^2(\pi q) \right). \tag{2.7.8}$$

Taking the Legendre transform of (2.7.8) then yields

$$g_{\mathrm{d}}(\boldsymbol{\xi}) = \frac{2\alpha}{\mathscr{A}} \left(\mathrm{S}(\beta\xi) + \mathrm{S}(\beta\eta) \right), \tag{2.7.9}$$

where $\mathrm{S}(x) = 1 + x\sinh^{-1}(x) - \sqrt{1+x^2}$ and $\beta = \mathscr{A}/(4\pi\alpha)$. Figure 2.6 shows that the rate function (2.7.9) is an improvement to the quadratic (Gaussian) approximation. Nevertheless this improvement is limited to small values of $|\boldsymbol{\xi}|$. This is because a key assumption of the network model, namely that the concentration is nearly uniform outside the gaps, breaks down for $|\boldsymbol{x}|$ large enough that $|\boldsymbol{\xi}|$ is not small. We now carry out an asymptotic analysis that yields an approximation to rate function that is valid for $|\boldsymbol{\xi}| = O(1)$ and recovers (2.7.9) as a limiting case.

2.7.2 Asymptotics

We apply matched asymptotics to obtain an approximation to the solution of the eigenvalue problem (2.2.9) for $\varepsilon \ll 1$ that is valid in the distinguished regime $|\boldsymbol{p}| = O(1)$. The analysis is conveniently carried out in the translated elementary cell ω' shown in Figure 2.1. This is centred on the star-like region which we will (inaccurately) refer to as 'astroid' in the limit $\varepsilon \to 0$, when the gaps close to form four cusps (see Figure 2.8).

We first consider the solution inside a representative gap, in the the positive x-direction, that for convenience we refer to as west of the centre of ω'. The gap boundaries are given by

$$y = -\pi \pm h_\varepsilon(x), \quad \text{where} \quad h_\varepsilon(x) = \pi - \left((\pi-\varepsilon)^2 - x^2\right)^{1/2}, \quad 0 \leqslant x \leqslant \pi - \varepsilon. \tag{2.7.10}$$

This form suggests an *outer region* where x, $y + \pi = O(1)$ in which case (2.7.10) may be approximated as the boundary of the astroid,

$$y = -\pi \pm h_0(x) + O(\varepsilon) \quad \text{where} \quad h_0(x) = \pi - \sqrt{\pi^2 - x^2}, \quad 0 \leqslant x \leqslant \pi, \tag{2.7.11}$$

and an *inner region* where $X = x/\sqrt{\varepsilon} = O(1)$ and $Y = (y+\pi)/\varepsilon = O(1)$ in terms of which (2.7.10) is approximately given by

$$Y = \pm H_\varepsilon(X) = \pm H_0(X) + O(\varepsilon) \quad \text{where} \quad H_0(X) = \frac{X^2}{2\pi} + 1, \quad 0 \leqslant X < \infty, \tag{2.7.12}$$

Inner region

Inside the inner region, the modified Helmholtz problem (2.2.9) becomes

$$\varepsilon\partial_{XX}\Psi + \partial_{YY}\Psi = \varepsilon^2 f\Psi, \tag{2.7.13a}$$

for the eigenfunction $\Psi(X,Y) = \psi(x,y)$, with the Neumann boundary condition approximated by

$$\pm\,\partial_Y\Psi - \varepsilon\left(\frac{X}{\pi}\partial_X\Psi \pm \frac{X^2}{2\pi^2}\partial_Y\Psi\right) + O(\varepsilon^{3/2}) = 0 \quad \text{at} \ \ Y = \pm H_0(X) + O(\varepsilon). \tag{2.7.13b}$$

We now introduce the expansions

$$\Psi(X,Y) = \Psi_0(X,Y) + \varepsilon^{1/2}\Psi_1(X,Y) + \varepsilon\Psi_2(X,Y) + O(\varepsilon^{3/2}) \tag{2.7.14a}$$

and

$$f(\boldsymbol{p}) = f_0(\boldsymbol{p}) + \varepsilon^{1/2} f_1(\boldsymbol{p}) + \varepsilon f_2(\boldsymbol{p}) + O(\varepsilon^{3/2}) \tag{2.7.14b}$$

of the eigenvalue and eigenfunction into (2.7.13) to obtain, at $O(1)$ and $O(\varepsilon^{1/2})$,

$$\partial_{YY}\Psi_i = 0 \quad \text{with} \ \ \partial_Y\Psi_i = 0 \quad \text{at} \ \ Y = \pm H_0(X) \quad (i = 0,1) \tag{2.7.15}$$

and thus $\Psi_0 = \Psi_0(X)$ and $\Psi_1 = \Psi_1(X)$ i.e., they are transversely uniform. The key equation appears at $O(\varepsilon)$. Using the Y-independence of Ψ_0 it simplifies to

$$\partial_{YY}\Psi_2 = -\partial_{XX}\Psi_0 \quad \text{with} \quad \mp\,\partial_Y\Psi_2 = \frac{1}{\pi}X\partial_X\Psi_0 \quad \text{at} \ \ Y = \pm H_0(X). \tag{2.7.16}$$

Integrating (2.7.16) for $Y \in [-H_0(X), H_0(X)]$ we find that $\partial_X(H_0(X)\partial_X\Psi_0) = 0$, hence

$$\Psi_0 = A_1\int_0^X \frac{\mathrm{d}X'}{H_0(X')} + B_1 = \sqrt{2\pi}A_1\tan^{-1}\left(\frac{X}{\sqrt{2\pi}}\right) + B_1, \quad X = x/\varepsilon^{1/2}, \tag{2.7.17a}$$

for constants A_1 and B_1 to be determined by matching with the outer solution. Similarly, using symmetry, the solution inside the gaps to the south (in the negative y-direction), east (in the negative x-direction), and north (in the positive y-direction) of the centre of ω', are

$$\Psi_0 = A_2\sqrt{2\pi}\tan^{-1}\left(\frac{Y}{\sqrt{2\pi}}\right) + B_2, \quad Y = (y + 2\pi)/\varepsilon^{1/2}, \tag{2.7.17b}$$

$$\Psi_0 = A_3\sqrt{2\pi}\tan^{-1}\left(\frac{X}{\sqrt{2\pi}}\right) + B_3, \quad X = (x - 2\pi)/\varepsilon^{1/2}, \tag{2.7.17c}$$

$$\Psi_0 = A_4\sqrt{2\pi}\tan^{-1}\left(\frac{Y}{\sqrt{2\pi}}\right) + B_4, \quad Y = y/\varepsilon^{1/2}, \tag{2.7.17d}$$

introducing additional constants A_i and B_i for $i = 2, 3, 4$. The constants are constrained by the 'tilted' periodicity condition (2.2.9), giving

$$(A_3, B_3) = \mathrm{e}^{-2\pi p}(A_1, B_1) \quad \text{and} \quad (A_4, B_4) = \mathrm{e}^{-2\pi q}(A_2, B_2). \tag{2.7.18}$$

Outer region and matching

In the outer region we assume the expansion

$$\psi = \psi_0 + \varepsilon^{1/2}\psi_1 + \varepsilon\psi_2 + O(\varepsilon^{3/2}). \tag{2.7.19}$$

To leading-order ψ_0 satisfies

$$\nabla^2\psi_0 = f_0\psi_0, \quad \boldsymbol{n}\cdot\nabla\psi_0 = 0 \quad \text{on} \quad y = -\pi \pm \begin{cases} h_0(x) & \text{for} \;\; 0 \leqslant x < \pi \\ h_0(2\pi - x) & \text{for} \;\; \pi \leqslant x < 2\pi \end{cases}. \tag{2.7.20a}$$

Additional boundary conditions are obtained by matching the solution near the cusps of the astroid with the inner solutions (2.7.17). Near the cusp to the west of the centre, ψ_0 satisfies the approximation $\partial_x(h_0(x)\partial_x\psi_0) = 0$ to (2.7.20a) (obtained following similar steps as in §2.7.2), hence

$$x^2\partial_x\psi_0 \sim C_1, \quad \text{as } \boldsymbol{x} \to \boldsymbol{x}_1 = (0, -\pi), \tag{2.7.20b}$$

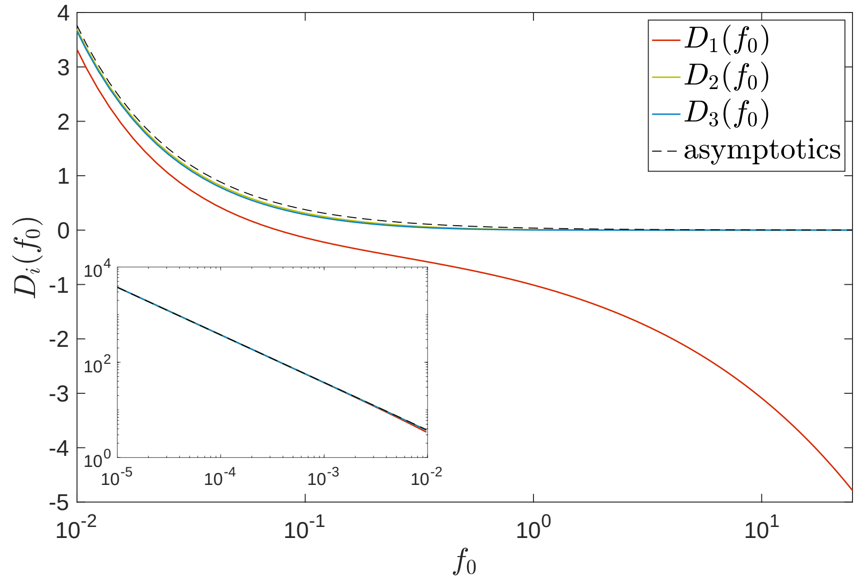

Figure 2.7: Functions D_i ($i = 1, 2, 3$) defined by (2.7.23) against f_0. The numerical estimates (solid lines) are compared with the asymptotic approximation (2.7.28) for $f_0 \ll 1$ (dashed line).

where C_1 is a constant to be determined. The behaviour is similar near the other three cusps located at $\boldsymbol{x}_2 = (\pi, -2\pi)$, $\boldsymbol{x}_3 = (2\pi, -\pi)$ and $\boldsymbol{x}_4 = (\pi, 0)$ involving constants C_i for $i = 2, 3, 4$.

Canonical boundary-value problem. Exploiting the four-fold symmetry the solution to (2.7.20) can be written as the linear combination

$$\psi_0(x,y) = C_1\psi^*(x,y) + C_2\psi^*(y+2\pi,-x) + C_3\psi^*(2\pi-x,-y-2\pi) + C_4\psi^*(-y,x) \quad (2.7.21)$$

of the solution ψ^* of the canonical boundary-value problem

$$\nabla^2\psi^* = f_0\psi^*, \quad \text{on} \quad y = -\pi \pm \begin{cases} h_0(x) & \text{for } 0 \leqslant x < \pi \\ h_0(2\pi - x) & \text{for } \pi \leqslant x < 2\pi \end{cases}, \quad (2.7.22a)$$

with Neumann boundary conditions on the astroid except on the western cusp where

$$x^2 \partial_x \psi^* \to 1 \quad \text{as } \boldsymbol{x} \to \boldsymbol{x}_1. \tag{2.7.22b}$$

The key point is that solving (2.7.22) determines four functions $D_i(f_0)$, $(i = 1, \ldots, 4)$ defined by

$$\psi^* \sim -\frac{1}{x} - D_1(f_0) \;\text{ as }\; \boldsymbol{x} \to \boldsymbol{x}_1 \quad \text{and} \quad \psi^* \sim -D_i(f_0) \;\text{ as }\; \boldsymbol{x} \to \boldsymbol{x}_i \;\text{ for }\; i = 2,\, 3,\, 4. \tag{2.7.23}$$

Thus, these functions describe the leading-order behaviour of ψ^* once the singular contribution $-1/x$ at $\boldsymbol{x}_1$ is subtracted out. By symmetry

$$D_4(f_0) = D_2(f_0). \tag{2.7.24}$$

We obtain the functions $D_i(f_0)$ by solving (2.7.22) numerically for a range of values of f_0 using a standard finite-element discretisation. The difficulty associated with the singular shape of the astroid is avoided by trimming off the cusp regions with four straight segments placed a small distance δ away from each cusp. Figure 2.7 shows the results obtained for a range of values of f_0. These results have been checked to be insensitive to the value of δ as well as to the resolution of the finite-element discretisation ($\delta = 0.01$ for the figure). Figure 2.8 shows the form of ψ^* for different values of f_0. Clearly, larger values of f_0, corresponding to larger values of $\boldsymbol{p}$, lead to higher contrasts in ψ_0, reflecting the fact that the asymptotic analysis goes beyond the hypothesis of near-uniform concentration assumed for the discrete-network approximation of §2.7.1.

The asymptotic behaviour of $D_i(f_0)$ for small f_0 is useful for later reference. In

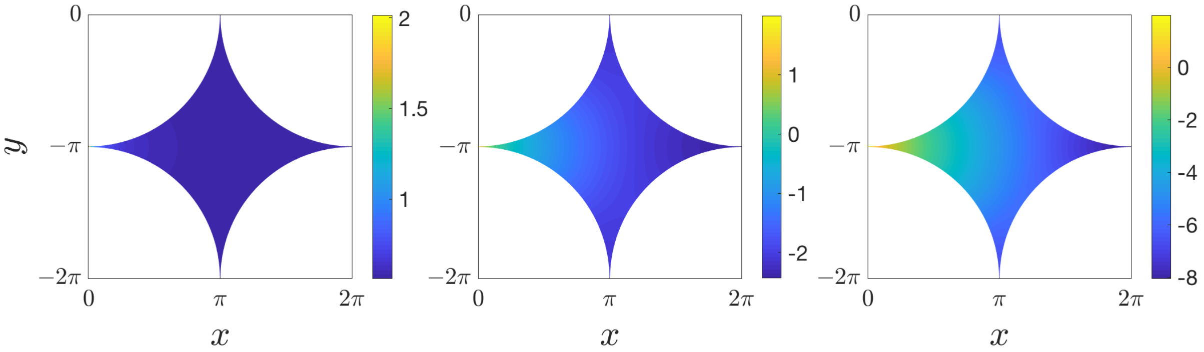

Figure 2.8: Logarithm $\log_{10}|\psi^*|$ of $\psi^*(\boldsymbol{x})$ defined as the solution to the canonical boundary-value problem (2.7.22) obtained for (left) $f_0 = 0.01$, (middle) 1 and (right) 10.

this limit, the solution ψ^* may be expanded according to

$$\psi^* = f_0^{-1}\psi_0^* + \psi_1^* + O(f_0), \quad f_0 \ll 1. \tag{2.7.25}$$

Substituting (2.7.25) into (2.7.22a), we obtain that

$$\nabla^2\psi_0^* = 0 \quad \text{and} \quad \nabla^2\psi_1^* = \psi_0^*, \quad \text{on} \quad y = -\pi \pm \begin{cases} h_0(x) & \text{for } \ 0 \leqslant x < \pi \\ h_0(2\pi - x) & \text{for } \ \pi \leqslant x < 2\pi \end{cases}. \tag{2.7.26a}$$

Additionally, from (2.7.22b) we have that ψ_0^* and ψ_1^* satisfy Neumann boundary conditions on the astroid except on the western cusp where ψ_1^* satisfies

$$x^2\partial_x\psi_1^* \to 1 \quad \text{as } \boldsymbol{x} \to \boldsymbol{x}_1. \tag{2.7.26b}$$

Thus, $\psi_0^* = c$ where c is a constant. The value of c may be determined by integrating the second equation in (2.7.26a) and using (2.7.26b) to obtain

$$\mathscr{A}c = \int_{\omega'} \nabla^2\psi_1^* \mathrm{d}\boldsymbol{x} \sim -\lim_{\delta\to 0}\int_{-\delta^2/(2\pi)}^{\delta^2/(2\pi)} \partial_x\psi_1^*|_{x=\delta}\, \mathrm{d}y = -\frac{1}{\pi}, \tag{2.7.27}$$

with the area $\mathscr{A}$ defined in (2.7.5). Therefore

$$D_i(f_0) \sim \frac{1}{\pi \mathscr{A} f_0} \quad \text{for} \quad f_0 \ll 1 \quad (i = 1, \cdots, 4). \tag{2.7.28}$$

Figure 2.7 confirms the validity of (2.7.28).

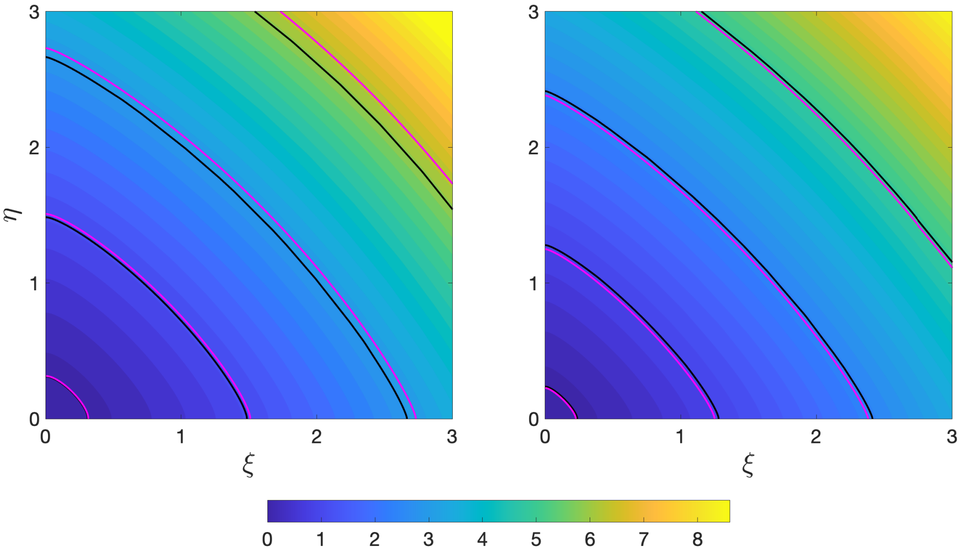

Figure 2.9: Rate function g plotted against $|\boldsymbol{\xi}|$ for square lattice of circular obstacles with radius $a = \pi - 0.01$ (left) and $\pi - 0.001$ (right) (corresponding to gap half widths $\varepsilon = 0.01$ and 0.001) obtained by solving the eigenvalue problem (2.2.6). Selected contours (with values 0.1, 1, 2.5 and 5) compare the numerical g (black) with the asymptotic approximation deduced from (2.7.30) (pink).

Matching. The leading-order approximation to the eigenvalue $f(\boldsymbol{p})$ is obtained by matching the solution in the inner and outer regions. Comparing (2.7.17) with (2.7.21) using (2.7.23) and (2.7.24) leads to

$$C_1 = -2\pi\sqrt{\varepsilon}A_1, \qquad -C_1D_1(f_0) - (C_2 + C_4)D_2(f_0) - C_3D_3(f_0) = \sqrt{\pi^3/2}A_1 + B_1, \tag{2.7.29a}$$

$$C_2 = -2\pi\sqrt{\varepsilon}A_2, \qquad -(C_1 + C_3)D_2(f_0) - C_2D_1(f_0) - C_3D_4(f_0) = \sqrt{\pi^3/2}A_2 + B_2, \tag{2.7.29b}$$

$$C_3 = 2\pi\sqrt{\varepsilon}A_3, \qquad -C_1D_3(f_0) - (C_2 + C_4)D_2(f_0) - C_3D_1(f_0) = -\sqrt{\pi^3/2}A_3 + B_3, \tag{2.7.29c}$$

$$C_4 = 2\pi\sqrt{\varepsilon}A_4, \qquad -(C_1 + C_3)D_2(f_0) - C_2D_3(f_0) - C_4D_1(f_0) = -\sqrt{\pi^3/2}A_4 + B_4. \tag{2.7.29d}$$

We now use (2.7.18) to reduce (2.7.29) to a homogeneous linear system for two of the constants, e.g., A_1 and A_2. Non-trivial solutions exist provided that the determinant of the associated matrix vanish. After some manipulations using (2.7.24) this gives

$$\begin{aligned}\big(D_3(f)\cosh(2\pi p) - D_1(f) - (2\pi\alpha)^{-1}\big)\,\big(D_3(f)\cosh(2\pi q) - D_1(f) - (2\pi\alpha)^{-1}\big)& \\ - D_2^2(f)\,\big(\cosh(2\pi p) - 1\big)\,\big(\cosh(2\pi q) - 1\big) &= 0\end{aligned} \tag{2.7.30}$$

with $\alpha = \sqrt{2\varepsilon/\pi^3}$ as defined in (2.7.4) and we omit the subscript of f_0.

Equation (2.7.30) is the central result of this paper. It is a transcendental equation for the Legendre transform f of the rate function g as a function of the gap half width ε. Once the functions $D_i(f)$ have been tabulated, it reduces the determination f and hence g to an algebraic problem. The transcendental dependence of f on ε reflects the uniform validity of our approximation across a range of values of $\boldsymbol{p}$, including in particular a regime where $\sqrt{\varepsilon}\mathrm{e}^{2\pi|\boldsymbol{p}|} = O(1)$ as well as the discrete-network regime of §2.7.1.

We solve (2.7.30) numerically for a range of $\boldsymbol{p} = (p, q)$ to obtain $f(\boldsymbol{p})$ and $g(\boldsymbol{\xi})$ by Legendre transform. In practice, it is convenient to express $\boldsymbol{p} = |\boldsymbol{p}|(\cos\varphi, \sin\varphi)$ in polar form and, for fixed angle φ, solve for $|\boldsymbol{p}|$ as a function of f using a nonlinear solver such as Matlab's `fzero`. The computation needs a good first guess which we obtain by noting that, when $\varphi = 0$, i.e. for $\boldsymbol{p} = |\boldsymbol{p}|(1, 0)$, (2.7.30) reduces to $|\boldsymbol{p}| = 1/(2\pi)\cosh^{-1}((D_1(f) + \alpha^{-1})/D_3(f))$. We then iterate over increasing values of φ using the value of $|\boldsymbol{p}|$ determined previously as an initial guess for the next solution.

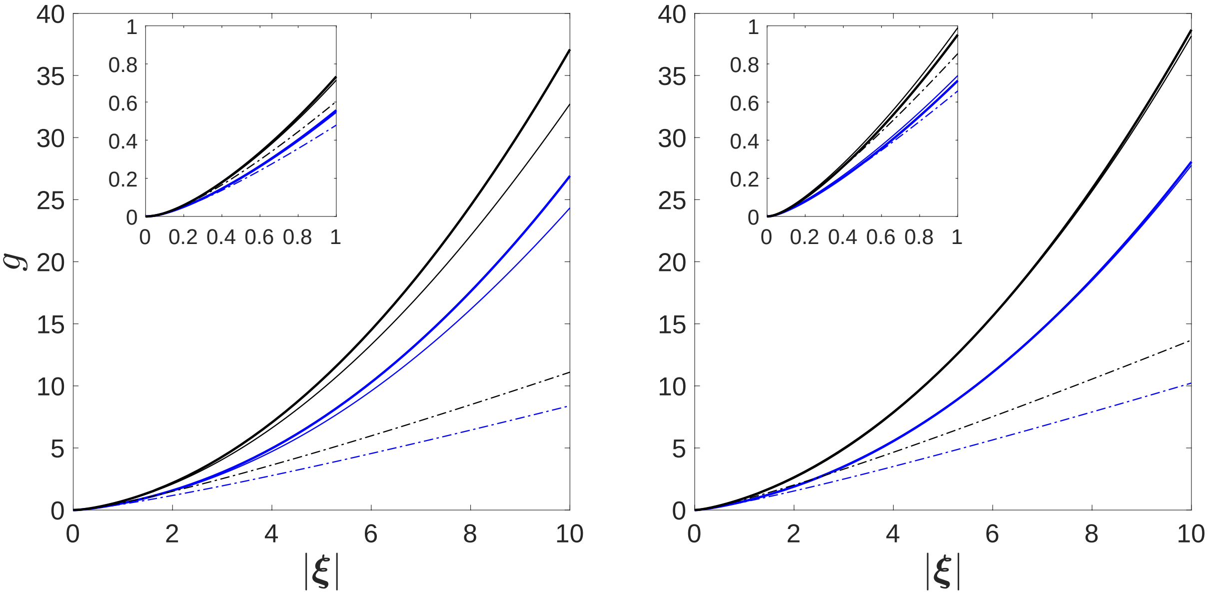

Figure 2.10: Cross-section of the rate function g in Figure 2.9 in the directions $(1, 1)$ (black lines) and $(1, 0)$ (lines). Numerical results obtained by solving (2.2.6) (thick solid lines) are compared against the asymptotic approximation derived from (2.7.30) (thin solid lines) and from the discrete-network approximation (2.7.8) (dashed-dotted). The insets focus on small values of $|\boldsymbol{\xi}|$.

Figure 2.9 compares the asymptotic prediction for $g(\boldsymbol{\xi})$ deduced from (2.7.30) to that obtained by finite-element solution of the full eigenvalue problem (2.2.6) for $\varepsilon = 0.01$

and 0.001. The agreement is excellent throughout the range of $|\boldsymbol{\xi}|$, showing that our approximation captures the scalar concentration deep into the tails. This is more clearly demonstrated in Figure 2.10 which displays cross-sections of $g(\boldsymbol{\xi})$ for $\boldsymbol{\xi}$ along the ξ-axis and along the diagonal $\xi = \eta$ and for a very wide range of values of $|\boldsymbol{\xi}|$. While some discrepancies between asymptotic and numerical solutions are visible for $\varepsilon = 0.01$ the solutions match perfectly for $\varepsilon = 0.001$.

For very large $|\boldsymbol{\xi}|$, the concentrations are exceedingly small, of course. It is nonetheless interesting to note that $g(\boldsymbol{\xi})$ is then controlled by an action-minimising trajectory as predicted by the Friedlin–Wentzell (small-noise) large-deviation theory [37]. This gives the asymptotics $g(\boldsymbol{\xi}) \sim d^2(\boldsymbol{\xi})/4$ and hence $\theta \propto \mathrm{e}^{-d^2(\boldsymbol{x}-\boldsymbol{x}_0)/(4t)}$ where $d(\boldsymbol{x}) = \pi(x+y)/4 + (1-\pi/4)|x-y|$ is the distance along the shortest path (made up of quarter circles and a line segment (horizontal if $x > y$, vertical if $x < y$) joining $\boldsymbol{x}_0$ to $\boldsymbol{x}$ while avoiding the obstacles. Thus, at very large distances, one recovers a diffusive behaviour with the molecular value of the diffusivity but a non-Euclidean distance determined by the obstacle geometry (see [87] for a similar phenomenon in a different geometry).

We conclude by checking explicitly that our asymptotic analysis recovers the discrete-network approximation (2.7.8). This approximation arises from the transcendental equation (2.7.30) in the limit of small f: introducing the small-f asymptotic approximation (2.7.28) of the D_i into (2.7.30) gives

$$\begin{aligned}\big(\cosh(2\pi p) - 1 - \mathscr{A} f/(2\alpha)\big)\,\big(\cosh(2\pi q) - 1 - \mathscr{A} f/(2\alpha)\big)& \\ - \big(\cosh(2\pi p) - 1\big)\,\big(\cosh(2\pi q) - 1\big) &= 0, \qquad (2.7.31)\end{aligned}$$

which simplies as $f = f_\mathrm{d}$ with the network expression (2.7.8) of f_d. The corresponding rate function g_d is compared with the asymptotic and numerical estimates of g in Figure 2.10 which demonstrates the superiority of our asymptotic result over the network approximation.

2.8 Concluding remarks

This chapter revisits the classical results of Maxwell, Rayleigh, Keller and many others on the impact of an array of obstacles on the diffusion of scalars in an otherwise homogeneous medium. Homogenisation theory predicts that, at a coarse-grained level, a scalar released instantaneously simply diffuses with a (computable) effective diffusivity. A basic observation is that this conclusion is restricted to the bulk of the scalar distribution and that the more general tool of large-deviation theory is necessary to capture the tails of the distribution. Focusing on the case of a square lattice of circular obstacles for simplicity, we show that the non-diffusive behaviour is leading to tail concentrations that are much fatter than predicted by the effective diffusion approximation. This effect is strongest in the dense limit, when the obstacles are nearly touching and large-scale dispersion is strongly inhibited. We examine this limit using a matched-asymptotics approach which reduces the computation of the large-deviation rate function – requiring in general the solution of a family of elliptic eigenvalue problems – to the algebraic equation (2.7.30). The rate function that is obtained in this way captures the scalar concentration over a wide range of distances from the point of release and encompasses several physical regimes: the diffusive regime with Keller's effective diffusivity [46], a closely related regime associated with a lattice random walk, all the way to the extreme-tail regime where the scalar concentration is controlled by single shortest-distance paths.

Chapter Three

Dispersion in Networks

3.1 Introduction

In this chapter, we consider the evolution of a passive scalar inside networks composed of an infinite number of vertices connected by (one-dimensional) edges of equal length ℓ. We focus on three types of networks: triangular (with vertex degree 6), square (with vertex degree 4) and hexagonal (with vertex degree 3) networks, illustrated in Figure 3.1. The networks are generated by periodic lattices. These are Bravais lattices for the case of triangular and square networks but not for the hexagonal network. The position of the vertices are obtained from linear combinations of the vectors $\ell \boldsymbol{a}_1$ and $\ell \boldsymbol{a}_2$ (see Equation (1.2.3)) which span the elementary cell. In triangular and square networks, the elementary cell $\boldsymbol{n} = (n_1, n_2) \in \mathbb{Z}^2$ consists of a single vertex (see the left and middle panels of Figure 3.1) whose position is given by Equation (1.2.1), repeated here

$$\boldsymbol{r}^{(\boldsymbol{n})} = \ell(n_1 \boldsymbol{a}_1 + n_2 \boldsymbol{a}_2), \tag{3.1.1}$$

so that $\boldsymbol{r}^{(0)} = \mathbf{0}$. For triangular networks the (lattice) basis vectors are

$$\boldsymbol{a}_1 = \frac{1}{2}(1, \sqrt{3})^T \quad \text{and} \quad \boldsymbol{a}_2 = \frac{1}{2}(1, -\sqrt{3})^T, \tag{3.1.2a}$$

while for square networks the (lattice) basis vectors are

$$\boldsymbol{a}_1 = (1, 0)^T \quad \text{and} \quad \boldsymbol{a}_2 = (0, 1)^T. \tag{3.1.2b}$$

In contrast, in hexagonal networks, the elementary cell consists of two vertices (see the right panel of Figure 3.1). Their positions are given by (3.1.1) and $\boldsymbol{r}^{(n)} - (1, 0)^T$ where this time

$$\boldsymbol{a}_1 = \frac{\sqrt{3}}{2}(\sqrt{3}, 1)^T \quad \text{and} \quad \boldsymbol{a}_2 = \frac{\sqrt{3}}{2}(\sqrt{3}, -1)^T. \tag{3.1.2c}$$

The position on the network may be generated from the corresponding lattice via

$$\boldsymbol{x}_i^{(n)} = \ell_i \boldsymbol{b}_i + \boldsymbol{r}^{(n)}, \tag{3.1.3}$$

where $\boldsymbol{b}_i$ for $i = 1, \ldots, N$ is a unit vector that denotes the direction of the ith edge with N the total number of edges inside an elementary cell. For square networks, $N = 2$ while for triangular and hexagonal networks, $N = 3$ (see Figure 3.1). The distance along the ith edge is measured from $\boldsymbol{r}^{(n)}$ by $\ell_i \in [0, \ell)$. For all networks,

$$\boldsymbol{b}_i = \boldsymbol{a}_i, \quad i = 1, 2, \tag{3.1.4a}$$

where $\boldsymbol{a}_i$ are obtained from (3.1.2a) for the triangular and hexagonal network and (3.1.2b) for the square network. We also have

$$\boldsymbol{b}_3 = (1, 0)^T \quad \text{and} \quad \boldsymbol{b}_3 = -(1, 0)^T, \tag{3.1.4b}$$

for the triangular and hexagonal networks, respectively.

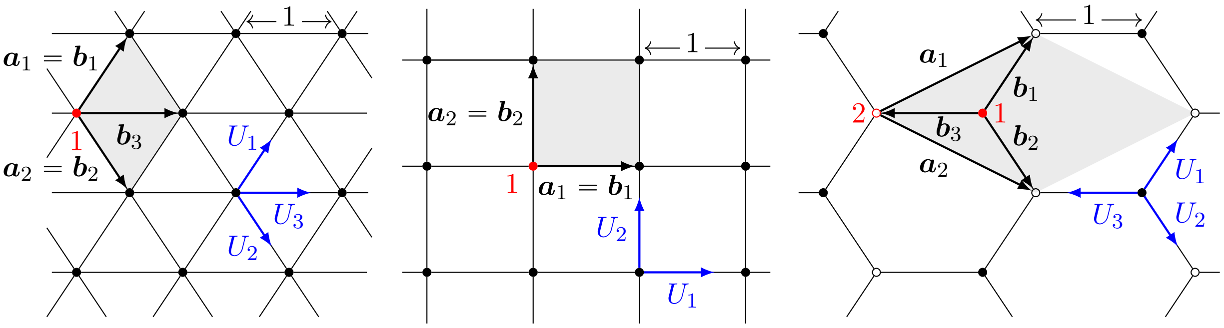

Figure 3.1: Triangular (left), square (middle) and hexagonal (right) networks and their associated elementary cell (shaded grey area). These are spanned by vectors $\boldsymbol{a}_1$ and $\boldsymbol{a}_2$ while the unit vectors $\boldsymbol{b}_1$, $\boldsymbol{b}_2$ and $\boldsymbol{b}_3$ describe the direction of the network edges connecting the vertices (black and white dots). Fluid flows with velocity $U_i = \boldsymbol{b}_i \cdot \boldsymbol{U}$ for $i = 1, \dots, N$ along edges of unit length.

Taking ℓ as reference length and and ℓ^2/κ as reference time with κ being the diffusivity constant, the (one-dimensional) advection–diffusion equation for the scalar concentration θ is given by

$$\partial_t \theta_i^{(\boldsymbol{n})} + U_i \partial_{\ell_i} \theta_i^{(\boldsymbol{n})} = \partial^2_{\ell_i \ell_i} \theta_i^{(\boldsymbol{n})}, \tag{3.1.5}$$

for $\ell_i \in [0, 1)$, where $\theta_i^{(\boldsymbol{n})}(\ell_i, t) := \theta(\boldsymbol{x}_i^{(\boldsymbol{n})}, t)$ denotes the concentration along the ith edge in elementary cell $\boldsymbol{n}$. Here, the parameters $U_i := \boldsymbol{b}_i \cdot \boldsymbol{U}\ell/\kappa$ are the projection of the uniform velocity field $\boldsymbol{U} = (U_x, U_y)$ along the ith edge. They correspond to (local) Péclet numbers measuring the strength of advection relative to diffusion. For the triangular and hexagonal network we have additionally that $U_3 = U_1 + U_2 = U_x$ and $U_3 = -(U_1 + U_2) = -U_x$, respectively.

Complementing (3.1.5) are boundary conditions applied at the vertices. These are obtained by assuming continuity of the concentration and a zero net concentration flux at each vertex. For the *triangular and square networks*, the boundary conditions are given by

$$\theta_i^{(\boldsymbol{n})}\big|_{\ell_i=0} = \theta_j^{(\boldsymbol{n}-\boldsymbol{e}_j)}\big|_{\ell_j=1}, \tag{3.1.6a}$$

for $i, j = 1 \dots N$ and

$$\sum_{i=1}^{N} \partial_{\ell_i}\theta_i^{(\boldsymbol{n})}\big|_{\ell_i=0} - \partial_{\ell_i}\theta_i^{(\boldsymbol{n}-\boldsymbol{e}_i)}\big|_{\ell_i=1} = 0. \tag{3.1.6b}$$

Here, the vectors $\boldsymbol{e}_1 = (1,0)^T$, $\boldsymbol{e}_2 = (0,1)^T$ and $\boldsymbol{e}_3 = (1,1)^T$ are used to define elementary cells adjacent to $\boldsymbol{n}$. For the *hexagonal network*, the corresponding boundary conditions are given by

$$\theta_i^{(\boldsymbol{n})}\big|_{\ell_i=0} = \theta_j^{(\boldsymbol{n})}\big|_{\ell_j=0}, \quad \text{and} \quad \theta_i^{(\boldsymbol{n}-\boldsymbol{e}_i)}\big|_{\ell_i=1} = \theta_j^{(\boldsymbol{n}-\boldsymbol{e}_j)}\big|_{\ell_j=1}, \tag{3.1.7a}$$

for $i, j = 1 \dots N$ and

$$\sum_{i=1}^{N} \partial_{\ell_i}\theta_i^{(\boldsymbol{n})}\big|_{\ell_i=0} = \sum_{i=1}^{N} \partial_{\ell_i}\theta_i^{(\boldsymbol{n}-\boldsymbol{e}_i)}\big|_{\ell_i=1} = 0, \tag{3.1.7b}$$

where this time $\boldsymbol{e}_1 = (1,0)^T$, $\boldsymbol{e}_2 = (0,1)^T$ and $\boldsymbol{e}_3 = (0,0)^T$.

Given an initial condition, the scalar concentration is completely determined by the system of equations (3.1.5) together with boundary condition (3.1.6) or (3.1.7) (depending on the type of network). It can be solved numerically using finite differences or Laplace transforms [28, 51, 42] or Monte Carlo simulations [87].

We are once more interested in the initial value problem corresponding to the instantaneous release of the scalar at some location inside the network which without loss of generality we take to be the origin so that $\theta_i^{(\boldsymbol{n})}(\ell_i, 0) = \delta(\ell_i)\delta(\boldsymbol{n})$. Once again we assume that the solution decays at infinity. Our aim is to obtain a coarse-grained description of the concentration at large times, in the large-deviation regime. We achieve this by extending the approach in [87] for dispersion in square and rectangular networks to tackle more general two-dimensional periodic networks based on both Bravais and non-Bravais lattices. The approach, which is introduced in §3.2, provides the rate function g in terms of the solution to a set of transcendental equations which are easy to solve numerically. Their quadratic approximation, which we obtain in §3.3, determines the effective diffusive approximation for the concentration with the effective diffusivity tensor, K explicitly obtained and analysed in the limits of small and large Péclet. At large distances from the centre of mass, the behaviour of the concentration, described §3.3 can greatly differ from the effective diffusive approximation. Throughout the chapter the focus is to determine how dispersion depends on the the geometry (associated with the orientation and length of the edges) and topology (associated with the connectivity of the network vertices) of the networks considered. We conclude the chapter in §3.5.

3.2 Large deviations

We use the theory of large-deviations [37, 36, 86] now applied to periodic networks to approximate the concentration at long times $t \gg 1$ by the two-scale form (1.4.1) [40, 87, 35], repeated here for convenience

$$\theta(\boldsymbol{x}_i^{(\boldsymbol{n})}, t) = \phi(\boldsymbol{x}_i^{(\boldsymbol{n})}, \boldsymbol{\xi}, t) e^{-tg(\boldsymbol{\xi})}, \quad \text{where } \boldsymbol{\xi} = \frac{\boldsymbol{x}}{t} \in \mathbb{R}^2. \tag{3.2.1}$$

Once more the rate function g is a continuous function of $\boldsymbol{\xi}$ describing the most rapid changes in θ. It is non-negative, convex and has a single minimum and zero located at

$\boldsymbol{\xi} = \boldsymbol{\xi}^*$, where $\boldsymbol{\xi}^*$ corresponds to the centre of mass of θ. Higher order corrections are captured by ϕ . This is supported on the network so that ϕ is only non-zero at $\boldsymbol{x}_i^{(\boldsymbol{n})}$ where $\boldsymbol{x}_i^{(\boldsymbol{n})}$ is given by (3.1.3). We assume that ϕ inherits the same periodicity of the network so that

$$\phi(\boldsymbol{x}_i^{(\boldsymbol{n})} + \boldsymbol{r}^{(\boldsymbol{n})}, \boldsymbol{\xi}, t) = \phi(\boldsymbol{x}_i^{(\boldsymbol{n})}, \boldsymbol{\xi}, t), \tag{3.2.2}$$

where $\boldsymbol{x}_i^{(\boldsymbol{n})}$ is given by (3.1.3).

Following the same steps as in Chapter 2, we expand $\phi(\boldsymbol{x}_i^{(\boldsymbol{n})}, \boldsymbol{\xi}, t)$ according to

$$\phi(\boldsymbol{x}_i^{(\boldsymbol{n})}, \boldsymbol{\xi}, t) = t^{-1}\left(\phi_0(\boldsymbol{x}_i^{(\boldsymbol{n})}, \boldsymbol{\xi}) + t^{-1}\phi_1(\boldsymbol{x}_i^{(\boldsymbol{n})}, \boldsymbol{\xi}) + t^{-2}\phi_2(\boldsymbol{x}_i^{(\boldsymbol{n})}, \boldsymbol{\xi}) + \dots\right). \tag{3.2.3}$$

Changing variables using (3.1.3), and letting $\phi_i^{(\boldsymbol{n})} := \phi_0(\boldsymbol{x}_i^{(\boldsymbol{n})}, \boldsymbol{\xi})$ we arrive, at leading order at

$$\partial^2_{\ell_i\ell_i}\phi_i^{(\boldsymbol{n})} - (U_i + 2\boldsymbol{b}_i \cdot \boldsymbol{p})\partial_{\ell_i}\phi_i^{(\boldsymbol{n})} + (U_i\boldsymbol{b}_i \cdot \boldsymbol{p} + (\boldsymbol{b}_i \cdot \boldsymbol{p})^2)\phi_i^{(\boldsymbol{n})} = f(\boldsymbol{p})\phi_i^{(\boldsymbol{n})}, \tag{3.2.4}$$

for $i = 1 \dots N$, where we have defined

$$\boldsymbol{p} = (p_x, p_y)^T = \nabla_{\boldsymbol{\xi}} g \quad \text{and} \quad f(\boldsymbol{p}) = \boldsymbol{\xi} \cdot \boldsymbol{p} - g(\boldsymbol{\xi}). \tag{3.2.5}$$

Note for convenience we have changed notation from $\boldsymbol{p} = (p, q)$ (used in previous chapters) to $\boldsymbol{p} = (p_x, p_y)$.

Equation (3.2.4) is supplemented by boundary condition applied at each vertex. For the *triangular and square networks*, these are inferred from (3.1.6) from where we obtain that

$$\phi_i^{(\boldsymbol{n})}\big|_{\ell_i=0} = \phi_j^{(\boldsymbol{n}-\boldsymbol{e}_j)}\big|_{\ell_j=1}, \tag{3.2.6a}$$

$$\sum_{i=1}^{N} \partial_{\ell_i}\phi_i^{(\boldsymbol{n})}\big|_{\ell_i=0} - \partial_{\ell_i}\phi_i^{(\boldsymbol{n}-\boldsymbol{e}_i)}\big|_{\ell_i=1} = 0, \tag{3.2.6b}$$

for $i, j = 1 \dots N$. For the *hexagonal network*, the boundary conditions are inferred from (3.1.7) from where we obtain that

$$\phi_i^{(\boldsymbol{n})}\big|_{\ell_i=0} = \phi_j^{(\boldsymbol{n})}\big|_{\ell_j=0} \quad \text{and} \quad \phi_i^{(\boldsymbol{n}-\boldsymbol{e}_i)}\big|_{\ell_i=1} = \phi_j^{(\boldsymbol{n}-\boldsymbol{e}_j)}\big|_{\ell_j=1}, \tag{3.2.7a}$$

$$\sum_{i=1}^{N} \partial_{\ell_i}\phi_i^{(\boldsymbol{n})}\big|_{\ell_i=0} = \sum_{i=1}^{N} \partial_{\ell_i}\phi_i^{(\boldsymbol{n}-\boldsymbol{e}_i)}\big|_{\ell_i=1} = 0, \tag{3.2.7b}$$

for $i, j = 1 \dots N$. Equation (3.2.4) together with the boundary condition (3.2.6) or (3.2.7) as well as the periodicity condition (3.2.2) define a family of eigenvalue problems which determine a discrete spectrum of eigenvalues $f(\boldsymbol{p})$. We once more focus on the principal eigenvalue $f(\boldsymbol{p})$ which is unique real and isolated with a sign-definite associated eigenfunction $\{\phi_i^{(\boldsymbol{n})}\}_{i=1}^{N}$ [52]. Moreover, f is a convex function of $\boldsymbol{p}$. Together with (3.2.5) this implies that $f(\boldsymbol{p})$ and $g(\boldsymbol{\xi})$ are Legendre duals.

The solution to the eigenvalue problem (3.2.4) together with boundary condition (3.2.6) or (3.2.7) is a transcendental equation in $f(\boldsymbol{p})$. We next solve the eigenvalue problems.

3.2.1 Triangular and square networks

We first focus on the case of triangular and square networks. We use the first boundary condition (3.2.6a) to deduce that the value of $\phi_i^{(\boldsymbol{n})}$ at all the vertices is the same. Let A be the value of $\phi_i^{(\boldsymbol{n})}$ at $\ell_i = 0, 1$ for $i = 1 \dots N$. We use (3.2.4) to obtain an explicit expression for $\phi_i^{(\boldsymbol{n})}$

$$\phi_i^{(\boldsymbol{n})} = \frac{Ae^{\mu_i \ell_i}}{\sinh \nu_i}\big(\sinh \nu_i(1-\ell_i) + e^{-\mu_i}\sinh \nu_i \ell_i\big), \tag{3.2.8}$$

for $i = 1 \dots N$ where the variables μ_i and λ_i are defined as

$$\mu_i = \boldsymbol{b}_i \cdot \boldsymbol{p} + \frac{U_i}{2}, \quad \nu_i = \sqrt{\frac{U_i^2}{4} + f(\boldsymbol{p})}. \tag{3.2.9}$$

Substituting (3.2.8) inside the second boundary condition (3.2.6b) yields

$$\sum_{i=1}^{N} \frac{\nu_i}{\sinh \nu_i} \left(\cosh \mu_i - \cosh \nu_i\right) = 0. \tag{3.2.10}$$

Equation (3.2.10) is a transcendental equation whose solution determines f as a function of $\boldsymbol{p}$.

3.2.2 Hexagonal networks

We follow a similar procedure for the hexagonal network. Using the first boundary condition (3.2.7a) we let $\phi_i^{(\boldsymbol{n})}\big|_{\ell_i=0} = A$ and $\phi_i^{(\boldsymbol{n})}\big|_{\ell_i=1} = B$ for $i = 1 \dots 3$. Then, solving (3.2.4) yields

$$\phi_i^{(\boldsymbol{n})} = \frac{e^{\mu_i \ell_i}}{\sinh \nu_i}\big(A \sinh \nu_i (1-\ell_i) + B e^{-\mu_i} \sinh \nu_i \ell_i\big), \tag{3.2.11}$$

for $i = 1 \dots 3$ with μ_i and ν_i defined in (3.2.9). Substituting (3.2.11) inside the second boundary condition (3.2.7b) and using $\sum_{i=1}^{N} \mu_i = 0$ yields a linear system of equations, expressed in matrix form as

$$\mathrm{T}\boldsymbol{a} = \boldsymbol{0}, \tag{3.2.12a}$$

where

$$\mathrm{T} = \sum_{i=1}^{3} \begin{bmatrix} -\nu_i \coth \nu_i & \nu_i e^{-\mu_i} \operatorname{csch} \nu_i \\ -\nu_i e^{\mu_i} \operatorname{csch} \nu_i & \nu_i \coth \nu_i \end{bmatrix}, \quad \boldsymbol{a} = \begin{bmatrix} A \\ B \end{bmatrix}. \tag{3.2.12b}$$

For a non-trivial solution of (3.2.12), the matrix must be singular i.e. $|\mathrm{T}| = 0$. This leads to the transcendental equation

$$\sum_{i,j=1}^{3} \frac{\nu_i \nu_j}{\sinh \nu_i \sinh \nu_j} (e^{-\mu_i} e^{\mu_j} - \cosh \nu_i \cosh \nu_j) = 0. \tag{3.2.13}$$

The transcendental equations (3.2.10) and (3.2.13) for $f(\boldsymbol{p})$ are the main results of this chapter. Their solution provides f as a function of $\boldsymbol{p}$ which can be used to determine the rate function g as a function of $\boldsymbol{\xi}$. It is then easy to show that $f(\mathbf{0}) = 0$. For $\boldsymbol{p} \neq \mathbf{0}$ the number of solutions are infinite. We focus on the unique real solution corresponding to the principal eigenvalue.

The principal eigenvalue cannot be analytically obtained except in the absence of a flow when $U_x = U_y = 0$. In this case, the principal eigenvalue is given by

$$f(\boldsymbol{p}) = \left(\cosh^{-1} \left(\frac{1}{N} \sum_{i=1}^{N} \cosh(\boldsymbol{b}_i \cdot \boldsymbol{p}) \right) \right)^2, \tag{3.2.14a}$$

for the triangular and square networks. While for the hexagonal networks, the corresponding expression is

$$f(\boldsymbol{p}) = \left(\cosh^{-1} \left(\frac{1}{3} \sqrt{\sum_{i,j=1}^{3} e^{(\boldsymbol{b}_j - \boldsymbol{b}_i) \cdot \boldsymbol{p}}} \right) \right)^2. \tag{3.2.14b}$$

However, an explicit expression for their Legendre transform cannot be calculated. For arbitrary U_x, U_y, the principal eigenvalue can be obtained numerically using MATLAB's *fsolve*, then using finite differences to carry out a numerical Legendre transform to deduce g. We now proceed to analyse the behaviour of f and g in the homogenisation regime, when the diffusive (Gaussian) approximation holds.

3.3 Effective diffusivity

The diffusive (Gaussian) approximation can be recovered from the large-deviation approximation (3.2.1) by determining the quadratic approximation of g around its minimum, $\boldsymbol{\xi}^*$:

$$g(\boldsymbol{\xi}) \sim \frac{1}{4}(\boldsymbol{\xi} - \boldsymbol{\xi}^*)^T \mathrm{K}^{-1}(\boldsymbol{\xi} - \boldsymbol{\xi}^*), \quad |\boldsymbol{\xi} - \boldsymbol{\xi}^*| \ll 1. \tag{3.3.1}$$

Upon substitution of (3.3.1) inside (3.2.1), the large deviation approximation reduces to the diffusive (Gaussian) approximation

$$\theta(\boldsymbol{x}, t) \sim e^{-(\boldsymbol{x}-\boldsymbol{\xi}^* t)^T \mathrm{K}^{-1}(\boldsymbol{x}-\boldsymbol{\xi}^* t)/(4t)}, \quad t \gg 1, \tag{3.3.2}$$

where $\mathrm{K} = 2(\nabla_{\boldsymbol{\xi}}\nabla_{\boldsymbol{\xi}} g(\boldsymbol{\xi}^*))^{-1}$ corresponds to the effective diffusivity tensor (see §1.4.1). To achieve this we first expand f in power series of $\boldsymbol{p}$ around $\boldsymbol{p} = \boldsymbol{0}$. This is because from the Legendre transform $\boldsymbol{p} = \nabla_{\boldsymbol{\xi}} g(\boldsymbol{\xi}^*) = \boldsymbol{0}$ corresponds to the minimum of g, hence

$$\boldsymbol{\xi}^* = \nabla_{\boldsymbol{p}} f(\boldsymbol{0}). \tag{3.3.3}$$

At the same time, taking the gradient of $\boldsymbol{p} = \nabla_{\boldsymbol{\xi}} g$ with respect to $\boldsymbol{\xi}$ at $\boldsymbol{\xi}^*$ gives $\nabla_{\boldsymbol{\xi}}\nabla_{\boldsymbol{\xi}} g(\boldsymbol{\xi}^*) = \nabla_{\boldsymbol{\xi}} \boldsymbol{p}(\boldsymbol{\xi}^*)$. Taking the gradient of $\boldsymbol{\xi} = \nabla_{\boldsymbol{p}} f$ with respect to $\boldsymbol{\xi}$ gives $I = \nabla_{\boldsymbol{p}}\nabla_{\boldsymbol{p}} f \cdot \nabla_{\boldsymbol{\xi}} \boldsymbol{p}$ where I is the identity matrix. Evaluating at $\boldsymbol{\xi} = \boldsymbol{\xi}^*$ and $\boldsymbol{p} = \boldsymbol{0}$ yields the standard relation for the effective diffusivity tensor in terms of the Hessian of f [87]:

$$\mathrm{K} = \frac{1}{2}\nabla_{\boldsymbol{p}}\nabla_{\boldsymbol{p}} f(\boldsymbol{0}). \tag{3.3.4}$$

Explicit expressions for $\boldsymbol{\xi}^*$ and K are obtained by introducing the expansion

$$f = \boldsymbol{\xi}^* \cdot \boldsymbol{p} + \boldsymbol{p}^T \mathrm{K} \boldsymbol{p} + O(|\boldsymbol{p}|^3), \tag{3.3.5}$$

(recalling that $f(\mathbf{0}) = 0$) inside (3.2.10) and (3.2.13) and expanding in power series of $\boldsymbol{p}$. We use Mathematica, a symbolic algebra package, to solve at $O(|\boldsymbol{p}|)$ from where we obtain $\boldsymbol{\xi}^*$ and at $O(|\boldsymbol{p}|^2)$ from where we obtain K.

We can alternatively determine $\boldsymbol{\xi}^*$ and K by seeking a perturbative solution of the eigenvalue problems (3.2.4) together with the boundary condition (3.2.6) or (3.2.7), in the limit $|\boldsymbol{p}| \to 0$. This approach recovers, at leading order, the cell problem of homogenisation. However, the corresponding calculation, are significantly more involved, particularly for the hexagonal case (see §3.3.1). Thus, the large-deviation approximation not only provides the rate function but also an easier calculation of $\boldsymbol{\xi}^*$ and K.

For all three networks, we obtain that

$$\boldsymbol{\xi}^* = \frac{1}{N}\sum_{i=1}^{N} U_i \boldsymbol{b}_i = \frac{1}{2}(U_x, U_y). \tag{3.3.6}$$

In the case of *triangular and square networks*, the components of K satisfy

$$\mathrm{K}_{11} = \frac{1}{2N}\sum_{i=1}^{N}\frac{1}{U_i}\left(4\xi_x^*\boldsymbol{b}_i\cdot\boldsymbol{e}_1 + (\xi_x^* - U_i\boldsymbol{b}_i\cdot\boldsymbol{e}_1)^2\coth\frac{U_i}{2} - 2\frac{\xi_x^{*2}}{U_i}\right), \tag{3.3.7a}$$

$$\mathrm{K}_{12} = \frac{1}{2N}\sum_{i=1}^{N}\frac{1}{U_i}\left(2\boldsymbol{b}_i\cdot(\xi_y^*\boldsymbol{e}_1 + \xi_x^*\boldsymbol{e}_2) + (\xi_x^* - U_i\boldsymbol{b}_i\cdot\boldsymbol{e}_1)(\xi_y^* - U_i\boldsymbol{b}_i\cdot\boldsymbol{e}_2)\coth\frac{U_i}{2} - 2\frac{\xi_x^*\xi_y^*}{U_i}\right), \tag{3.3.7b}$$

where $\mathrm{K}_{21} = \mathrm{K}_{12}$ and K_{22} is obtained from K_{11} by taking $\boldsymbol{e}_1 \mapsto \boldsymbol{e}_2$ and $\xi_x^* \mapsto \xi_y^*$. Expression (3.3.7) generalises the expression for the effective diffusivity tensor obtained for square networks in [87].

For *hexagonal networks* the corresponding calculation become cumbersome. We instead work with the matrix equation (3.2.12). We expand T according to

$$\mathrm{T} = \mathrm{T}^{(0)} + \sum_{j=1}^{2} \mathrm{T}_j^{(1)} p_{l_j} + \sum_{j,k=1}^{2} \mathrm{T}_{jk}^{(2)} p_{l_j} p_{l_k} + O(|\boldsymbol{p}|^3), \quad \text{as } |\boldsymbol{p}| \to 0, \tag{3.3.8}$$

where the labels (l_1, l_2) correspond to (x, y) and the matrices $\mathrm{T}^{(0)}$, $\mathrm{T}_j^{(1)}$ and $\mathrm{T}_{jk}^{(2)}$ for $j, k = 1, 2$ are independent of $\boldsymbol{p}$ and tracefree (since T is tracefree although not necessarily symmetric). In order to calculate K we need to determine the determinant of T. This can be expressed as a power series in $|\boldsymbol{p}|$ given by

$$\begin{aligned}|\mathrm{T}| = |\mathrm{T}^{(0)}| + \sum_{j=1}^{2}(\mathrm{Tr}(\mathrm{T}^{(0)})\mathrm{Tr}(\mathrm{T}_j^{(1)}) - \mathrm{Tr}(\mathrm{T}^{(0)}\mathrm{T}_j^{(1)}))p_{l_j} + \sum_{j=1}^{2}(|\mathrm{T}_j^{(1)}| + \mathrm{Tr}(\mathrm{T}^{(0)})\mathrm{Tr}(\mathrm{T}_{jj}^{(2)})\\ - \mathrm{Tr}(\mathrm{T}^{(0)}\mathrm{T}_{jj}^{(2)}))p_{l_j}^2 + (\mathrm{Tr}(\mathrm{T}_1^{(1)})\mathrm{Tr}(\mathrm{T}_2^{(1)}) - \mathrm{Tr}(\mathrm{T}_1^{(1)}\mathrm{T}_2^{(1)}) + \mathrm{Tr}(\mathrm{T}^{(0)})\mathrm{Tr}(\mathrm{T}_{12}^{(2)}) - \mathrm{Tr}(\mathrm{T}^{(0)}\mathrm{T}_{12}^{(2)}))p_{l_1}p_{l_2}.\end{aligned} \tag{3.3.9}$$

Equation (3.3.9) significantly simplifies using the tracefree property of the matrices together with equation (3.3.6):

$$|\mathrm{T}| = \boldsymbol{p}^T M \boldsymbol{p}, \tag{3.3.10a}$$

where

$$M = \begin{bmatrix} \left|\mathrm{T}_1^{(1)}\right| - \mathrm{Tr}(\mathrm{T}^{(0)}\mathrm{T}_{11}^{(2)}) & -\frac{1}{2}(\mathrm{Tr}(\mathrm{T}_1^{(1)}\mathrm{T}_2^{(1)}) - \mathrm{Tr}(\mathrm{T}^{(0)}\mathrm{T}_{12}^{(2)})) \\ -\frac{1}{2}(\mathrm{Tr}(\mathrm{T}_1^{(1)}\mathrm{T}_2^{(1)}) - \mathrm{Tr}(\mathrm{T}^{(0)}\mathrm{T}_{12}^{(2)})) & \left|\mathrm{T}_2^{(1)}\right| - \mathrm{Tr}(\mathrm{T}^{(0)}\mathrm{T}_{22}^{(2)}) \end{bmatrix}. \tag{3.3.10b}$$

We now determine $\mathrm{T}^{(0)}$, $\mathrm{T}_j^{(1)}$ and $\mathrm{T}_{jk}^{(2)}$ for $j, k = 1, 2$. With the aid of Mathematica, we find that

$$\mathrm{T}^{(0)} = \frac{1}{2}\left(\sum_{i=1}^{3} U_i \coth\frac{U_i}{2}\right)\begin{bmatrix} -1 & 1 \\ -1 & 1 \end{bmatrix}, \tag{3.3.11}$$

and

$$\mathrm{T}_j^{(1)} = \frac{1}{2}\sum_{i=1}^{3} {U_i}^{-1} \begin{bmatrix} \xi_{l_j}^* \, a(U_i) & c_-(U_i)(b(U_i)\xi_{l_j}^* - U_i^2 \boldsymbol{b}_i \cdot \boldsymbol{e}_j) \\ c_+(U_i)\left(b(U_i)\xi_{l_j}^* + U_i^2 \boldsymbol{b}_i \cdot \boldsymbol{e}_j\right) & -\xi_{l_j}^* \, a(U_i) \end{bmatrix}, \quad (3.3.12)$$

for $j = 1, 2$. The components of $\mathrm{T}_{jk}^{(2)}$ are:

$$(\mathrm{T}_{jk}^{(2)})_{11} = \frac{1}{2}\sum_{i=1}^{3} d(U_i)\mathrm{K}_{jk} + e(U_i)\xi_{l_j}^*\xi_{l_k}^* + \mathrm{K}_{11}\delta_{1k}, \quad (3.3.13a)$$

$$(\mathrm{T}_{jk}^{(2)})_{12} = \frac{1}{2}\sum_{i=1}^{3} c_-(U_i)\left(\frac{U_i(\boldsymbol{b}_i \cdot \boldsymbol{e}_j)(\boldsymbol{b}_i \cdot \boldsymbol{e}_k)}{2} + \frac{b(U_i)}{U_i}\left(\mathrm{K}_{jk} - \frac{\boldsymbol{b}_i \cdot (\boldsymbol{e}_j\xi_{l_k}^* + \boldsymbol{e}_k\xi_{l_j}^*)}{2}\right) + f(U_i)\xi_{l_j}^*\xi_{l_k}^*\right), \quad (3.3.13b)$$

$$(\mathrm{T}_{jk}^{(2)})_{21} = \frac{1}{2}\sum_{i=1}^{3} c_+(U_i)\left(\frac{U_i(\boldsymbol{b}_i \cdot \boldsymbol{e}_j)(\boldsymbol{b}_i \cdot \boldsymbol{e}_k)}{2} + \frac{b(U_i)}{U_i}\left(\mathrm{K}_{jk} + \frac{\boldsymbol{b}_i \cdot (\boldsymbol{e}_j\xi_{l_k}^* + \boldsymbol{e}_k\xi_{l_j}^*)}{2}\right) + f(U_i)\xi_{l_j}^*\xi_{l_k}^*\right), \quad (3.3.13c)$$

for $j, k = 1, 2$ where $(\mathrm{T}_{jk}^{(2)})_{22} = -(\mathrm{T}_{jk}^{(2)})_{11}$ and δ_{jk} is the Kronecker delta function. Here, we have defined the functions

$$a(x) = x\coth^2(x/2) - 2\coth\bigl(x/2\bigr) - x, \qquad b(x) = 2 - x\coth\bigl(x/2\bigr),$$

$$c_\pm(x) = \mp e^{\pm x/2}\,\mathrm{csch}\bigl(x/2\bigr), \qquad d(x) = (1 - x^{-1}\sinh x)\,\mathrm{csch}^2(x/2),$$

$$e(x) = (\sinh x + x - x^2\coth x/2)x^{-3}\,\mathrm{csch}^2(x/2),$$

$$f(x) = \Bigl(-2 - x\coth\bigl(x/2\bigr) - x^2(1/2 - \coth^2(x/2))\Bigr)\,x^{-3}.$$

We now determine K. This is achieved by using (3.3.10) to solve for $|\mathrm{T}| = 0$ to obtain

$$\mathrm{K} = \mathrm{K}^{(h)} + \frac{1}{3}\left(\sum_{i=1}^{3} U_i \coth\frac{U_i}{2}\right)^{-1} \begin{bmatrix} 2\left|T_1^{(1)}\right| & -\mathrm{Tr}(T_1^{(1)}T_2^{(1)}) \\ -\mathrm{Tr}(T_1^{(1)}T_2^{(1)}) & 2\left|T_2^{(1)}\right| \end{bmatrix}, \quad (3.3.14)$$

where $\mathrm{K}^{(h)}$ is given by (3.3.7) with $\{\boldsymbol{b}_i\}_{i=1}^3$ provided by (3.1.4) and (3.1.2c), representing the hexagonal network geometry. The form of effective diffusivity tensor (3.3.14) is therefore different from the form of the corresponding tensor (3.3.7) obtained for the square and triangular networks. The additional matrix in (3.3.14) involving $T_j^{(1)}$ for $j = 1, 2$ arises due to the topological differences between the hexagonal network and the triangular and square networks.

3.3.1 Effective diffusivity via perturbative expansion

In the limit of $|\boldsymbol{p}| \to 0$ (corresponding to the limit $|\boldsymbol{\xi} - \boldsymbol{\xi}^*| \to 0$), we take the quadratic approximation for $f(\boldsymbol{p})$ given by (3.3.5) and the quadratic approximation for the eigenfunction

$$\phi_i^{(\boldsymbol{n})} = \phi_{i,0}^{(\boldsymbol{n})} + \phi_{i,1}^{(\boldsymbol{n})} |\boldsymbol{p}| + \phi_{i,2}^{(\boldsymbol{n})} |\boldsymbol{p}|^2 + O(|\boldsymbol{p}|^3), \quad \text{as } |\boldsymbol{p}| \to 0. \tag{3.3.15}$$

We first consider triangular and square networks. We introduce (3.3.5) and (3.3.15) inside the eigenvalue equation (3.2.4) and the boundary condition (3.2.6). At leading order we obtain

$$\partial^2_{\ell_i\ell_i}\phi_{i,0}^{(\boldsymbol{n})} - U_i \partial_{\ell_i}\phi_{i,0}^{(\boldsymbol{n})} = 0, \tag{3.3.16a}$$

and

$$\phi_{i,0}^{(\boldsymbol{n})}\big|_{\ell_i=0,1} = A, \tag{3.3.16b}$$

$$\sum_{i=1}^{N}\left(\partial_{\ell_i}\phi_{i,0}^{(\boldsymbol{n})}\big|_{\ell_i=0} - \partial_{\ell_i}\phi_{i,0}^{(\boldsymbol{n})}\big|_{\ell_i=1}\right) = 0, \tag{3.3.16c}$$

for $i = 1 \dots N$. The general solution to (3.3.16a) is

$$\phi_{i,0}^{(\boldsymbol{n})} = C_0 + D_0 e^{U_i \ell_i}, \tag{3.3.17}$$

where C_0 and D_0 are constants of integration. Then using the continuity condition (3.3.16b) it follows that $\phi_{i,0}^{(\boldsymbol{n})} = 1$, where we have let $A = 1$ without loss of generality. Using $\phi_{i,0}^{(\boldsymbol{n})} = 1$ the problem at $O(|\boldsymbol{p}|)$ now reduces to

$$\partial^2_{\ell_i\ell_i}\phi_{i,1}^{(\boldsymbol{n})} - U_i\partial_{\ell_i}\phi_{i,1}^{(\boldsymbol{n})} + U_i\boldsymbol{b}_i \cdot \hat{\boldsymbol{p}} = \boldsymbol{\xi}^* \cdot \hat{\boldsymbol{p}}, \tag{3.3.18a}$$

and

$$\phi_{i,1}^{(\boldsymbol{n})}\big|_{\ell_i=0,1} = 0, \tag{3.3.18b}$$

$$\sum_{i=1}^{N}\left(\partial_{\ell_i}\phi_{i,1}^{(\boldsymbol{n})}\big|_{\ell_i=0} - \partial_{\ell_i}\phi_{i,1}^{(\boldsymbol{n})}\big|_{\ell_i=1}\right) = 0, \tag{3.3.18c}$$

for $i = 1 \ldots N$, where $\hat{\boldsymbol{p}} = \boldsymbol{p}/|\boldsymbol{p}|$. We now average (3.3.18a) over the elementary cell from where we obtain

$$\boldsymbol{\xi}^* \cdot \hat{\boldsymbol{p}} = \frac{1}{N}\sum_{i=1}^{N}\int_0^1 (\partial^2_{\ell_i\ell_i}\phi_{i,1}^{(\boldsymbol{n})} - U_i\partial_{\ell_i}\phi_{i,1}^{(\boldsymbol{n})} + U_i\boldsymbol{b}_i \cdot \hat{\boldsymbol{p}})\, d\ell_i. \tag{3.3.19}$$

Applying (3.3.18b) and (3.3.18c) we recover (3.3.6) for the centre of mass velocity. The solution to (3.3.18a) is given by

$$\phi_{i,1}^{(\boldsymbol{n})} = \frac{C_1}{U_i}e^{U_i\ell_i} + D_1 - \frac{\ell_i}{U_i}\big(\boldsymbol{\xi}^* - U_i\boldsymbol{b}_i\big) \cdot \hat{\boldsymbol{p}}, \tag{3.3.20}$$

for $i = 1 \ldots N$, where C_1 and D_1 are constants of integration. Employing the continuity condition (3.3.18b) yields

$$\phi_{i,1}^{(\boldsymbol{n})} = \frac{\big(\boldsymbol{\xi}^* - U_i\boldsymbol{b}_i\big) \cdot \hat{\boldsymbol{p}}}{U_i(e^{U_i} - 1)}\left(e^{U_i\ell_i} + (1 - e^{U_i})\ell_i - 1\right), \tag{3.3.21}$$

for $i = 1 \ldots N$. At $O(|\boldsymbol{p}|^2)$ using (3.3.21) the problem is

$$\partial^2_{\ell_i\ell_i}\phi_{i,2}^{(\boldsymbol{n})} - U_i\partial_{\ell_i}\phi_{i,2}^{(\boldsymbol{n})} - 2\boldsymbol{b}_i \cdot \hat{\boldsymbol{p}}\partial_{\ell_i}\phi_{i,1}^{(\boldsymbol{n})} + U_i\boldsymbol{b}_i \cdot \hat{\boldsymbol{p}}\phi_{i,1}^{(\boldsymbol{n})} + (\boldsymbol{b}_i \cdot \hat{\boldsymbol{p}})^2 = \boldsymbol{\xi}^* \cdot \hat{\boldsymbol{p}}\phi_{i,1}^{(\boldsymbol{n})} + \hat{\boldsymbol{p}}^T\mathrm{K}\hat{\boldsymbol{p}}, \tag{3.3.22a}$$

and

$$\phi_{i,2}^{(\boldsymbol{n})}\big|_{\ell_i=0,1} = 0, \tag{3.3.22b}$$

$$\sum_{i=1}^{N}\Big(\partial_{\ell_i}\phi^{(\boldsymbol{n})}_{i,2}\big|_{\ell_i=0}-\partial_{\ell_i}\phi^{(\boldsymbol{n})}_{i,2}\big|_{\ell_i=1}\Big)=0, \tag{3.3.22c}$$

for $i=1\dots N$. Averaging (3.3.22a) and using (3.3.22b) and (3.3.22c) we obtain

$$\hat{\boldsymbol{p}}^T\mathrm{K}\hat{\boldsymbol{p}}=\frac{1}{N}\sum_{i=1}^{N}\left((U_i\boldsymbol{b}_i-\boldsymbol{\xi}^*)\cdot\hat{\boldsymbol{p}}\int_0^1\phi^{(\boldsymbol{n})}_{i,1}\,d\ell_i+(\boldsymbol{b}_i\cdot\hat{\boldsymbol{p}})^2\right). \tag{3.3.23}$$

We use (3.3.21) to obtain that

$$\hat{\boldsymbol{p}}^T\mathrm{K}\hat{\boldsymbol{p}}=\frac{1}{2N}\sum_{i=1}^{N}2(\boldsymbol{b}_i\cdot\hat{\boldsymbol{p}})^2-\frac{1}{2U_i^2}\Big((U_i\boldsymbol{b}_i-\boldsymbol{\xi}^*)\cdot\hat{\boldsymbol{p}}\Big)^2\Big(2-U_i\coth\frac{U_i}{2}\Big), \tag{3.3.24}$$

and (after simplifying the right-hand side) we recover expression (3.3.7) for the effective diffusivity tensor.

For the hexagonal network, the calculation is not as straightforward therefore we use Mathematica to solve the eigenvalue problems at $O(|\boldsymbol{p}|)$ and $O(|\boldsymbol{p}|^2)$. Introducing (3.3.5) and (3.3.15) to the the eigenvalue equation (3.2.4) together with the boundary condition (3.2.7), at leading order we obtain

$$\partial^2_{\ell_i\ell_i}\phi^{(\boldsymbol{n})}_{i,0}-U_i\partial_{\ell_i}\phi^{(\boldsymbol{n})}_{i,0}=0, \tag{3.3.25a}$$

and

$$\phi^{(\boldsymbol{n})}_{i,0}\big|_{\ell_i=0}=A\quad\text{and}\quad\phi^{(\boldsymbol{n})}_{i,0}\big|_{\ell_i=1}=B, \tag{3.3.25b}$$

$$\sum_{i=1}^{N}\partial_{\ell_i}\phi^{(\boldsymbol{n})}_{i,0}\big|_{\ell_i=0}=\sum_{i=1}^{N}\partial_{\ell_i}\phi^{(\boldsymbol{n})}_{i,0}\big|_{\ell_i=1}=0, \tag{3.3.25c}$$

for $i=1\dots N$. The general solution to (3.3.25a) is

$$\phi^{(\boldsymbol{n})}_{i,0}=e^{U_i/2}\left(C_0e^{\ell_iU_i/2}+D_0e^{-\ell_iU_i/2}\right), \tag{3.3.26}$$

where C_0 and D_0 are constants of integration. Employing the continuity condition (3.3.25b) yields

$$\phi^{(\boldsymbol{n})}_{i,0}=\frac{e^{\ell_iU_i/2}}{\sinh\big(U_i/2\big)}\Big(A\sinh\big((1-\ell_i)U_i/2\big)+Be^{-U_i/2}\sinh\big(\ell_iU_i/2\big)\Big). \tag{3.3.27}$$

Introducing (3.3.27) into (3.3.25c) yields a linear system of equations, from which we obtain $|\mathrm{T}^{(0)}| = 0$, where the matrix $\mathrm{T}^{(0)}$ is given by (3.3.11). The problem at $O(|\boldsymbol{p}|)$ is

$$\partial^2_{\ell_i\ell_i}\phi^{(\boldsymbol{n})}_{i,1} - U_i\partial_{\ell_i}\phi^{(\boldsymbol{n})}_{i,1} - 2\boldsymbol{b}_i\cdot\hat{\boldsymbol{p}}\partial_{\ell_i}\phi^{(\boldsymbol{n})}_{i,0} + U_i\boldsymbol{b}_i\cdot\hat{\boldsymbol{p}}\phi^{(\boldsymbol{n})}_{i,0} = \boldsymbol{\xi}^*\cdot\hat{\boldsymbol{p}}\phi^{(\boldsymbol{n})}_{i,0}, \tag{3.3.28a}$$

and

$$\phi^{(\boldsymbol{n})}_{i,1}\big|_{\ell_i=0} = 0 \quad\text{and}\quad \phi^{(\boldsymbol{n})}_{i,1}\big|_{\ell_i=1} = 0, \tag{3.3.28b}$$

$$\sum_{i=1}^{N}\partial_{\ell_i}(\phi^{(\boldsymbol{n})}_{i,0} + \phi^{(\boldsymbol{n})}_{i,1}|\boldsymbol{p}|)\big|_{\ell_i=0} = \sum_{i=1}^{N}\partial_{\ell_i}(\phi^{(\boldsymbol{n})}_{i,0} + \phi^{(\boldsymbol{n})}_{i,1}|\boldsymbol{p}|)\big|_{\ell_i=1} = 0, \tag{3.3.28c}$$

for $i = 1\ldots N$. The solution to (3.3.28a) is given by

$$\phi^{(\boldsymbol{n})}_{i,1} = \frac{e^{U_i\ell_i}(U_i\ell_i-1)(U_i\boldsymbol{b}_i+\boldsymbol{\xi}^*)\cdot\hat{\boldsymbol{p}}(B-A) - U_i\ell_i(U_i\boldsymbol{b}_i-\boldsymbol{\xi}^*)\cdot\hat{\boldsymbol{p}}(e^{U_i}A-B)}{(-1+e^{U_i})U_i^2} + \frac{e^{U_i\ell_i}}{U_i}C_1 + D_1, \tag{3.3.29}$$

where C_1 and D_1 are constants of integration. Then using continuity condition (3.3.28b) it follows

$$\begin{aligned}\phi^{(\boldsymbol{n})}_{i,1} =& \frac{\left((1-\ell_i)B + Ae^{U_i}\ell_i + ((B-A)\ell_i - B)e^{U_i\ell_i}\right)\boldsymbol{b}_i\cdot\hat{\boldsymbol{p}}}{(-1+e^{U_i})}\\ &+ \frac{(e^{U_i\ell_i}-1)(2e^{U_i}A-(1+e^{U_i})B) - (e^{U_i}-1)((e^{U_i}+e^{U_i\ell_i})A-(1+e^{U_i\ell_i})B)\ell_i}{(-1+e^{U_i})^2U_i}\boldsymbol{\xi}^*\cdot\hat{\boldsymbol{p}}.\end{aligned} \tag{3.3.30}$$

Applying (3.3.28c) to (3.3.30) we obtain

$$\sum_{j=1}^{2}(\mathrm{Tr}(\mathrm{T}^{(0)})\mathrm{Tr}(\mathrm{T}^{(1)}_j) - \mathrm{Tr}(\mathrm{T}^{(0)}\mathrm{T}^{(1)}_j))p_{l_j} = 0, \tag{3.3.31}$$

where $\mathrm{T}^{(1)}_j$ for $j = 1, 2$ are defined in (3.3.12). Solving (3.3.31) we recover (3.3.6) for the centre of mass velocity. At $O(|\boldsymbol{p}|^2)$ the problem is

$$\partial^2_{\ell_i\ell_i}\phi^{(\boldsymbol{n})}_{i,2} - U_i\partial_{\ell_i}\phi^{(\boldsymbol{n})}_{i,2} - (2\partial_{\ell_i}-U_i)\boldsymbol{b}_i\cdot\hat{\boldsymbol{p}}\phi^{(\boldsymbol{n})}_{i,1} + (\boldsymbol{b}_i\cdot\hat{\boldsymbol{p}})^2\phi^{(\boldsymbol{n})}_{i,0} = \boldsymbol{\xi}^*\cdot\hat{\boldsymbol{p}}\phi^{(\boldsymbol{n})}_{i,1} + \hat{\boldsymbol{p}}^T\mathrm{K}\hat{\boldsymbol{p}}\phi^{(\boldsymbol{n})}_{i,0}, \tag{3.3.32a}$$

and

$$\phi^{(\boldsymbol{n})}_{i,2}\big|_{\ell_i=0} = 0 \quad\text{and}\quad \phi^{(\boldsymbol{n})}_{i,2}\big|_{\ell_i=1} = 0, \tag{3.3.32b}$$

$$\sum_{i=1}^{N}\partial_{\ell_i}(\phi_{i,0}^{(\boldsymbol{n})}+\phi_{i,1}^{(\boldsymbol{n})}\,|\boldsymbol{p}|+\phi_{i,2}^{(\boldsymbol{n})}\,|\boldsymbol{p}|^2)\big|_{\ell_i=0}=\sum_{i=1}^{N}\partial_{\ell_i}(\phi_{i,0}^{(\boldsymbol{n})}+\phi_{i,1}^{(\boldsymbol{n})}\,|\boldsymbol{p}|+\phi_{i,2}^{(\boldsymbol{n})}\,|\boldsymbol{p}|^2)\big|_{\ell_i=1}=0, \tag{3.3.32c}$$

for $i = 1 \dots N$. The solution to (3.3.32a) is given by

$$\begin{aligned}\phi_{i,2}^{(\boldsymbol{n})} =&\frac{1}{2(-1+e^{U_i})^2U_i^4}(2U_i^2(\boldsymbol{\xi}^*\cdot\hat{\boldsymbol{p}})(\boldsymbol{b}_i\cdot\hat{\boldsymbol{p}})((-A+B)e^{U_i(1+\ell_i)}(2+U_i(-2+\ell_i)\ell_i)+U_i\ell_i((A-B)e^{U_i\ell_i}\ell_i\\&+(B-Ae^{U_i})(2+(-1+e^{U_i})\ell_i)))+(-1+e^{U_i})U_i^2(2\hat{\boldsymbol{p}}^T\mathrm{K}\hat{\boldsymbol{p}}((B-Ae^{U_i})U_i\ell_i\\&+(-A+B)e^{U_i\ell_i}(-1+U_i\ell_i))+U_i(\boldsymbol{b}_i\cdot\hat{\boldsymbol{p}})^2(U_i\ell_i(2B+(-B+Ae^{U_i})\ell_i)\\&+e^{U_i\ell_i}(2B+U_i\ell_i(-2B+(-A+B)\ell_i))))+(\boldsymbol{\xi}^*\cdot\hat{\boldsymbol{p}})^2(-2(A-B)e^{U_i\ell_i}(-1+e^{U_i})\\&+U_i(2e^{U_i\ell_i}(B+(-2A+B)e^{U_i})+\ell_i(2(-1+e^{U_i})(-B+Ae^{U_i}+(A-B)e^{U_i\ell_i}\\&+U_i(-2(B+(-2A+B)e^{U_i})(-1+e^{U_i\ell_i})+(-1+e^{U_i})(-B+Ae^{U_i}+(-A+B)e^{U_i\ell_i})\ell_i))))))\\&+\frac{e^{U_i\ell_i}}{U_i}C_2+D_2,\end{aligned} \tag{3.3.33}$$

for $i = 1 \dots N$, where C_2 and D_2 are constants of integration. Then using continuity condition (3.3.32b) we find

$$\begin{aligned}\phi_{i,2}^{(\boldsymbol{n})} =&\frac{1}{2(-1+e^{U_i})^3U_i^3}(2(-1+e^{U_i})U_i^2(\boldsymbol{\xi}^*\cdot\hat{\boldsymbol{p}})(\boldsymbol{b}_i\cdot\hat{\boldsymbol{p}})(B(1+e^{U_i})(-1+e^{U_i\ell_i})+2(B-Ae^{U_i}\\&+(A-B)e^{U_i(1+\ell_i)})\ell_i+(-1+e^{U_i})(B-Ae^{U_i}+(-A+B)e^{U_i\ell_i})\ell_i^2)\\&+(\boldsymbol{\xi}^*\cdot\hat{\boldsymbol{p}})^2(2(-1+e^{U_i})((B+(-2A+B)e^{U_i})(-1+e^{U_i\ell_i})+(-1+e^{U_i})(-B+Ae^{U_i}\\&+(A-B)e^{U_i\ell_i})\ell_i)+U_i((B+2(-2A+3B)e^{U_i}+(-4A+B)e^{2U_i})(-1+e^{U_i\ell_i})\\&+(-1+e^{U_i})(-2(B+(-2A+B)e^{U_i})(1+e^{U_i\ell_i})+(-1+e^{U_i})(-B+Ae^{U_i}\\&+(-A+B)e^{U_i\ell_i})\ell_i)\ell_i))+(-1+e^{U_i})U_i^2(2\hat{\boldsymbol{p}}^T\mathrm{K}\hat{\boldsymbol{p}}((-B+(2A-B)e^{U_i})(-1+e^{U_i\ell_i})\\&+(-1+e^{U_i})(B-Ae^{U_i}+(-A+B)e^{U_i\ell_i})\ell_i)+(-1+e^{U_i})U_i(\boldsymbol{b}_i\cdot\hat{\boldsymbol{p}})^2(-B+2B\ell_i-B\ell_i^2\\&+Ae^{U_i}\ell_i^2+e^{U_i\ell_i}(B-2B\ell_i+(-A+B)\ell_i^2)))),\end{aligned} \tag{3.3.34}$$

for $i = 1 \dots N$. Applying (3.3.32c) to (3.3.34) we obtain

$$\sum_{j=1}^{2}(|\mathrm{T}_j^{(1)}| - \mathrm{Tr}(\mathrm{T}^{(0)}\mathrm{T}_{jj}^{(2)}))p_{l_j}^2 - (\mathrm{Tr}(\mathrm{T}_1^{(1)}\mathrm{T}_2^{(1)}) + \mathrm{Tr}(\mathrm{T}^{(0)}\mathrm{T}_{12}^{(2)}))p_{l_1}p_{l_2} = 0, \tag{3.3.35}$$

where $\mathrm{T}_{jk}^{(2)}$ for $j, k = 1, 2$ are given in (3.3.13). Finally solving (3.3.35) we recover expression (3.3.14) for the effective diffusivity tensor.

It is clear that performing a perturbative expansion of the eigenvalue problem is feasible thus allowing us to recover the centre of mass velocity and the effective diffusivity tensor. However, the approach is rather inefficient, requiring the calculation of $\phi_{i,0}^{(\boldsymbol{n})}$,$\phi_{i,1}^{(\boldsymbol{n})}$ and $\phi_{i,2}^{(\boldsymbol{n})}$ which is rather intensive when compared to the calculation of $\phi_i^{(\boldsymbol{n})}$ which is straightforward (see (3.2.8) or (3.2.11)).

3.3.2 Asymptotic regimes

We now have a complete description of dispersion in the effective diffusion regime. The explicit expressions (3.3.6), (3.3.7) and (3.3.14) describe the complex interaction between advection and diffusion controlling scalar dispersion in periodic networks. Figure 3.2 shows ellipses of constant $\boldsymbol{x}^T\mathrm{K}^{-1}\boldsymbol{x}$ (which corresponds to a constant concentration), obtained for a range of positive values of U_x and U_y in the $\boldsymbol{U}$-plane (other regions in the plane are obtained by exploiting the symmetries of the networks). It demonstrates that scalar dispersion can vary significantly between the three networks in both magnitude and direction. The figure illustrates interesting features, such as anisotropy, which is weak for triangular networks but can be very pronounced for square networks. For small U_x, U_y or equivalently, for all $i = 1 \dots N$, $|U_i|$ is small (i.e. all Péclet numbers are small),

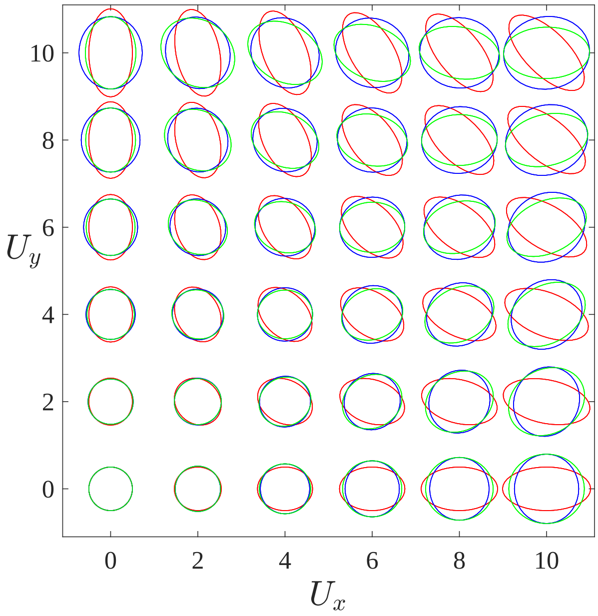

Figure 3.2: Ellipses of constant $\boldsymbol{x}^T \mathrm{K}^{-1} \boldsymbol{x}$ representing the effective diffusivity tensor K as a function of U_x and U_y for the square network (red), triangular network (blue) and hexagonal network (green). The results for the square network have been reproduced from [87].

we use the asymptotic formulas

$$\coth x = 1/x + x/3 + O(x^3), \quad a(x) = -2x/3 + O(x^3), \quad b(x) = x/6 + O(x^3), \quad \text{as } x \to 0, \tag{3.3.36}$$

inside (3.3.7) and (3.3.14) from where we obtain that, for all three networks, when $|U_i| \ll 1$, the effective diffusivity tensor may be approximated by

$$\mathrm{K}_{11} \sim \frac{1}{2} + \frac{1}{12N} \sum_{i=1}^{N} (\xi_x^* - U_i \boldsymbol{b}_i \cdot \boldsymbol{e}_1)^2, \tag{3.3.37a}$$

$$\mathrm{K}_{12} \sim \frac{1}{12N} \sum_{i=1}^{N} (\xi_x^* - U_i \boldsymbol{b}_i \cdot \boldsymbol{e}_1)(\xi_y^* - U_i \boldsymbol{b}_i \cdot \boldsymbol{e}_2), \tag{3.3.37b}$$

where K_{22} is obtained from K_{11} by taking $\boldsymbol{e}_1 \mapsto \boldsymbol{e}_2$ and $\xi_x^* \mapsto \xi_y^*$. Thus, in this limit, the three networks share the same leading-order effective behaviour, which corresponds to the leading-order effective behaviour obtained in the absence of advection [85]. From (3.3.37) it is easy to see that higher-order corrections to the leading-order behaviour are $O(|U_x|^2, |U_y|^2)$ and therefore the effect of advection is very weak in this limit (see Figure 3.2).

For large U_x and U_y, the behaviour of the effective diffusivity tensor depends on the orientation of the flow relative to the network (see Figure 3.2). We can distinguish two cases. The first case corresponds to when for all $i = 1 \ldots N$, $|U_i| \gg 1$ (i.e. all Péclet numbers are large). In this case, the components of the effective diffusivity tensor are at leading order linearly dependent on U_i. Dimensionally this corresponds to components that are independent of the molecular diffusivity κ corresponding to a regime termed geometric [20] or mechanical [77, 49] dispersion. For triangular and square networks we use the asymptotic formula $\coth x \sim x/|x|$ as $|x| \to \infty$ inside (3.3.7) to obtain that at leading order

$$\mathrm{K}_{11} \sim \frac{1}{2N} \sum_{i=1}^{N} |U_i|^{-1} (\xi_x^* - U_i \boldsymbol{b}_i \cdot \boldsymbol{e}_1)^2, \tag{3.3.38a}$$

$$\mathrm{K}_{12} \sim \frac{1}{2N} \sum_{i=1}^{N} |U_i|^{-1} (\xi_x^* - U_i \boldsymbol{b}_i \cdot \boldsymbol{e}_1)(\xi_y^* - U_i \boldsymbol{b}_i \cdot \boldsymbol{e}_2), \tag{3.3.38b}$$

where K_{22} is obtained from K_{11} in the same way as before. For the hexagonal networks we use the additional asymptotic formulas

$$a(x) \sim -2x/|x|, \quad b(x) \sim 2 - |x|, \quad c_{\pm}(x) \sim \mp 2e^{(\pm x - |x|)/2} x/|x|, \quad \text{as } |x| \to \infty, \tag{3.3.39}$$

inside (3.3.12) to determine a leading order expression for $\{\mathrm{T}_j^{(1)}\}_{j=1}^{2}$ from where we deduce that

$$|\mathrm{T}_1^{(1)}| \sim \sum_{\substack{i,U_i>0\\ j,U_j<0}} (\xi_x^* - U_i\boldsymbol{b}_i\cdot\boldsymbol{e}_1)(\xi_x^* - U_j\boldsymbol{b}_j\cdot\boldsymbol{e}_1), \quad |\mathrm{T}_2^{(1)}| \sim \sum_{\substack{i,U_i>0\\ j,U_j<0}} (\xi_y^* - U_i\boldsymbol{b}_i\cdot\boldsymbol{e}_2)(\xi_y^* - U_j\boldsymbol{b}_j\cdot\boldsymbol{e}_2), \tag{3.3.40a}$$

and

$$\mathrm{Tr}(T_1^{(1)}T_2^{(1)}) \sim -\sum_{\substack{i,U_i>0\\ j,U_j<0}} (\xi_x^* - U_j\boldsymbol{b}_j\cdot\boldsymbol{e}_1)(\xi_y^* - U_i\boldsymbol{b}_i\cdot\boldsymbol{e}_2) + (\xi_y^* - U_j\boldsymbol{b}_j\cdot\boldsymbol{e}_2)(\xi_x^* - U_i\boldsymbol{b}_i\cdot\boldsymbol{e}_1). \tag{3.3.40b}$$

Employing (3.3.40) inside (3.3.14) yields, at leading order,

$$\mathrm{K}_{11} \sim \frac{1}{6}\sum_{i=1}^{3}\frac{1}{|U_i|}(\xi_x^* - U_i\boldsymbol{b}_i\cdot\boldsymbol{e}_1)^2 + \frac{2}{3\sum_{i=1}^{3}|U_i|}\sum_{\substack{i,U_i>0\\ k,U_j<0}} (\xi_x^* - U_i\boldsymbol{b}_i\cdot\boldsymbol{e}_1)(\xi_x^* - U_j\boldsymbol{b}_j\cdot\boldsymbol{e}_1), \tag{3.3.41a}$$

$$\mathrm{K}_{12} \sim \frac{1}{6}\sum_{i=1}^{3}\frac{1}{|U_i|}(\xi_x^* - U_i\boldsymbol{b}_i\cdot\boldsymbol{e}_1)(\xi_y^* - U_i\boldsymbol{b}_i\cdot\boldsymbol{e}_2) + \frac{1}{3\sum_{i=1}^{3}|U_i|}\sum_{\substack{i,U_i>0\\ j,U_j<0}} (\xi_y^* - U_i\boldsymbol{b}_i\cdot\boldsymbol{e}_2)(\xi_x^* - U_j\boldsymbol{b}_j\cdot\boldsymbol{e}_1)$$
$$+ (\xi_x^* - U_i\boldsymbol{b}_i\cdot\boldsymbol{e}_1)(\xi_y^* - U_j\boldsymbol{b}_j\cdot\boldsymbol{e}_2), \tag{3.3.41b}$$

where K_{22} is obtained from K_{11} as before.

For the square and hexagonal networks, the effective diffusivity tensor K is singular to leading order in U_i. This corresponds to an effective diffusion that is strong in one direction and weak in another direction (see Figure 3.2). For the triangular networks, K is not singular at leading order and both eigenvalues are of the same order. This explains the nearly isotropic behaviour observed in this regime. The direction along which effective diffusion is strong or weak (obtained by analysing the eigensystem) differs between the square and hexagonal networks. For the square networks, effective diffusion is strong in the direction $(-U_x, U_y)$ and weak along the direction of the flow. For the hexagonal networks effective diffusion is strong along the direction $(2U_y, 1 - U_y^2/U_x)$ and weak along the perpendicular direction. This explains the nearly diagonal and horizontal alignment of the effective diffusion observed respectively for square and hexagonal networks when $U_x \sim U_y \gg 1$. Contrasting the two networks, it is easy to see that effective diffusion is strongest for the square network and weakest for the hexagonal network (see also Figure 3.2).

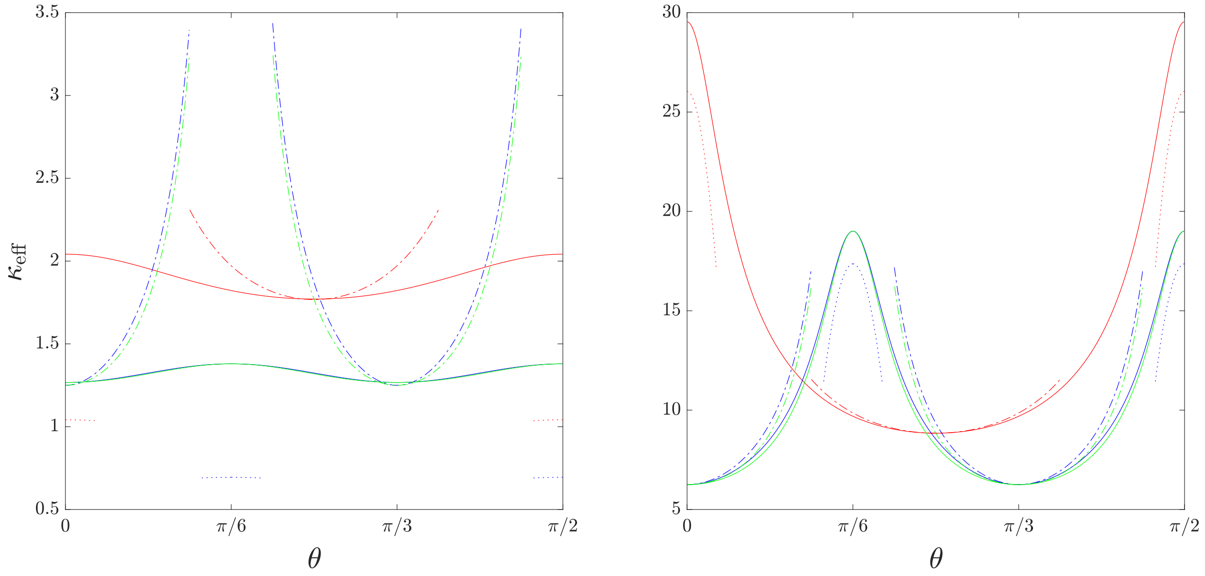

Figure 3.3: Maximum effective diffusivity as a function of the flow orientation θ. Results are shown for square (red solid line), triangular (blue solid) and hexagonal (green solid) networks and for flows: (left) $(U_x, U_y) = 10(\cos\theta, \sin\theta)$ and (right) $50(\cos\theta, \sin\theta)$. These are compared against the asymptotic approximations (3.3.38) or (3.3.41) (dashed-dotted lines) and (3.3.42) (dotted lines).

The behaviour of effective diffusion changes drastically when the flow becomes nearly perpendicular to one of the network edges. Employing the asymptotic formulas

(3.3.36) and (3.3.39) inside (3.3.7) and (3.3.14) we obtain that for all three networks,

$$\mathrm{K}_{11} \sim \frac{1}{48N} U_x^2, \quad \mathrm{K}_{12} \sim \frac{1}{48N} U_x U_y, \quad \mathrm{K}_{22} \sim \frac{1}{48N} U_y^2, \tag{3.3.42}$$

where the magnitude of U_x and U_y depends on the type of network. For the square network, this case is achieved when $U_x \gg 1$ and $U_y \ll 1$ (i.e. when the flow angle $\theta \sim 0$) or $U_x \ll 1$ and $U_y \gg 1$ (i.e. when the flow angle $\theta \sim \pi/2$). This corresponds to a mostly longitudinal or latitudinal diffusivity with a κ^{-1} scaling characteristic of Taylor dispersion [83]. For the triangular and hexagonal networks, this is achieved when $U_x \ll 1$ and $U_y \gg 1$ (i.e. when the flow angle $\theta \sim \pi/2$) or $U_x \sim \sqrt{3} U_y \gg 1$ (i.e. when the flow angle $\theta \sim \pi/6$). In both cases the diffusivity is mostly oriented along the same direction as the flow. Using (3.3.42) it is easy to see that at leading order, effective diffusion is strongest for the square network and weakest for the triangular and hexagonal networks, achieving the same magnitude irrespective of the flow orientation.

We now compare the asymptotic results obtained for large U_x and U_y against numerical results. We focus on the maximum effective diffusivity corresponding to the maximum eigenvalue of (3.3.7) and (3.3.14) and consider two flow strengths both in the strong flow regime. Figure 3.3 shows that the agreement is very good only for the stronger flow in the mechanical dispersion regime. This is expected because higher order corrections to (3.3.42) are $O(U_x, U_y)$ and (3.3.38) and (3.3.41) are $O(1)$. Thus, a better agreement at moderately strong flows and both regimes can only be achieved when higher order corrections are included.

In all cases of large U_x and U_y, effective diffusion is weakest for the triangular network. This is expected because the triangular network has the largest vertex connectivity. However, the results show that connectivity alone cannot explain why effective diffusion is strongest for the square network which has a larger vertex connectivity than the hexagonal network. Thus both geometry and topology have a role in determining the dispersive properties of networks. Their combined effect can be captured by random-walk models with correlation time determined by advection in the geometric regime and molecular diffusion in the Taylor regime [51]. These models can be used to understand why in both geometric and Taylor regimes, effective diffusion is strongest for the square network.

3.4 Rate function

For a complete description of dispersion we analyse the rate function g. Figure 3.4 focuses on g obtained for $U_x = U_y = 0$ and 5 and contrasts its behaviour against the quadratic approximation (3.3.1) associated with the diffusive (Gaussian) approximation (3.3.2). For values of $\boldsymbol{\xi}$ near $\boldsymbol{\xi}^*$, the quadratic approximation with circular contours for $U_x = U_y = 0$ (top row) and elliptical contours for $U_x = U_y \neq 0$ (bottom row), perfectly matches with g. Beyond this neighbourhood of $\boldsymbol{\xi}^*$, the difference between the quadratic approximation and g can be significant (corresponding to an exponentially large difference between θ and (3.3.2)). For $U_x = U_y = 0$, the difference is most marked for the square network for which g is highly anisotropic (except for $\xi_x = \xi_y$ in which case g coincides with its quadratic approximation [87]) and least obvious for the triangular network for which g remains nearly isotropic for a larger range of values of $\boldsymbol{\xi}$. The small range of validity of the diffusive (Gaussian) approximation is further highlighted Figure 3.5. For the triangular

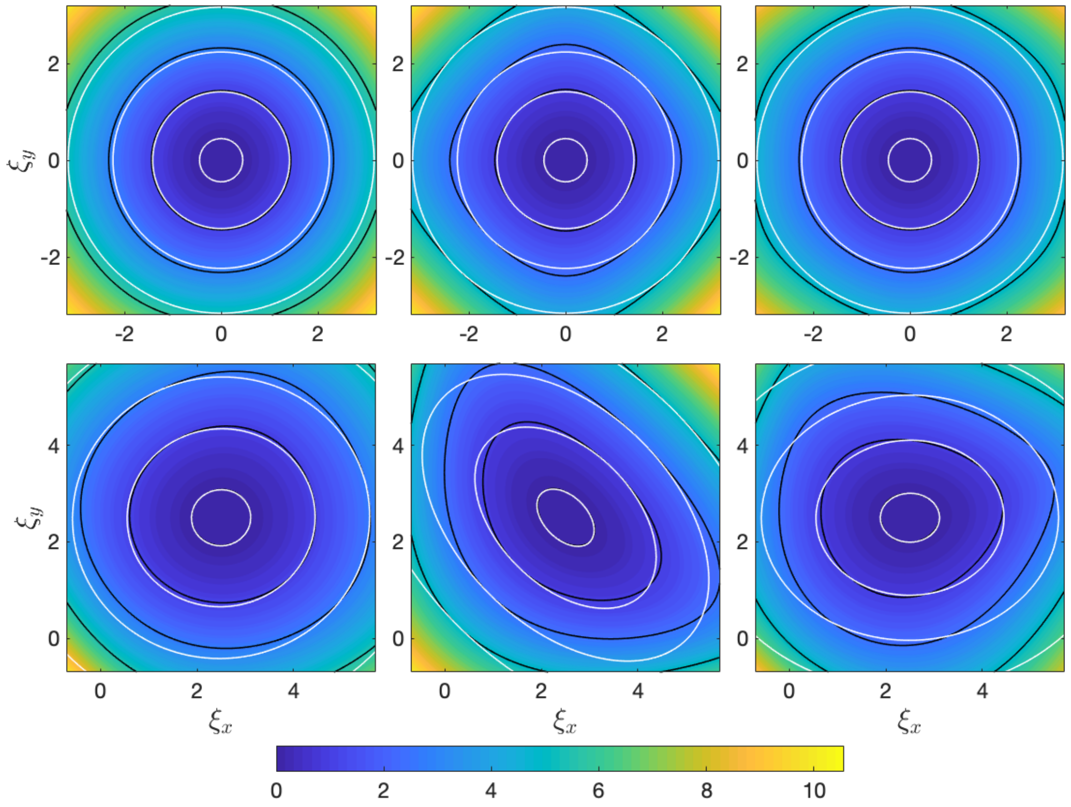

Figure 3.4: Rate function g for (left) triangular (middle) square and (right) hexagonal networks calculated numerically using equations (3.2.10) and (3.2.13), respectively. These are shown for (top row) $(U_x, U_y) = (0, 0)$ and (bottom row) $(5, 5)$. Selected contours (with values $0.1, 1, 2.5$ and 5) compare g (black) with its quadratic approximation (white) corresponding to the diffusive (Gaussian) approximation (3.3.2). This approximation is clearly valid near the minimum $\boldsymbol{\xi}^*$ of g. The results for the square network are in agreement with those obtained in [87].

network the difference only becomes significant for larger distances from the centre of mass (not shown).

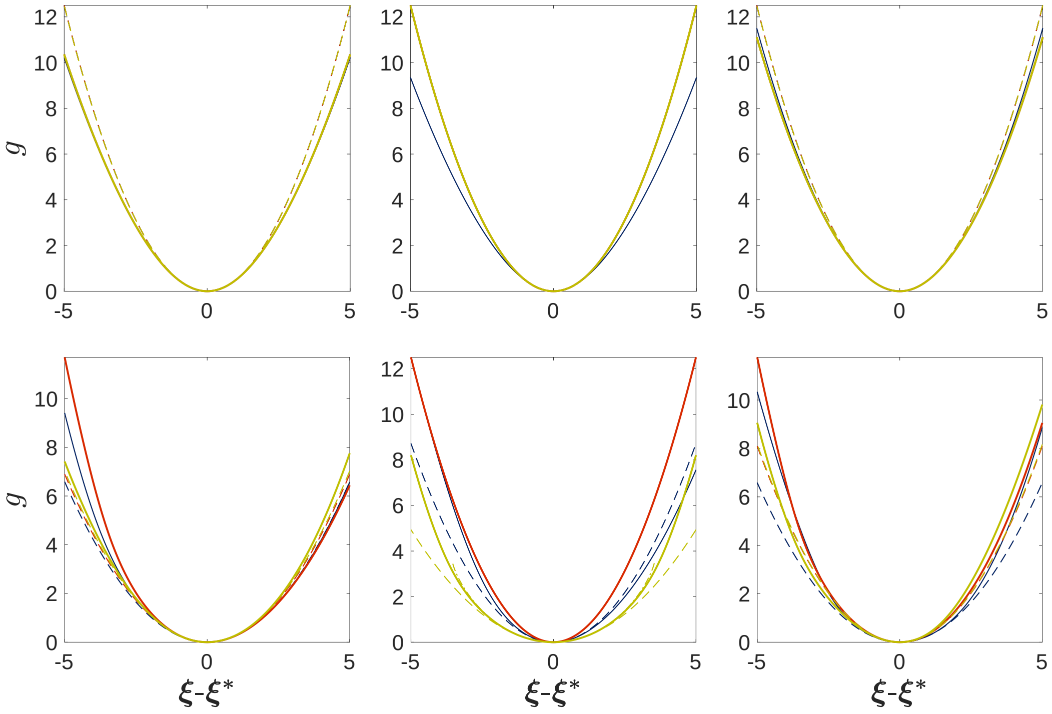

Figure 3.5: Cross sections of the rate function g for (left) triangular, (middle) square and (right) hexagonal networks, for flows (top) $(U_x, U_y) = (0,0)$ and (bottom) $(5,5)$. The large-deviation (3.2.1) (solid lines) is compared against the diffusive (Gaussian) approximation (3.3.2) (dashed lines) along the directions $(1,0)$ (blue), $(1,1)$ (red) and $(1,-1)$ (yellow), and large Péclet approximation derived from (3.4.12) and (3.4.14) (dashed-dotted) along the directions $(1,1)$ for the square network.

3.4.1 Tail regime

The large-$\boldsymbol{\xi}$ behaviour of $g(\boldsymbol{\xi})$ can be obtained by considering the large-$\boldsymbol{p}$ behaviour of f. We focus on the distinguished scaling $\{U_i\}_{i=1}^N = O(|\boldsymbol{p}|)$, which from (3.2.9) implies that $\{\mu_i\}_{i=1}^N = O(|\boldsymbol{p}|)$. For the triangular and square networks, f is given by (3.2.10) which in this limit reduces to

$$\sum_{i=1}^{N} \nu_i \left(2\cosh \mu_i e^{-\nu_i} - 1\right) \sim 0. \tag{3.4.1}$$

A solution to (3.4.1) exists only if $\sup\{|\mu_i| - \nu_i : i = 1, \ldots, N\} \sim 0$. Using (3.2.9), this constraint becomes

$$\sup\{|\boldsymbol{b}_i \cdot \boldsymbol{p} + U_i/2| - \sqrt{U_i^2/4 + f(\boldsymbol{p})} : i = 1, \ldots, N\} \sim 0 \tag{3.4.2}$$

which can be shown to further simplify as

$$f(\boldsymbol{p}) \sim \sup\{(\boldsymbol{b}_i \cdot \boldsymbol{p})^2 + U_i \boldsymbol{b}_i \cdot \boldsymbol{p} : i = 1, \ldots, N\}, \tag{3.4.3}$$

thus generalising expression (15) in [87]. For the hexagonal networks f is given by (3.2.13) which for large $\boldsymbol{p}$ reduces to

$$\sum_{i,j=1}^{3} \nu_i \nu_j (4e^{-\mu_i + \mu_j - \nu_i - \nu_j} - 1) \sim 0. \tag{3.4.4}$$

The constraint for a solution to (3.4.4) to exist is now given by $\sup\{\mu_j - \mu_i - \nu_i - \nu_j : i, j = 1 \ldots, 3\} \sim 0$. Using (3.2.9) the constraint becomes

$$\sup\{(\boldsymbol{b}_j - \boldsymbol{b}_i) \cdot \boldsymbol{p} + (U_j - U_i)/2 - \sqrt{U_i^2/4 + f(\boldsymbol{p})} - \sqrt{U_j^2/4 + f(\boldsymbol{p})} : i, j = 1, \ldots, 3\} \sim 0 \tag{3.4.5}$$

which after expanding to $O(|\boldsymbol{p}|)$ simplifies according to

$$f(\boldsymbol{p}) \sim \frac{1}{4} \sup\{((\boldsymbol{b}_j - \boldsymbol{b}_i) \cdot \boldsymbol{p})^2 + (U_j - U_i)(\boldsymbol{b}_j - \boldsymbol{b}_i) \cdot \boldsymbol{p} : i, j = 1 \ldots, 3\}. \tag{3.4.6}$$

The expressions for Legendre transform for (3.4.3) and (3.4.6) are unwieldy except when $\{U_i\}_{i=1}^N = 0$. In this case, (3.4.3) and (3.4.6) respectively become

$$f(\boldsymbol{p}) \sim \begin{cases} (\sup\{|\boldsymbol{b}_i \cdot \boldsymbol{p}| : i = 1, \ldots, N\})^2, & \text{for triangular and square networks,} \\ (\frac{1}{2} \sup\{|\boldsymbol{a}_i \cdot \boldsymbol{p}| : i = 1, \ldots, 3\})^2, & \text{for hexagonal networks,} \end{cases} \tag{3.4.7}$$

where $\boldsymbol{a}_1$ and $\boldsymbol{a}_2$ are given by (3.1.2c) and $\boldsymbol{a}_3 = \boldsymbol{a}_2 - \boldsymbol{a}_1$. (the same result can be obtained from (3.2.14). Equation (3.4.7) may be viewed as the square of a polygonal norm $\|\boldsymbol{p}\|^2$ (which for the square network case corresponds to the square of the ℓ^∞-norm) with unit ball centred at the origin, corresponding to a regular hexagon for the triangular and hexagonal cases and a square for the square case. The Legendre transform of a norm squared is proportional to the dual norm squared (see [21], example 3.27) where the dual norm is given by $\|\boldsymbol{\xi}\|_* = \sup\{\boldsymbol{\xi} \cdot \boldsymbol{p} \,|\, \|\boldsymbol{p}\| \leqslant 1\}$. Thus,

$$g(\boldsymbol{\xi}) \sim \frac{1}{4}\|\boldsymbol{\xi}\|_*^2 = \begin{cases} \frac{1}{4}\left(\sup\{|\boldsymbol{b}^i \cdot \boldsymbol{\xi}| : i = 1, \ldots, N\}\right)^2, & \text{for triangular and square networks,} \\ \frac{1}{4}\left(\sup\{|\boldsymbol{a}^i \cdot \boldsymbol{\xi}| : i = 1, \ldots, 3\}\right)^2, & \text{for hexagonal networks,} \end{cases} \tag{3.4.8a}$$

where $\{\boldsymbol{a}^i\}_{i=1}^3$ and $\{\boldsymbol{b}^i\}_{i=1}^N$ denote the position of vertices of the polygon $\|\boldsymbol{p}\| = 1$. For the triangular network, the vertices are

$$\boldsymbol{b}^1 = \frac{1}{\sqrt{3}}(\sqrt{3}, -1)^T, \quad \boldsymbol{b}^2 = \frac{1}{\sqrt{3}}(-\sqrt{3}, -1)^T, \quad \text{and} \quad \boldsymbol{b}^3 = \frac{2}{\sqrt{3}}(0, 1)^T \tag{3.4.8b}$$

while for the square network they are

$$\boldsymbol{b}^1 = (0, 1)^T \quad \text{and} \quad \boldsymbol{b}^2 = (1, 0)^T. \tag{3.4.8c}$$

Finally, for the hexagonal network the vertices are

$$\boldsymbol{a}^1 = \frac{2}{3}(1, \sqrt{3})^T, \quad \boldsymbol{a}^2 = \frac{2}{3}(1, -\sqrt{3})^T \quad \text{and} \quad \boldsymbol{a}^3 = \frac{4}{3}(1, 0)^T. \tag{3.4.8d}$$

Equation (3.4.8) implies a concentration $\theta \sim \exp\Big(-\|\boldsymbol{x}\|_*^2/(4t)\Big)$. It can be interpreted as a generalised form of diffusion with the Euclidian distance replaced by a polygonal norm (which for the square case corresponds to the ℓ^1-norm). It can be shown that the polygonal norm is the distance along the shortest path on the network between $\boldsymbol{x}$ and the origin (where the shortest path is not unique).

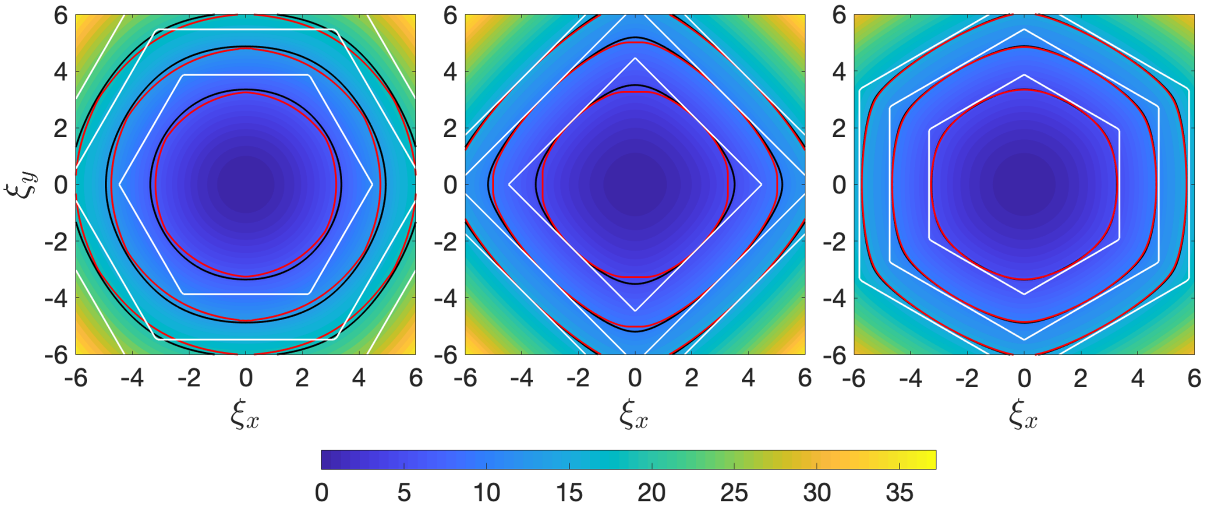

Figure 3.6: Rate function g calculated numerically from (3.2.10) and (3.2.13) in the absence of a flow for (left) triangular (middle) square and (right) hexagonal networks calculated numerically using equations (3.2.10) and (3.2.13). Selected contours (with values $5, 10$ and 15) compare g (black) against the large-$|\boldsymbol{\xi}|$ leading order approximation (3.4.8) (white) and higher-order correction (red) extracted from (3.2.14).

Figure 3.6 shows that the leading-order approximation (3.4.8) captures the diamond and hexagonal shaped contours of g obtained for the square and hexagonal network even for moderate values of $\boldsymbol{\xi}$; it provides an excellent approximation except along the directions of $\{\boldsymbol{a}^i\}_{i=1}^3$ and $\{\boldsymbol{b}^i\}_{i=1}^N$ where (3.4.8) overestimates g (and thus underestimates θ). For the triangular network, the approximation is only effective for values of $\boldsymbol{\xi}$ larger than 15 (not shown). A higher-order correction to (3.4.8) can be obtained by expanding (3.2.14) to $O(|\boldsymbol{p}|)$ and carrying out a numerical Legendre transform. Figure 3.6 shows that the higher-order correction is excellent for the moderate values of $\boldsymbol{\xi}$ considered.

For large $\{U_i\}_{i=1}^N$, the leading-order term in (3.4.3) and (3.4.6) respectively become

$$f(\boldsymbol{p}) \sim \begin{cases} \sup\{|U_i \boldsymbol{b}_i \cdot \boldsymbol{p}| : i = 1, \ldots, N\}, & \text{for triangular and square networks,} \\ \sup\{\frac{1}{4}|V_i \boldsymbol{a}_i \cdot \boldsymbol{p}| : i = 1, \ldots, 3\}, & \text{for hexagonal networks,} \end{cases} \tag{3.4.9}$$

where $V_1 = U_1 - U_3$ and $V_2 = U_2 - U_3$ and $V_3 = U_2 - U_1$. This time the leading-order behaviour depends linearly on a polygonal norm $\|\boldsymbol{p}\|$. The Legendre transform of a norm is the indicator function of the dual norm unit ball (see [21], example 3.26). Thus,

$$g(\boldsymbol{\xi}) \sim \begin{cases} 0, & \|\boldsymbol{\xi}\|_* \leqslant 1, \\ \infty, & \text{otherwise.} \end{cases} \tag{3.4.10}$$

For the square network case, it is easy to find that $\|\boldsymbol{\xi}\|_* = |\xi_x/U_x| + |\xi_y/U_y|$. Equation (3.4.10) implies that the concentration vanishes for $\|\boldsymbol{\xi}\|_* > 1$, reflecting a finite propagation speed of the scalar that exists when molecular diffusion is neglected against advection.

3.4.2 The large-Péclet regime

We last focus on the large-Péclet behaviour of $g(\boldsymbol{\xi})$ when $\boldsymbol{\xi} = O(1)$. This is obtained by considering the behaviour of f for $U_x,\ U_y \gg 1$ with $\{U_i\}_{i=1}^N \neq 0$ and $\boldsymbol{p} = O(1)$. For the triangular and square networks, f is given by (3.2.10) using $\sinh x \sim \frac{x}{|x|} e^{|x|}/2$ and $\cosh x \sim e^{|x|}/2$ as $|x| \to \infty$, (3.2.10) is approximated by

$$\sum_{i=1}^{N} \nu_i \left(e^{|\mu_i| - \nu_i} - 1 \right) \sim 0. \tag{3.4.11}$$

Using (3.2.9) with $\nu_i \sim |U_i|/2 + f/|U_i|$, equation (3.4.11) becomes

$$\sum_{i=1}^{N} |U_i| \left(e^{(U_i \boldsymbol{b}_i \cdot \boldsymbol{p} - f)/|U_i|} - 1 \right) \sim 0. \tag{3.4.12}$$

For the hexagonal networks, f is given by (3.2.13) which for large $\{U_i\}_{i=1}^N$ and $\boldsymbol{p} = O(1)$ reduces to

$$\sum_{i,j=1}^{3} \nu_i \nu_j (4e^{-\mu_i+\mu_j-\nu_i-\nu_j} - 1) \sim 0 \tag{3.4.13}$$

or, equivalently, upon using (3.2.9),

$$\sum_{i,j=1}^{3} |U_i||U_j|(4e^{-(\boldsymbol{b}_i-\boldsymbol{b}_j)\cdot\boldsymbol{p}-U_i/2-|U_i|/2+U_j/2-|U_j|/2-f/|U_i|-f/|U_j|} - 1) \sim 0. \tag{3.4.14}$$

Expanding (3.4.12) and (3.4.14) for small $\boldsymbol{p}$ recovers and subsumes the diffusive approximation in the geometric or mechanical dispersion regime i.e. with effective diffusivity tensors given by (3.3.38) and (3.3.41) (calculations not shown). From (3.4.12) and (3.4.14) it is clear that $f = O(\{U_i\}_{i=1}^N)$ and thus independent of molecular diffusivity. Therefore the notion of geometric or mechanical dispersion generalises to the large-deviation regime.

Equations (3.4.12) and (3.4.14) cannot be solved analytically. We instead seek for their numerical solution using MATLAB's *fsolve*, then taking a numerical Legendre transform to deduce an approximation for g in the large-Péclet regime. Figure 3.5 (bottom row) shows that the approximation for g provides an improvement to the diffusive approximation for $\|\boldsymbol{\xi}\|_* < 1$ (see (3.4.10)) which for the square network case (bottom, middle panel) corresponds to $|\xi_x| + |\xi_y| \leqslant 5$.

3.5 Concluding remarks

In this chapter, we have considered scalar dispersion in two dimensional uniform periodic networks. We have extended the large-deviation approach developed in [87] for the square network to obtain a macroscale description of the scalar concentration at large times. The extension is straightforward in the case of the triangular network and more subtle for the hexagonal network. The reason for this is that the vertices of the square and triangular networks are translationally invariant; a property that does not hold for the hexagonal network. The vertex arrangement of the square and triangular networks form a Bravais lattice, thus it is possible that other periodic networks characterised by a Bravais lattice, have similar macroscale behaviour encapsulated by (3.2.10) (with the upper number in the sum modified accordingly).

The main quantity of interest is the rate function g (the Legendre transform of the principal eigenvalue f) which is able to describe scalar distribution at large distances from the centre of mass including at the tails. We obtained for each network a transcendental equation for f (3.2.10) or (3.2.13) by solving a family of eigenvalue problems. We then determined the behaviour of g both numerically and asymptotically identifying various physical regimes: near the centre of mass we recover the diffusive (Gaussian) approximation characterised by a centre of mass velocity and effective diffusivity tensor. In this regime we show that for weak flows at leading order all three networks share the same effective behaviour. For strong flow, depending on the orientation of the flow we have Taylor dispersion or mechanical dispersion in which the effective diffusivity is respectively independent or inversely proportional to the molecular diffusivity κ. In both cases effective diffusion at leading order can be described by random walks on a lattice which highlights the strength of effective diffusion is related to both the geometry and topology of the networks. We find that effective diffusion is most enhanced for the square network.

For large distances from the centre of mass, the diffusive approximation overestimates or underestimates g in large portions of the $\boldsymbol{\xi}$ - plane. The discrepancy however is least pronounced for the triangular network. For very large $|\boldsymbol{\xi}|$ (corresponding to the tails) and in the absence of flow, at leading order we find dispersion is controlled by a shortest path distance function between the elementary cells of networks. The effectiveness of which is dependent on the connectivity of the network. Finally for strong flows scalar concentration is at leading order independent of κ and can be described by a lattice random walk generalising mechanical dispersion to the large-deviation regime.

Chapter Four

Conclusion

This thesis develops a framework for the application of large deviation theory to the problem of scalar transport in porous media. This approach allows us to go beyond the scope of homogenisation theory and uncover various physical regimes relevant to the tails of the scalar concentration. We present the framework on two commonly studied models of periodic porous media; the first examined in chapter 2 is characterised by an array of impermeable obstacles arranged on a lattice and the second examined in chapter 3 is on regular networks composed of edges and vertices. It is useful to now highlight the shared dispersive properties of both models and to then conclude by mentioning several directions in which our results could be extended.

We observe that in both models of periodic porous media that large deviation effects lead to anisotropic behaviour that results in tail concentrations that can significantly differ from the diffusive approximation by exponential factors. This discrepancy is most evident in the dense limit in the first model and for networks with a small vertex degree in the second model. In both models the large deviation rate function deduced from a family of eigenvalue problems describes the scalar concentration over vast distances from the point of release and identifies various physical regimes: the diffusive regime with effective diffusivity usually obtained by homogenisation theory, a closely related regime associated with a lattice random walk, all the way to the extreme-tail regime where the scalar concentration is controlled by single shortest-distance paths. We emphasise that results obtained in both models exemplify a general phenomenon, relevant to a broad range of applications in porous media, composites and metamaterials, which takes its full significance when low concentrations are critical. This is the case in the presence of chemical reactions, as the example of the FKPP model makes plain. This adds the logistic term $\alpha\theta(1-\theta)$, with α the reaction rate, to the right-hand side of the transport equations (2.1.1a) and (3.1.5). It leads to the propagation of fronts with speed $c(\boldsymbol{e})$ in the direction of the unit vector $\boldsymbol{e}$. This speed can be deduced from the rate function by solving $g(c(\boldsymbol{e})\boldsymbol{e}) = \alpha$ or equivalently from its Legendre transform as $c(\boldsymbol{e}) = \inf_{p>0} \big(f(p\boldsymbol{e}) + \alpha)/p$ [36, 88]. This provides an explicit example of a macroscopic manifestation of the tail behaviour of the scalar concentration.

There a various natural directions the classical problem of diffusion applied to the first model (arrays of obstacles) in chapter 2 can take. A first direction is to adapt our approach to consider different, more complex obstacle geometries, with extension from the square lattice to other Bravais lattices and from two to three dimensions, e.g. with spherical obstacles. A second direction would incorporate the effect of a steady, incompressible flow. The impact of the flow on dispersion is determined by solving the appropriate family of eigenvalue problems which include advection by a specified velocity field. This velocity field, driven for instance by a large-scale pressure gradient, can be obtained as part of the solution of a homogenisation problem posed for a fluid model such as the Stokes or Navier–Stokes models. One expects that the interaction between the inhomogeneity in the flow and in the domain will lead to interesting dispersion regimes, dependent on the size of the obstacles and the intensity of the flow (see e.g. [63, 11] for the corresponding homogenisation regimes in the case of a Stokes flow). A third direction concerns the nearly periodic case, introducing modulations in the arrangement and size of the obstacles over long spatial scales (see [23] for corresponding homogenisation results). A fourth direction is to examine random distributions of obstacles such as those considered in [44, 84] or models of dispersion in complex media more sophisticated than simple diffusion [29, 65]. The fifth and final direction we suggest is the transfer of the tools of large-deviation theory from the (parabolic) diffusion equation to the (hyperbolic) wave equation, with applications to acoustics and photonics. Results are available about the effective wave speed (the analogue of the effective diffusivity) in media with obstacles, including in the dense limit [89]; it would be desirable to extend these to capture wave propagation over very large distances and to apply large deviations to go beyond simple dispersive corrections to homogenisation [1].

Future extensions to the advection-diffusion problem applied to the second model (periodic networks) studied in chapter 3 are: generalisation to three-dimensional networks, in particular to three dimensional Bravais lattices is immediate. Another possible extension is to consider the case of random arrangement of vertices. A further extension is to consider a time dependent periodic pressure gradient on a Newtonian incompressible flow (see [38] for effective diffusion results). A very interesting problem is to consider dispersion of active tracers in periodic networks using large-deviation estimates. The effective diffusivity was analysed in [7] in periodic porous media finding a competition between active dispersion and Taylor dispersion depending on the strength of flow. We expect the periodic networks considered in this chapter will aid in clarifying the dependence of dispersion on both geometry and strength of flow and highlight further dispersion regime, particularly at the tails of the distribution.

Bibliography

[1] A. Abdulle and T. Pouchon. Effective models for long time wave propagation in locally periodic media. *SIAM J. Numer. Anal.*, 56:2701–2730, 2018.

[2] P.M Adler. Porous media: Geometry and transport. *AIChE Journal*, 40(2):380–381, 1994.

[3] G. Allaire. Homogénéisation et convergence à deux échelles. application à un problème de convection diffusion. 1991.

[4] G. Allaire. Homogenization and two-scale convergence. *SIAM Journal on Mathematical Analysis*, 23(6):1482–1518, 1992.

[5] G. Allaire, M. Briane, R. Brizzi, and Y. Capdeboscq. Two asymptotic models for arrays of underground waste containers. *Applicable Analysis*, 88(10-11):1445–1467, 2009.

[6] G. Allaire and H. Hutridurga. Homogenization of reactive flows in porous media and competition between bulk and surface diffusion. *IMA Journal of Applied Mathematics*, 77(6):788–815, 07 2012.

[7] Roberto Alonso-Matilla, Brato Chakrabarti, and David Saintillan. Transport and dispersion of active particles in periodic porous media. *Phys. Rev. Fluids*, 4:043101, Apr 2019.

[8] B. Amaziane, S. Antontsev, L. Pankratov, and A. Piatnitski. Homogenization of immiscible compressible two-phase flow in porous media: Application to gas migration in a nuclear waste repository. *Multiscale Modeling & Simulation*, 8:2023–2047, 2010.

[9] M. P. Anderson. Introducing groundwater physics. *Physics Today*, 60, 2007.

[10] R. Aris. On the dispersion of a solute in a fluid flowing through a tube. *Proceedings of the Royal Society of London. Series A. Mathematical and Physical Sciences*, 235, 1956.

[11] J.L. Auriault and P.M. Adler. Taylor dispersion in porous media: Analysis by multiple scale expansions. *Advances in Water Resources*, 18, 1995.

[12] I. Babuška. Solution of interface problems by homogenization. I. *Siam Journal on Mathematical Analysis*, 7:603–634, 1976.

[13] I. Babuška. Solution of interface problems by homogenization. II. *SIAM Journal on Mathematical Analysis*, 7(5):635–645, 1976.

[14] I. Babuška. Solution of interface problems by homogenization. III. *SIAM Journal on Mathematical Analysis*, 8(6):923–937, 1977.

[15] N.S. Bakhvalov and G. Panasenko. *Homogenisation: Averaging Processes in Periodic Media: Mathematical Problems in the Mechanics of Composite Materials*. Mathematics and its Applications. Springer Netherlands, 1989.

[16] A. Bensoussan, J. L. Lions, and G. Papanicolaou. *Asymptotic analysis for periodic structures.* North Holland, 1978.

[17] H. Berestycki, F. Hamel, and N. Nadirashvili. The speed of propagation for KPP type problems. I: Periodic framework. *J. Eur. Math. Soc.*, 007(2):173–213, 2005.

[18] L. Berlyand, A. Novikov, and K.G. Alexander. *Introduction to the Network Approximation Method for Materials Modeling.* Cambridge University Press, 2012.

[19] D. Boffi. Finite element approximation of eigenvalue problems. *Acta Numerica*, 19:1–120, 2010.

[20] J.P Bouchaud and A. Georges. Anomalous diffusion in disordered media: Statistical mechanisms, models and physical applications. *Physics Reports*, 195(4):127–293, 1990.

[21] S. Boyd and L. Vandenberghe. *Convex Optimization.* Cambridge University Press, 2004.

[22] H. Brenner and K. Stewartson. Dispersion resulting from flow through spatially periodic porous media. *Philosophical Transactions of the Royal Society of London. Series A, Mathematical and Physical Sciences*, 297, 1980.

[23] M. Bruna and S. Chapman. Diffusion in Spatially Varying Porous Media. *SIAM Journal on Applied Mathematics*, 75, 2015.

[24] P. C. Chatwin. The cumulants of the distribution of concentration of a solute dispersing in solvent flowing through a tube. *Journal of Fluid Mechanics*, 51(1):63–67, 1972.

[25] P.C. Chatwin. The approach to normality of the concentration distribution of a solute in a solvent flowing along a straight pipe. *Journal of Fluid Mechanics*, 43(2):321–352, 1970.

[26] D. G. Crighton, F. G. Leppington, and D. S. Jones. Singular perturbation methods in acoustics: diffraction by a plate of finite thickness. *Proceedings of the Royal Society of London. A. Mathematical and Physical Sciences*, 335, 1973.

[27] H. Darcy. *Les fontaines publiques de la ville de dijon,*. Dalmont, 1856.

[28] L. de Arcangelis, J. Koplik, S. Redner, and D. Wilkinson. Hydrodynamic dispersion in network models of porous media. *Physical review letters*, 57:996–999, 09 1986.

[29] M. Dentz, M. Icardi, and J. J. Hidalgo. Mechanisms of dispersion in a porous medium. *Journal of Fluid Mechanics*, 841:851–882, 2018.

[30] K. D. Dorfman and H. Brenner. Generalized taylor-aris dispersion in discrete spatially periodic networks: Microfluidic applications. *Phys. Rev. E*, 65:021103, Jan 2002.

[31] J. P. Dougherty. Perturbation Methods in Fluid Mechanics. *Journal of Fluid Mechanics*, 79, 1977.

[32] L. C. Evans. Periodic homogenisation of certain fully nonlinear partial differential equations. *Proceedings of the Royal Society of Edinburgh: Section A Mathematics*, 120(3-4):245–265, 1992.

[33] A. Fannjiang and G. Papanicolaou. Convection enhanced diffusion for periodic flows. *SIAM J. Appl. Math.*, 54(2):333–408, 1994.

[34] A. Fannjiang and G. Papanicolaou. Convection-enhanced diffusion for random flows. *Journal of Statistical Physics*, 88(5-6):1033–1076, 1996.

[35] Y. Farah, D. Loghin, A. Tzella, and J. Vanneste. Diffusion in arrays of obstacles: beyond homogenization. *Proceedings of the Royal Society A: Mathematical, Physical and Engineering Sciences*, 476(2244):20200072, 2020.

[36] M. I. Freidlin. *Functional Integration and Partial Differential Equations.* Princeton University Press, 1985.

[37] M. I. Freidlin and A. D. Wentzell. *Random perturbations of dynamical systems.* Springer, 1984.

[38] G. Goldsztein. Solute transport in porous media. media with capillaries as voids. *SIAM Journal on Applied Mathematics*, 68, 2008.

[39] Z. Hashin and S. Shtrikman. A variational approach to the theory of the elastic behaviour of multiphase materials. *Journal of the Mechanics and Physics of Solids*, 11, 1963.

[40] P. H. Haynes and J. Vanneste. Dispersion in the large-deviation regime. Part I: shear flows and periodic flows. *J. Fluid Mech.*, 745:321–350, 2014.

[41] P. H. Haynes and J. Vanneste. Dispersion in the large-deviation regime. Part II: cellular flow at large Péclet number. *Journal of Fluid Mechanics*, 745, 2014.

[42] L.L.M. Heaton, E. López, P.K Maini, M.D. Fricker, and N.S Jones. Advection, diffusion, and delivery over a network. *Phys. Rev. E*, 86:021905, 08 2012.

[43] U. Hornung, editor. *Homogenization and Porous Media.* Springer, 1997.

[44] V.V. Jikov, S.M. Kozlov, and O.A. Oleinik. *Homogenization of Differential Operators and Integral Functionals.* Springer-Verlag, Berlin, 1994.

[45] C. Johnson. *Numerical Solution of Partial Differential Equations by the Finite Element Method.* Dover Publications, 2009.

[46] J.B. Keller. Conductivity of a medium containing a dense array of perfectly conducting spheres or cylinders or nonconducting cylinders. *Journal of Applied Physics*, 34, 1963.

[47] J.B. Keller. *Effective behaviour of heterogeneous media. In Statistical mechanics and statistical methods in theory and application.* Springer, 1977.

[48] D. L. Koch and J. F. Brady. A non-local description of advection-diffusion with application to dispersion in porous media. *Journal of Fluid Mechanics*, 180, 1987.

[49] D.L. Koch and J.F. Brady. Dispersion in fixed beds. *J. Fluid Mech.*, 154:399–427, 5 1985.

[50] D.L. Koch, R.G. Cox, H.Brenner, and J.F. Brady. The effect of order on dispersion in porous media. *Journal of Fluid Mechanics*, 200:173–188, 1989.

[51] J. Koplik, S. Redner, and D. Wilkinson. Transport and dispersion in random networks with percolation disorder. *Phys. Rev. A*, 37:2619–2636, Apr 1988.

[52] M.G. Krein and M.A. Rutman. *Linear Operators Leaving Invariant a Cone in a Banach Space.* American Mathematical Society translations. American Mathematical Society, 1950.

[53] Y. E. Kutsovsky, L. E. Scriven, H. T. Davis, and B. E. Hammer. Nmr imaging of velocity profiles and velocity distributions in bead packs. *Physics of Fluids*, 8(4):863–871, 1996.

[54] M.G. Larson and F. Bengzon. *The Finite Element Method: Theory, Implementation, and Applications*. Springer, 2013.

[55] D. Loghin. Code for diffusion in arrays of obstacles: beyond homogenisation, 2020.

[56] A.J. Majda and P. R. Kramer. Simplified models for turbulent diffusion: Theory, numerical modelling, and physical phenomena. *Physics Reports*, 314, 1999.

[57] M. Makwana, T. Antonakakis, B. Maling, S. Guenneau, and R. Craster. Wave mechanics in media pinned at bravais lattice points. *SIAM Journal on Applied Mathematics*, 76, 2015.

[58] R. Mauri. Dispersion, convection, and reaction in porous media. *Physics of Fluids A: Fluid Dynamics*, 3(5):743–756, 1991.

[59] J.M. Maxwell. *A Treatise of Electricity and Magnetism*. Clarendon Press, Oxford, 1873.

[60] D. R. McKenzie, R. C. McPhedran, G. H. Derrick, and Robert Brown. The conductivity of lattices of spheres. Part II: The body centred and face centred cubic lattices. *Proceedings of the Royal Society of London. A. Mathematical and Physical Sciences*, 362, 1978.

[61] D. W. McLaughlin, G. C. Papanicolaou, and O. R. Pironneau. Convection of

microstructure and related problems. *SIAM Journal on Applied Mathematics*, 45(5):780–797, 1985.

[62] R. C. McPhedran, D. R. McKenzie, and R. Brown. The conductivity of lattices of spheres. Part I: The simple cubic lattice. *Proceedings of the Royal Society of London. A. Mathematical and Physical Sciences*, 359, 1978.

[63] C.C. Mei. Method of homogenization applied to dispersion in porous media. *Transport Porous Med.*, 9(3):261–274, 1992.

[64] G. N. Mercer and A. J. Roberts. A centre manifold description of contaminant dispersion in channels with varying flow properties. *SIAM Journal on Applied Mathematics*, 50(6):1547–1565, 1990.

[65] F. Municchi and M. Icardi. Macroscopic models for filtration and heterogeneous reactions in porous media. *Advances in Water Resources*, 141:103605, 2020.

[66] F. Murat and L. Tartar. *H-Convergence*, pages 21–43. Birkhäuser Boston, 1997.

[67] G. Nguetseng. A general convergence result for a functional related to the theory of homogenization. *SIAM Journal on Mathematical Analysis*, 20(3):608–623, 1989.

[68] G. A. Pavliotis and A.M. Stuart. *Multiscale Methods: Averaging and Homogenization*, volume 53. Springer, 2008.

[69] W. T. Perrins, D. R. McKenzie, R. C. McPhedran, and R. Brown. Transport properties of regular arrays of cylinders. *Proceedings of the Royal Society of London. A. Mathematical and Physical Sciences*, 369, 1979.

[70] D. Pietro, B. Quaife, G. Biros, and R. Juanes. Prediction of the low-velocity distribution from the pore structure in simple porous media. *Physical Review Fluids*, 2, 2017.

[71] A. Quarteroni, R. Sacco, and F. Saleri. *Numerical Mathematics*, volume 37. Springer, 01 2007.

[72] J.W. Rayleigh. On the influence of obstacles arranged in rectangular order upon the properties of a medium. *The London, Edinburgh, and Dublin Philosophical Magazine and Journal of Science*, 34, 1892.

[73] J. Rubinstein and R. Mauri. Dispersion and convection in periodic porous media. *SIAM J. Appl. Math.*, 46(6):pp. 1018–1023, 1986.

[74] Y. Saad. *Numerical methods for large eigenvalue problems*, volume 66 of *Classics in Applied Mathematics*. Society for Industrial and Applied Mathematics (SIAM), Philadelphia, PA, 2011. Revised edition of the 1992 original.

[75] P. G. Saffman. Dispersion in flow through a network of capillaries. *Chemical Engineering Science*, 11(2):125–129, 1959.

[76] P. G. Saffman. Dispersion due to molecular diffusion and macroscopic mixing in flow through a network of capillaries. *Journal of Fluid Mechanics*, 7(2):194–208, 1960.

[77] M. Sahimi. Flow phenomena in rocks: from continuum models to fractals, percolation, cellular automata, and simulated annealing. *Rev. Mod. Phys.*, 65:1393–1534, Oct 1993.

[78] M. Sahimi. *Flow and transport in porous media and fractured rock: from classical methods to modern approaches.* Wiley-VCH, 2011.

[79] E. Sanchez-Palencia. Comportements local et macroscopique d'un type de milieux physiques heterogenes. *International Journal of Engineering Science*, 12(4):331 – 351, 1974.

[80] M. Shapiro and H. Brenner. Dispersion of a chemically reactive solute in a spatially periodic model of a porous medium. *Chemical Engineering Science*, 43, 1988.

[81] S. H. Simon. *The Oxford Solid State Basics.* Oxford University Press, 2013.

[82] L. Tartar. Compensated compactness and applications to partial differential equations. 1979.

[83] G.I. Taylor. Dispersion of soluble matter in solvent flowing slowly through a tube. *Proceedings of the Royal Society of London. Series A. Mathematical and Physical Sciences*, 219, 1953.

[84] S. Torquato. *Random Heterogeneous Materials: Microstructure and Macroscopic Properties.* Springer, 2002.

[85] S. Torquato, L.V. Gibiansky, M.J. Silva, and L.J. Gibson. Effective mechanical and transport properties of cellular solids. *International Journal of Mechanical Sciences*, 40, 1998.

[86] H. Touchette. The large deviation approach to statistical mechanics. *Physics Reports*, 478, 2009.

[87] A. Tzella and Vanneste J. Dispersion in rectangular networks: Effective diffusivity and large-deviation rate function. *Physical Review Letters*, 117, 2016.

[88] A. Tzella and J. Vanneste. FKPP fronts in cellular flows: The Large-Péclet regime. *SIAM J. Appl. Math.*, 75(4):1789–1816, 2015.

[89] A.L. Vanel, O. Schnitzer, and R.V. Craster. Asymptotic network models of subwavelength metamaterials formed by closely packed photonic and phononic crystals. *Europhys. Lett.*, 119(6):64002, 2017.

[90] S. Whitaker. The equations of motion in porous media. *Chemical Engineering Science*, 21(3):291–300, 1966.

[91] S. Whitaker. Diffusion and dispersion in porous media. *AIChE Journal*, 13:420 – 427, 05 1967.

[92] W. R. Young and Scott Jones. Shear dispersion. *Physics of Fluids A: Fluid Dynamics*, 3(5):1087–1101, 1991.